

Superconductivity Program for Electric Systems

Annual Progress Report for Fiscal Year 2005



Superconductivity Technology Center Los Alamos National Laboratory

Dean E. Peterson, Center Director and Program Manager
Kenneth R. Marken, Jr., Deputy Center Director
Jeffrey O. Willis, Principal Team Leader and Editor

Contributors:

P.N. Arendt
S.P. Ashworth
L. Civale
P.G. Clem^{SNL}
J.Y. Coulter
G. Croes
R.F. DePaula
P.C. Dowden
R. Feenstra^{ORNL}
A.T. Findikoglu
S.R. Foltyn
B.J. Gibbons
F. Grilli
J.R. Groves
H. Grube
A. Gurevich^{UW}
Y. Huang^{AMSC}
M. Hawley

T.G. Holesinger
T.A. Jankowski
M. Jaime
Q.X. Jia
J.A. Kennison
X. Li^{AMSC}
Y. Li
Y. Lin
J. MacManus-Driscoll^{UC}
B. Maiorov
M.P. Maley
J.R. Mantei^{UW}
V. Matias
D. Miller^{ANL}
V. Maroni^{ANL}
F.M. Mueller
P. Pelligrino^{SP}
D.E. Peterson

F.C. Prenger
A. Razani^{UNM}
J. Reeves^{SP}
M. Rupich^{AMSC}
E.N. Schmierer
V. Selvamanickam^{SP}
A. Serquis
C.J. Sheehan
L. Stan
J.A. Stewart
J. G. Storer
I. Usov
H. Wang
J.A. Waynert
J.O. Willis
Y.Y. Xie^{SP}

Key to non-LANL Affiliations

AMSC = American Superconductor Corp.
ANL = Argonne National Laboratory
ORNL = Oak Ridge National Laboratory
NMSU = New Mexico State University

SNL = Sandia National Laboratories
SP = SuperPower
UNM = University of New Mexico
UW = University of Wisconsin-Madison

Work supported by the United States Department of Energy
Office of Electricity Delivery & Energy Reliability



Los Alamos National Laboratory, an affirmative action/equal opportunity employer, is operated by the Los Alamos National Security, LLC for the National Nuclear Security Administration of the U.S. Department of Energy under contract DE-AC52-06NA25396. By acceptance of this article, the publisher recognizes that the U.S. Government retains a nonexclusive, royalty-free license to publish or reproduce the published form of this contribution, or to allow others to do so, for U.S. Government purposes. Los Alamos National Laboratory requests that the publisher identify this article as work performed under the auspices of the U.S. Department of Energy. Los Alamos National Laboratory strongly supports academic freedom and a researcher's right to publish; as an institution, however, the Laboratory does not endorse the viewpoint of a publication or guarantee its technical correctness.

Table of Contents

| | |
|---|----|
| Table of Contents | 3 |
| Table of Figures | 4 |
| Table of Tables | 11 |
| Glossary of Acronyms | 12 |
| Introduction..... | 13 |
| 1. Highlights of Fiscal Year 2005 | 15 |
| 2. Technical Activities | 17 |
| 2.1 Wire Technology | 17 |
| 2.1.1 LANL-SuperPower CRADA Strategic Research..... | 17 |
| 2.1.2 Self field and in-field performance enhancement for coated conductors | 24 |
| 2.1.3 Microstructures and Vortex Pinning in MOD and PVD-BaF ₂ ex-situ YBCO Films on RABiT SM | 42 |
| 2.1.4 Next Steps Towards a Commercializable Coated Conductor..... | 54 |
| 2.1.5 Study of Overcurrent Behavior in YBCO Coated Conductors Using a Localized Magnetic Field | 64 |
| 2.1.6 Combining modeling and measurements to control the ac losses in coated conductors..... | 69 |
| 2.2. Systems Applications..... | 77 |
| 2.2.1 Design and development of a 100 MVA HTS generator | 77 |
| 3. Fiscal Year 2005 Publications | 82 |
| 3.1. Journal Articles Published | 82 |
| 3.2. Journal Articles Submitted for Publication..... | 85 |
| 3.3. Other Publications and Conference Abstracts | 87 |
| 4. Patent and License Activity (April 1988 to September 2005)..... | 90 |
| 4a. Invention Disclosures and Patent Applications | 90 |
| 4b. Patents Granted | 91 |
| 4c. Licenses Granted..... | 95 |
| 5. Agreements in Progress (8 Active, all types) | 96 |
| 5a. CRADA Agreements - Active | 96 |
| 5b. Funds In / Funds Out Agreements – Active | 96 |
| 5c. Other Collaborations - Active..... | 96 |
| 6. Completed Agreements..... | 97 |
| 6a. CRADA Agreements - Completed | 97 |
| 6b. Funds In / Funds Out Agreements - Completed | 98 |
| 6c. Superconductivity Pilot Center Agreements - Completed..... | 99 |

Table of Figures

| | |
|---|----|
| Fig. 1. Lattice parameter as a function of rare earth (RE) composition x for $\text{RE}_x\text{Zr}_{1-x}\text{O}_y$ (left) and $\text{RE}_x\text{Hf}_{1-x}\text{O}_y$ (right). The $\text{Dy}_{0.2}\text{Hf}_{0.8}\text{O}_y$ lattice parameter is estimated. | 17 |
| Fig. 2. Reduction in stacking sequence complexity and thicknesss with $\text{RE}_2\text{Zr}_2\text{O}_7$ buffer..... | 18 |
| Fig. 3. Channeling yield as a function of Ar^+ dose. At low doses, all orientations survive, and at high doses even the (110) orientation is sputtered away..... | 18 |
| Fig. 4. Plan view selected area diffraction pattern of a non-IBAD MgO film on $\alpha\text{-Si}_3\text{N}_4$ exhibits random orientation. | 18 |
| Fig. 5. The number of interstitial defects ND (left) and normalized channeling yield (characterizing extended defects) (right) as a function of annealing temperature for MgO single crystals irradiated to $1 \times 10^{15} \text{ Ar}^+/\text{cm}^2$ and annealed for 3 minutes..... | 19 |
| Fig. 6. In-plane texture (FWHM) (left) and c-axis tilt (right) as a function of IBAD MgO film thickness for the nucleation layers Y_2O_3 and $\alpha\text{-Si}_3\text{N}_4$ | 19 |
| Fig. 7. HRTEM cross sectional images of IBAD MgO layers on two different nucleation layers. | 20 |
| Fig. 8. Plan view of 10 nm thick Y_2O_3 film (left), and SAD pattern of the Y_2O_3 nucleation layer (right) also showing random orientation. | 20 |
| Fig. 9a. Number of interstitial atoms as a function of implantation temperature. | 21 |
| Fig. 9b. In-plane texture as a function of ion assist current ratio for various temperatures..... | 21 |
| Fig. 10a. Schematic of IBAD deposition system..... | 21 |
| Fig. 10b. Film thickness, assist beam current, and in-plane texture along the deposition zone. $T_{\text{dep}} \sim 150^\circ\text{C}$ | 21 |
| Fig. 11a. Temperature of moving tape during IBAD MgO deposition as a function of time. | 22 |
| Fig. 11b. Film thickness, assist beam current, and in-plane texture along the deposition zone. $T_{\text{dep}} \sim 150^\circ\text{C}$ | 22 |
| Fig. 12a. Schematic of PLD target with Ni foil wedge..... | 22 |
| Fig. 12b. T_c and J_c as a function of Ni concentration in 200 nm thick YBCO films. | 22 |
| Fig. 13. Current distribution as a function of position across the width of a superconducting tape with a transport current of 80 A..... | 23 |
| Fig. 14. SuperPower MOCVD YBCO/IBAD MgO coated conductor wound into a coil at LANL. Coil being wound (left) and completed (right)..... | 23 |
| Fig. 15. Critical current as a function of film thickness (left) and of applied magnetic field H/c for IBAD MgO coated conductors. | 24 |
| Fig. 16. Critical current density as a function of total film thickness for single layer and multilayer films. | 24 |
| Fig. 17. a) Schematic of model for thickness dependence of the critical current density of YBCO films. b) Critical current density as a function of film | |

| | |
|--|----|
| thickness for YBCO films and the model result. c) Incremental j_c as a function of film thickness for ion-milled films and for the model..... | 25 |
| Fig. 18. SEM plan view image of a 25 x 25 μm square region of a film surface for a) a 3.7 μm thick single layer YBCO film, b) a 3.2 μm thick YBCO/SmBCO 6-layer multilayer, and c) a 3.1 μm thick YBCO/CeO ₂ 6-layer multilayer film..... | 26 |
| Fig. 19a. Critical current density as a function of YBCO film thickness for single YBCO layers and both YBCO/CeO ₂ and YBCO/SmBCO multilayers..... | 26 |
| Fig. 19b. Rocking curve peak width as a function of YBCO film thickness..... | 26 |
| Fig. 20. a) Schematic of straight vortices in a thin film. b) Normalized thickness dependence of J_c in the model. c) Schematic of flexible vortices in a thick film. | 27 |
| Fig. 21. (Left) Schematic of bilayer films with PrBCO layer and (right) TEM micrograph of layers. | 27 |
| Fig. 22a. J_c for a YBCO/PrBCO bilayer and results of 2D-3D model as a function of PrBCO layer thickness..... | 28 |
| Fig. 22b. J_c for a YBCO/PrBCO bilayer and results from incremental j_c model as a function of PrBCO layer thickness. | 28 |
| Fig. 23. Schematic of stacking sequence and results on J_c of added a CeO ₂ layer to the PrBCO/YBCO bilayer film..... | 28 |
| Fig. 24a. TEM micrograph of PLD YBCO on STO-buffered single crystal MgO showing a high density of defects near the interface (lower arrow) and threading dislocations parallel to the columnar grain boundaries. | 29 |
| Fig. 24b. Fast fourier filtered image of a high-resolution cross section of the dark band in Fig. 10a indicating the presence of misfit dislocations..... | 29 |
| Fig. 25a. TEM plan view images of a ~20 nm thick YBCO film on a STO single-crystal substrate. Observed dislocation spacing is ~17 nm..... | 29 |
| Fig. 25b. TEM plan view showing two adjacent growth islands in a 20 nm thick YBCO film on STO. | 29 |
| Fig. 26. Measured critical current density as a function of PrBCO layer thickness and that expected for interfacial pinning for a YBCO-PrBCO bilayer. | 30 |
| Fig. 27. J_c for YBCO single layers and YBCO/CeO ₂ and YBCO/PrBCO multilayers as a function of total multilayer thickness. | 30 |
| Fig. 28a. Critical current density as a function of angle for a YBCO film at 5 T and 75 K..... | 31 |
| Fig. 28b. Normalized critical current density as a function of normalized magnetic field \parallel c axis. | 31 |
| Fig. 29a. Critical current density as a function of angle for an ion milled YBCO film. .. | 32 |
| Fig. 29b. Critical current density as a function of magnetic field \parallel c. The inset shows the layer thickness removed by ion milling at each step. | 32 |
| Fig. 30a. Scaled critical current density as a function of angle for the ion milled YBCO film of Fig. 29. | 32 |
| Fig. 30b. Scaled critical current density as a function of magnetic field \parallel c. The inset shows the normalization factors derived at self field..... | 32 |

| | |
|---|----|
| Fig. 31. Critical current density as function of angle for YBCO on STO and with an intervening layer of PrBCO. | 33 |
| Fig. 32a. Schematic of mechanism for improvement of self field J_c of multilayer films. | 33 |
| Fig. 32b. J_c as a function of field as J_c^{sf} and α change. | 33 |
| Fig. 33. Normalized J_c as a function of magnetic field for YBCO on single-crystal STO and on STO buffer layers (lower two entries in legend). | 34 |
| Fig. 34a. Critical current density as a function of $H c$ for a single layer and multilayer. | 34 |
| Fig. 34b. Field dependence of I_c for 1, 4, and 6 layer multilayers. | 34 |
| Fig. 35a. Critical current as a function of applied field $ c$ for multilayer films and a single layer film with STO outgrowths. | 35 |
| Fig. 35b. Critical current as a function of angle at 65 K and 3 T. Minimum I_c is greater than 120 A/cm width. | 35 |
| Fig. 36a. Critical current density as a function of applied magnetic field parallel to c for YBCO and YBCO doped with BZO nanoparticles. | 35 |
| Fig. 36b. Normalized critical current density as a function of magnetic field parallel to c for BZO doped and undoped YBCO. (J.L. MacManus-Driscoll et al. Nature Materials 3, 439 (2004). | 35 |
| Fig. 37a. Critical current density as a function of angle for undoped YBCO and YBCO + BZO (red - early work; blue - recent result). | 36 |
| Fig. 37b. Normalized critical current as a function of magnetic field for undoped YBCO and BZO doped YBCO. | 36 |
| Fig. 38a. Critical current density as a function of angle for BZO doped and undoped YBCO. | 36 |
| Fig. 38b. Critical current density minus the random pinning contribution for the samples of Fig. 38a. | 36 |
| Fig. 39a. Schematic and micrograph of defect model for Er additions in MOD YBCO. | 37 |
| Fig. 39b. Critical current density as a function of angle for MOD YBCO with & without Er additions. | 37 |
| Fig. 40a. Schematic of dislocations in BZO doped YBCO, each emanating from a BZO nanoparticle. | 37 |
| Fig. 40b. Irreversibility line for YBCO samples near 5 T showing "bump" feature near 5 T characteristic of the matching field for correlated defects. | 37 |
| Fig. 41a. Temperature dependence of critical current density as a function of applied field $H c$ | 38 |
| Fig. 41b. Critical current density as a function of angle for thick YBCO, multilayer YBCO and BZO doped YBCO as a function of angle at 65 K & 3 T. | 38 |
| Fig. 42. Normalized critical current density as a function of normalized field for YBCO at a range of temperatures. | 38 |
| Fig. 43a. Magnetization as a function of applied field parallel to c for a thick YBCO film. | 39 |

| | |
|---|----|
| Fig. 43b. Critical current density as a function of applied magnetic field determined from magnetization data. | 39 |
| Fig. 44. Critical current density as a function of magnetic field parallel to c from transport, from magnetization, and from magnetization corrected for voltage criterion. | 39 |
| Fig. 45a. Magnetization critical current as a function of magnetic field parallel to c at the temperatures indicated. | 40 |
| Fig. 45b. Temperature dependence of the power law exponent α and the critical field H_{cr} derived from the data shown in Fig. 31a. | 40 |
| Fig. 46a. Power law exponent α as a function of temperature for single and multilayer undoped YBCO films. | 41 |
| Fig. 46b. Critical current as a function of applied field parallel to c at 30 K for single and multilayer undoped YBCO films. | 41 |
| Fig. 47. Architecture of MOD-BaF ₂ - and PVD-BaF ₂ / RABiTS™-based tapes. | 42 |
| Fig. 48a. SEM of MOD YBCO surface. | 42 |
| Fig. 48b. Raman of two REBCO films as a function of wave number. | 42 |
| Fig. 49. Characteristic features of YBCO films produced by different processes. | 43 |
| Fig. 50a. Coherent Y ₂ O ₃ precipitate in PLD YBCO. | 43 |
| Fig. 50b. LANL 1.5 μ m PLD YBCO film on IBAD MgO. The c-axis aligned defects, such as grain boundaries, dislocations, and anti-phase boundaries, are the source of correlated $J_c(H c)$ pinning. | 43 |
| Fig. 51a. MOD films show a very small c-axis peak and a large ab-plane peak. | 44 |
| Fig. 51b. PLD films show a large c-axis peak and a small ab plane peak. | 44 |
| Fig. 52a. MOD films are strongly dominated by ab-plane correlated pinning. | 44 |
| Fig. 52b. PLD films have clearly separated random pinning, c-axis-, and ab-plane correlated pinning regions. | 44 |
| Fig. 53a. HRTEM of MOD film showing intergrowths. | 45 |
| Fig. 53b. TEM image of MOD film showing non-coherent inclusion | 45 |
| Fig. 54. TEM image of MOD film showing porosity and other features. | 45 |
| Fig. 55a. TEM of 0.7 μ m PVD-BaF ₂ film on AMSC RABiTS film showing variations in microstructure and chemistry. | 45 |
| Fig. 55b. TEM of 0.7 μ m PVD-BaF ₂ film on AMSC RABiTS film showing variations in microstructure and chemistry. | 45 |
| Fig. 56. Images of an AMSC 0.8 μ m MOD YBCO research sample with $I_c = 264$ A/cm-w processed in a scale-up furnace. | 46 |
| Fig. 57. TEM images illustrating various features of a 4 cm wide long-length conductor 0.8 μ m thick with $I_c=214$ A/cm-w. | 46 |
| Fig. 58. Schematic of the baseline process for heat treatment of an MOD film and a modified process with a high temperature oxygen anneal (HTOA) added. | 47 |
| Fig. 59. Above: X-ray diffraction scan of MOD YBCO (by X. Li, AMSC). Right: Angle and field dependence of baseline and HTOA films. | 47 |

| | |
|--|----|
| Fig. 60 TEM images of baseline and HTOA MOD films. The c axis is vertical and the a and b axes are horizontal in these images. | 48 |
| Fig. 61a. Enhanced pinning with Dy substitution in PLD YBCO films. | 48 |
| Fig. 61b. Enhanced pinning in MOD films with Ho addition, but little enhancement with substitution. | 48 |
| Fig. 62a. Critical current density as a function of magnetic field for Er additions in MOD films. The same trends are observed at 65 K and 75 K. | 49 |
| Fig. 62b. Critical current density as a function of angle for Er additions in MOD films. The I_c (75K, sf) are baseline 250 A/cm and 25% and 50% Er additions 260 A/cm. | 49 |
| Fig. 63. Micrographs of ex-situ MOD films with varying amounts of erbia additions (FIB by Dean Miller, ANL) | 49 |
| Fig. 64. Micrographs of the surface of ex-situ MOD films with varying amounts of Er additions. | 50 |
| Fig. 65. Elemental maps of the ex-situ MOD film with 100% Er additions shown in Fig. 64. | 50 |
| Fig. 66. TEM micrographs of Y-124 inclusions in baseline (spacing 16 nm) and 50% Er added spacing (111 nm) ex-situ MOD films. (Dean Miller, ANL) | 51 |
| Fig. 67. XRD patterns of ex-situ MOD films at baseline and with Er additions and showing reduced peak broadening. (X. Li et al., AMSC)..... | 51 |
| Fig. 68. Schematic (right) and TEM micrograph (left) of nanodot and surrounding strain fields. | 52 |
| Fig. 69. Critical current density as a function of angle for MOD YBCO films (left), baseline and 50% Er additions and a PLD YBCO film. | 52 |
| Fig. 70. a) Y124 intergrowths, found in baseline MOD films. b) nanodots plus extended structure found in 50% Er added MOD films. | 53 |
| Fig. 71. Schematic of the IBAD system. | 54 |
| Fig. 72. Original stacking sequence through the epi-MgO layer. | 54 |
| Fig. 73. RHEED patterns during deposition. | 55 |
| Fig. 74a. Texture across the width of a tape. | 55 |
| Fig. 74b. Texture along a 10 m length of tape. | 55 |
| Fig. 75a. Schematic of the assist ion source geometry. | 55 |
| Fig. 75b. Tilting of the MgO c axis results in a stair step template and a vicinal angle α | 55 |
| Fig. 76. IBAD deposition geometry with an adjustable shield to allow for nucleation layer pretreatment. | 56 |
| Fig. 77. Tilt of the MgO axis can be controlled by pretreatment of the nucleation layer. | 56 |
| Fig. 78. AFM RMS roughness measurements for Y_2O_3 sol-gel coatings on Hastelloy substrates. | 56 |

| | |
|--|----|
| Fig. 79 a) in-plane texture as a function of gross deposit thickness for various ratios ρ of ion/molecule ratio. b) in-plane texture as a function of ρ times the gross deposit thickness. | 57 |
| Fig. 80. Texture as measured by $\Delta\phi$ FWHM as a function of IBAD deposition time for IBAD MgO and other competing processes. | 57 |
| Fig. 81. IBAD TiN properties. | 58 |
| Fig. 82. Out-of-plane (left) and in-plane texture for a thick YBCO film. | 59 |
| Fig. 83. Uniformity along the length of a coated conductor tape. | 59 |
| Fig. 84. a) Scribing of tape into 10 strips for b) I_c measurements. | 60 |
| Fig. 85. Geometry of MOI samples cut from middle of centimeter wide tape. | 60 |
| Fig. 86. MOI as function of current density for a coated conductor tape. | 60 |
| Fig. 87. Electron back-scattered diffraction (EBS) images of the (left) out-of-plane (angle between sample normal and nearest crystal axis) and of (right) in-plane alignment (angle between rolling direction and nearest crystal axis). | 61 |
| Fig. 88. Grain boundary map of PLD YBCO/IBAD MgO coated conductor. | 61 |
| Fig. 89. Δm as a function of applied field for a coated conductor film at 50 K shows power law behavior. | 61 |
| Fig. 90a. Critical current as a function of position along a 1.2 m long tape. Mean I_c (75 K, sf) is 350 A. | 62 |
| Fig. 90b. I-V curve and I_c distribution across the tape width of a 7 cm, 525 A tape. | 62 |
| Fig. 91. Photograph of reel-to-reel tape measurement system set up for 4 cm wide conductor. | 62 |
| Fig. 92a. Critical current per cm width as a function of length for LANL tapes during the past year. | 63 |
| Fig. 92b. Critical current per cm width as a function of length for leading institutions producing coated conductor tapes. | 63 |
| Fig. 93. Response of an unstabilized coated conductor tape to an overcurrent. | 64 |
| Fig. 94a. Schematic diagram of the experimental measurement configuration. | 66 |
| Fig. 94b. Magnetic field generated by 2 NdFeB magnets separated by a distance of 0.64 cm and normalized critical current of a coated conductor tape as a function of position along the tape. | 66 |
| Fig. 95a. Voltage and temperature rise as a function of transport current for sample A (unstabilized). | 67 |
| Fig. 95b. Temperature rise as a function of power density for sample A. | 67 |
| Fig. 96a. Voltage and temperature rise as a function of transport current for sample B with 25 μm of copper on one side. | 67 |
| Fig. 96b. Temperature rise as a function of power density for sample B showing clearly the large change of heat transfer efficiency with onset of boiling. | 67 |
| Fig. 97a. Voltage and temperature rise as a function of transport current for coated conductor sample C with 50 μm of copper on each side. | 68 |
| Fig. 97b. Temperature rise as a function of power density for sample C. | 68 |

| | |
|--|----|
| Fig. 98. AC losses for coated conductor tape as a function of ac perpendicular field and ac transport current..... | 69 |
| Fig. 99. Comparison of measured and calculated ac losses as a function of applied perpendicular ac magnetic field. | 70 |
| Fig. 100. a) Multifilament tape prevents flux from entering. b) Multifilament tape with transversal cross cuts allows flux to enter between filaments. | 70 |
| Fig. 101. Top: Schematic of experiment to determine extent of flux penetration into multifilament tape. Bottom: Penetration of flux into the tape as a function of position away from the cross-cut. | 71 |
| Fig. 102. FEM results for the multifilament tape with crosscuts every 20 cm. | 71 |
| Fig. 103a. Transport current loss for 10 mm wide, 10 filament tapes with and without cross cuts as a function of peak current. | 72 |
| Fig. 103b. Magnetization ac loss for a 10 mm wide tape and one cut into 1 mm wide strips as a function of applied magnetic field. | 72 |
| Fig. 104a. Magnetic losses and total losses for a 10 mm wide tape and one with 10 filaments and cross cuts as a function of transport current and magnetic field. | 72 |
| Fig. 104b. Total losses for several tape configurations as a function of magnetic field. | 72 |
| Fig. 105a. Section of cuts in 10 mm wide tape made by microtome blade pack with spacing of 400 μm | 73 |
| Fig. 105b. Cutting portion of 24-blade microtome blade pack. | 73 |
| Fig. 106. a) Blade pack cutting grooves in tape moving to the left. b) Flexure between blades to ensure alignment on μm scale. c) cross section of cut topography. | 73 |
| Fig. 107a. Magnetic field distribution for a stack of tapes in an applied perpendicular magnetic field. | 74 |
| Fig. 107b. Magnetic field distribution for a stack of tapes carrying a transport current. | 74 |
| Fig. 108a. Symmetry considerations reduce the volume of material for FEM simulation of a stack of 8 tapes to 1 quadrant and to a 2D problem. | 74 |
| Fig. 108b. Results of FEM simulation of an 8-tape stack. The arrows indicate the direction and magnitude of the magnetic field. The scale in the lower part of the figure shows the field intensity color code. | 74 |
| Fig. 109. AC losses as a function of peak perpendicular applied field for 8 individual tapes and stacks of 8 tapes with separations of 1 mm and 0.1 mm. | 75 |
| Fig. 110a. FEM simulations of the ac losses per tape as a function of peak field for a stack of 1 to 8 tapes. | 75 |
| Fig. 110b. Measured ac losses per tape as a function of peak field for a stack of 1 to 8 tapes. | 75 |
| Fig. 111a. FEM simulations of the transport losses of a 8 individual tapes and of an 8 tape stack as a function of tape separation. | 76 |
| Fig. 111b. Measurements of the transport losses of a single tape and stack of 4 tapes. | 76 |

| | |
|---|----|
| Fig. 112. Surfaces at room temperature outgas and unless absorbed by a getter, result in a heat load on cold surfaces. | 77 |
| Fig. 113. Outgassing rate as a function of time for various materials and treatments..... | 77 |
| Fig. 114. Schematic of rotor (right) and coupling (left) with heat pipe transferring the heat..... | 78 |
| Fig. 115. Experimental vs. model predictions for a heat pipe with a 4° adverse tilt. | 79 |
| Fig. 116. Heat pipe components and schematics. | 79 |
| Fig. 117. Ac loss measurements in an HTS coil. | 80 |

Table of Tables

| | |
|--|----|
| Table 1. Interfacial and bulk j_c and range z_r for YBCO films. | 30 |
| Table 2. Process speeds for IBAD deposition by step..... | 58 |
| Table 3. Outgassing rates for selected materials..... | 78 |

Glossary of Acronyms

| | |
|----------|--|
| ANL | Argonne National Laboratory |
| AMSC | American Superconductor Corporation |
| BEI | Backscatter Electron Imaging |
| Bi-2212 | $\text{Bi}_2\text{Sr}_2\text{CaCu}_2\text{O}_8$ |
| Bi-2223 | $(\text{Bi,Pb})_2\text{Sr}_2\text{Ca}_2\text{Cu}_3\text{O}_8$ |
| BSCCO | Bi-2212 or Bi-2223 |
| CC | Coated Conductor |
| CRADA | Cooperative Research and Development Agreement |
| EBS | Electron Back-Scattered Diffraction |
| EDS | Energy Dispersive Spectroscopy |
| FCC | Fault Current Controller |
| FCL | Fault Current Limiter |
| FEM | Finite Element Modeling |
| HTS | High-Temperature Superconductivity |
| IBAD | Ion Beam-Assisted Deposition |
| I_c | Critical current of a superconductor, A |
| J_c | Critical current density of a superconductor, A/cm^2 |
| LANL | Los Alamos National Laboratory |
| LARP | Los Alamos Research Park |
| MgO | Magnesium Oxide |
| MOCVD | Metal Organic Chemical Vapor Deposition |
| MOD | Metal Organic Deposition |
| MRI | Magnetic Resonance Imaging |
| NHMFL | National High-Magnetic Field Laboratory |
| ORNL | Oak Ridge National Laboratory |
| OSTI | Oxford Superconductivity Technology, Inc. |
| PLD | Pulsed-Laser Deposition |
| RBS | Rutherford Backscattering Spectroscopy |
| RHEED | Reflection High-Energy Electron Diffraction |
| SAD | Selected Area Diffraction |
| SEM | Scanning Electron Microscopy |
| Sm-123 | $\text{SmBa}_2\text{Cu}_3\text{O}_{7-\delta}$ |
| SPI | Superconductivity Partnerships with Industry |
| STC | Superconductivity Technology Center (Los Alamos) |
| T_c | Critical temperature for superconductivity, K |
| TEM | Transmission Electron Microscopy |
| TOFISARS | Time of Flight Ion Scattering and Recoil Spectroscopy |
| XRD | X-Ray Diffraction |
| YBCO | $\text{YBa}_2\text{Cu}_3\text{O}_{7-\delta}$ |
| YSZ | Yttria-Stabilized Zirconia |

Introduction

The rate of progress towards practical applications of high temperature superconductors (HTS) continues to be very rapid. BSCCO tapes are now commercially available for use in the Superconductivity Partnership Initiative (SPI) projects and other prototype power demonstrations. Second-generation coated conductors continue to display very high critical currents in long lengths when cooled with liquid nitrogen indicative of the future potential for wide spread use in power applications. The SPI projects including the three transmission cable initiatives, fault current limiter, generator, flywheel, motor, and transformer are all exciting. The national laboratories are proud to have played important roles in advancing these technical successes.

LANL continued to be a CRADA partner with American Superconductor in the Wire Development Group focused on advancing further improvement of properties of second generation YBCO coated conductor tapes. Our contributions in microscopic and superconducting characterizations have been critical to continued technical advancements in this area.

New, unique tape processing and characterization capabilities have been developed at the Research Park that are now available to other national labs, universities, and industrial collaborators.

LANL continued strong partnerships with Superpower and American Superconductor in second-generation wire development focusing on the IBAD MgO technology. These collaborations have been extremely beneficial in accelerating their progress towards commercialization of coated conductors. Our expertise in evaluating vortex pinning in superconductor tapes as a function of temperature and magnetic field amplitude and angle was shown to be very valuable. LANL contributions towards characterizing and minimizing ac losses in coated conductors have been substantial.

LANL continued in a strong partnership with General Electric focused on a 100 MVA HTS SPI generator. LANL supports the CRADA through outgassing studies, ac loss studies, and development of a rotating heat pipe for cooling the rotor.

Research and development activities at LANL related to the HTS program for FY05 are collected in this report. Technical highlights are listed in Section 1 and individual project summaries appear in Section 2. Section 3 lists the 33 journal articles published and another 17 submitted and an additional 30 other publications and conference abstracts for the year. Section 4 summarizes the total patent and license activity, and Section 5 lists the various agreements underway and completed.

Dean E. Peterson, Leader
Superconductivity Technology Center

1. Highlights of Fiscal Year 2005

- Two buffer layers were replaced with a single layer (RE-Zr oxide) compatible with SuperPower's high rate reactive sputter process.
- Determined that using Y_2O_3 as the nucleation layer leads to reduced c-axis tilt and better in-plane texture. Experimental annealing data on damage anisotropy data for IBAD MgO ([100] and (111) orientations removed faster than (110)) correlates well with theoretical model. Lower IBAD deposition temperature is found to reduce sensitivity to ion assist ratio and leads to better in-plane texture.
- A model to explain the thickness dependence of the critical current I_c of YBCO coated conductors utilizes an incremental critical current density j_c . Using tools, such as PrBCO/YBCO multilayers, we have narrowed the possible explanations for the thickness dependence to the presence of misfit dislocations resulting from interfacial effects. The defects are uncorrelated and scarce
- These PrBCO/YBCO multilayers retain their strong I_c performance in an applied magnetic field. The multilayers (and thick single layer) undoped YBCO films surpass all DOD Title III I_c target values. With added $BaZrO_3$ (nanoparticles), record low values of I_c decay in magnetic fields have been achieved.
- In collaboration with American Superconductor Corp. and the Wire Development Group, microstructural and electrical characterizations were found to be significantly different for MOD (and other ex-situ processed) lamellar structure films versus, for instance, columnar structure PLD films. Y124 intergrowths were found to be the dominant ab-plane pinning structure in the MOD films. Rare earth oxide additions were found to produce nanodots and greatly enhanced c-axis pinning in the ex-situ films.
- MgO IBAD processing has been accelerated such that high quality IBAD can be produced in less than 2 s with an in-plane texture of 7° . Typical production rates for 10 m lengths yield 4 - 6° texture. Elimination of the $a-Al_2O_3$ layers and using a thicker MgO layer also led to better texture. Sol gel deposition has been investigated for the barrier/nucleation layer deposition. Other materials have been investigated for the IBAD layer, in particular TiN could be used as part of a conductive buffer stack.
- Reel to reel deposited YBCO had an I_c value of 350 A/cm width at 1 m lengths and 530 A/cm-width for a short (7 cm) length. Long polished substrates and IBAD buffered tapes were provided to various collaborators.
- Copper electroplating of YBCO coated conductors was found to substantially expand the stability region of the conductors during over current operation. The voltage/current power law exponent n is much reduced with electroplating, from ~ 12 to ~ 2 , and a power density and temperature rise 20 times greater than that of an unstabilized conductor can be controllably achieved.
- AC magnetic field losses in a single tape can be reduced significantly ($\times 100$ at 30 mT) by filamentizing a conductor and making cross cuts at fixed separations. Finite element modeling calculations indicate that, in contrast

to the predictions of the analytical models, the magnetic losses of a stack of (~8) tapes decreases by a factor of 10 to 30 for <1 mm separation. The tapes show only a modest increase (6-7) in transport ac losses for this separation, indicating that there is a window of reduced losses for current and field calculations.

- *LANL has supported GE in the HTS generator SPI project by evaluating materials for long-term vacuum maintenance and reduced refrigeration costs. LANL has also been developing a more efficient cooling system for the generator rotor using heat pipe technology and has been providing expertise in thermal modeling of the system.*

2. Technical Activities

2.1 Wire Technology

2.1.1 LANL-SuperPower CRADA Strategic Research

P.N. Arendt, S.R. Foltyn, L. Civale, R. DePaula, J.R. Groves, H. Grube, M. Hawley, T.G. Holesinger, Q.X. Jia, B. Maiorov, V. Matias, F.M. Mueller, L. Stan, I. Usov and H. Wang, SuperPower: P. Pellegrino, V. Selvamanickam, J. Reeves, and Y.Y. Xie

We report here on much of the SuperPower CRADA-related work we have performed during the last year. This includes work on alternate buffer layers, on understanding and optimizing the IBAD process, studying effects of impurities from the substrate on the YBCO performance, measuring the critical current density across the tape width and fabricating and characterizing coils of coated conductor wire.

Buffer layers have been optimized at LANL for the IBAD MgO template (YBCO/STO/homo-epi MgO/IBAD MgO). This results in excellent I_c and J_c , but the MgO and STO buffers are incompatible with SuperPower's high-rate reactive sputter deposition processing. Sr and Ti cannot be fabricated into a metal alloy target that is required for sputtering. For MgO, the high Mg vapor pressure results in the metal evaporating from the deposition surface before reacting with background O_2 yielding a thickness control issue. Therefore, we have decided to focus on MeZrO and MeHfO buffers, where Me is a metal. Typically, the melting points T_m of these materials follow this inequality: $T_m(\text{hafnates, zirconates}) > T_m(\text{titanates}) > T_m(\text{niobates})$. Further, the very refractory oxides tend to have chemical inertness with YBCO (e.g. $BaZrO_3$), yielding a possible advantage for high-rate, high-temperature YBCO deposition. However, similar to Sr-Ti, Ba-Zr cannot be fabricated as an alloy target.

RE-Zr and RE-Hf satisfy several Hume-Rothery conditions for alloy formation. In this study, we focused on the least expensive RE elements, e.g., Nd, Sm, Gd, Dy, and Er. These elements form stable alloys with Zr and Hf. The REZrO and REHfO compounds form cubic phases over a wide range of stoichiometries, as shown in Fig. 1. Because of this stoichiometry range, the cubic phase is retained even if the film stoichiometry drifts during long length processing, resulting in a robust process.

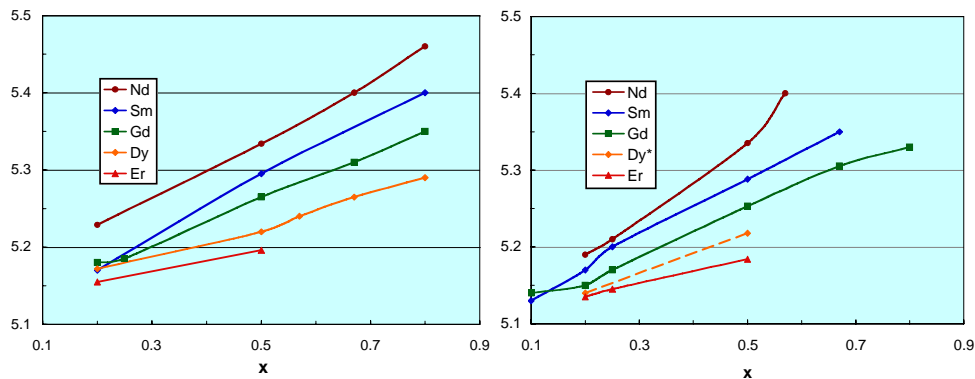


Fig. 1. Lattice parameter as a function of rare earth (RE) composition x for $RE_xZr_{1-x}O_y$ (left) and $RE_xHf_{1-x}O_y$ (right). The $Dy_{0.2}Hf_{0.8}O_y$ lattice parameter is estimated.

Using this new RE-Zr or RE-Hf buffer, it is possible to replace two buffers with one, and reduce the thickness of the stack (Fig. 2). Initial PLD-YBCO results are very promising for the use of reactive sputtering to produce this buffer. Texture at the various layers are IBAD MgO: $\Delta\phi = 6.2^\circ$, $\Delta\omega = 2.3^\circ$; $\text{Sm}_2\text{Zr}_2\text{O}_7$: $\Delta\phi = 4.4^\circ$, $\Delta\omega = 2.5^\circ$; YBCO: $\Delta\phi = 2.7^\circ$, $\Delta\omega = 1.1^\circ$. A 1.5 μ thick film using the $\text{Sm}_2\text{Zr}_2\text{O}_7$ buffer showed very good properties and had a T_c of 89 K and a J_c of 2.6 MA/cm² resulting in $I_c = 390$ A/cm-width.

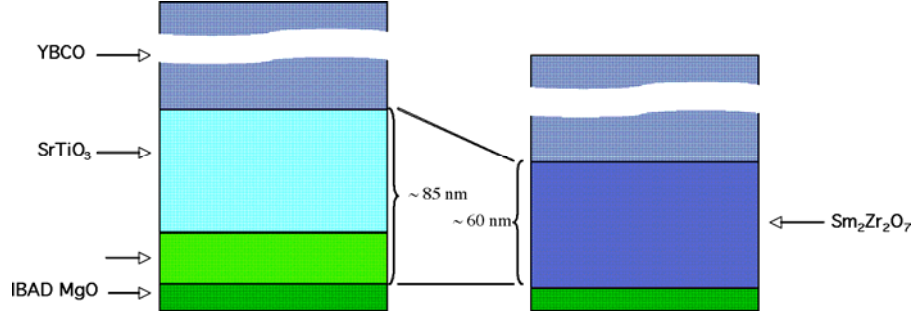


Fig. 2. Reduction in stacking sequence complexity and thickness with $\text{RE}_2\text{Zr}_2\text{O}_7$ buffer.

Several effects occur simultaneously during growth of films via IBAD texturing, such as anisotropic ion-induced damage, anisotropic sputter yield, anisotropic defect annihilation, and anisotropic ion channeling. This prompted a study of ion induced damage anisotropy while attempting to suppress other effects. MgO single crystals of (100), (110) and (111) orientations were implanted with 100 keV Ar^+ ions at varying doses and implantation temperatures. At 100 keV, the sputtering is negligible. The damage is centered at a depth of about 100 nm below crystal surface. Implants were performed 7° from normal to minimize channeling. Larger defect clusters are expected at this energy vs. ~ 1 keV range used during IBAD.

Rutherford backscattering spectrometry, combined with channeling, gives information on the concentration and type of defects. We used the following three damage criteria in our study 1) χ_{\min} is dominated by lattice distortions surrounding extended defects; 2) N_D represents the number of isolated atoms displaced from lattice sites (interstitials), and 3) χ_{\max} is determined by combining both of the above defect types. Previously, we learned that Ar^+ damage anisotropy of MgO crystals (Fig. 3) indicated a possible explanation for the IBAD MgO texturing mechanism. However, a question arises as to what occurs if the assist beam current density is too low. Here, we find that for the ion dose less than $\sim 4 \times 10^{15} \text{ Ar}^+/\text{cm}^2$, all MgO orientations survive bombardment, resulting in a randomly oriented film, similar to that of the non-IBAD film shown in Fig. 4.

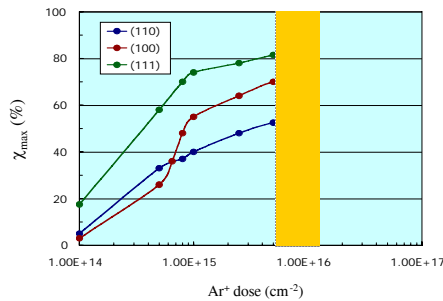


Fig. 3. Channeling yield as a function of Ar^+ dose. At low doses, all orientations survive, and at high doses even the (110) orientation is sputtered away.

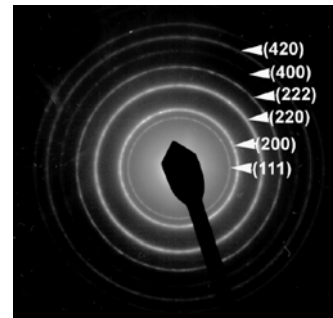


Fig. 4. Plan view selected area diffraction pattern of a non-IBAD MgO film on $\alpha\text{-Si}_3\text{N}_4$ exhibits random orientation.

At some point, as the dose is increased, all orientations but the (110) are removed by sputtering. Also, at even higher doses ($>1 \times 10^{16} \text{ Ar}^+/\text{cm}^2$), the (110) oriented MgO grains also are completely removed by sputtering. As a result, the assist ion/atom ratio must be optimized to be in the $\sim 5 \times 10^{15}$ to $\sim 1 \times 10^{16} \text{ Ar}^+/\text{cm}^2$ range shown by the yellow band in Fig. 4a. This is the dose range used by most institutions during IBAD MgO processing.

We next initiated rapid thermal anneal studies of MgO crystals to determine how orientation influences damage recovery. Fig. 5 shows the results of this study for an Ar^+ dose of $1 \times 10^{15} \text{ Ar}^+/\text{cm}^2$ and an anneal time of 3 minutes. We found that the annealing of interstitial defects was more effective than that of extended defects. The amount of recovery was also greatest for (110) oriented samples - independent of damage criterion. This latter point corroborates theoretical prediction of Uberuaga (Phys. Rev. Lett. 92 (2004) 115505).

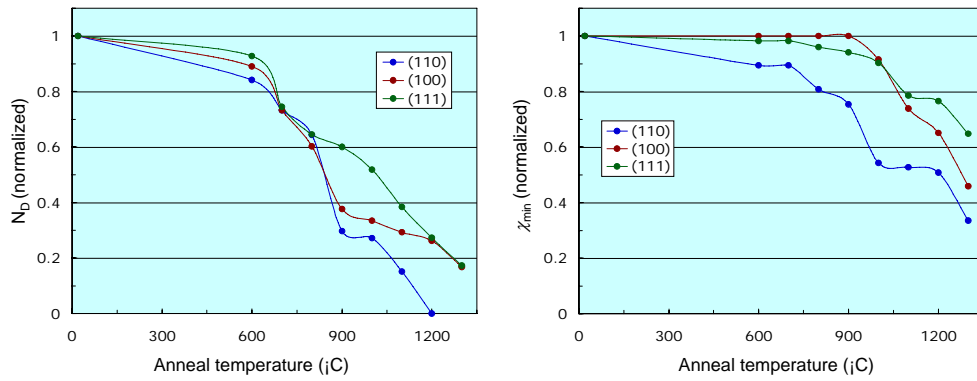


Fig. 5. The number of interstitial defects ND (left) and normalized channeling yield (characterizing extended defects) (right) as a function of annealing temperature for MgO single crystals irradiated to $1 \times 10^{15} \text{ Ar}^+/\text{cm}^2$ and annealed for 3 minutes.

It is also very clear that the type of nucleation layer greatly influences the IBAD MgO film growth. Fig. 6 shows that the in-plane texture and c-axis tilt are both numerically much smaller for MgO on Y_2O_3 compared to on $\alpha\text{-Si}_3\text{N}_4$. Examination of HRTEM cross sections of the films (Fig. 7) shows very different growth characteristics for the two nucleation layers. For IBAD MgO on $\alpha\text{-Si}_3\text{N}_4$, there is planar alignment within the first few monolayers and only slight roughness at the interface. The MgO grains are $\sim 10 \text{ nm}$ in size. In contrast for the IBAD MgO film on the planar alignment is not seen until about 20 layers have been deposited, and the interface is rougher. The grain size here is $\sim 2 \text{ nm}$.

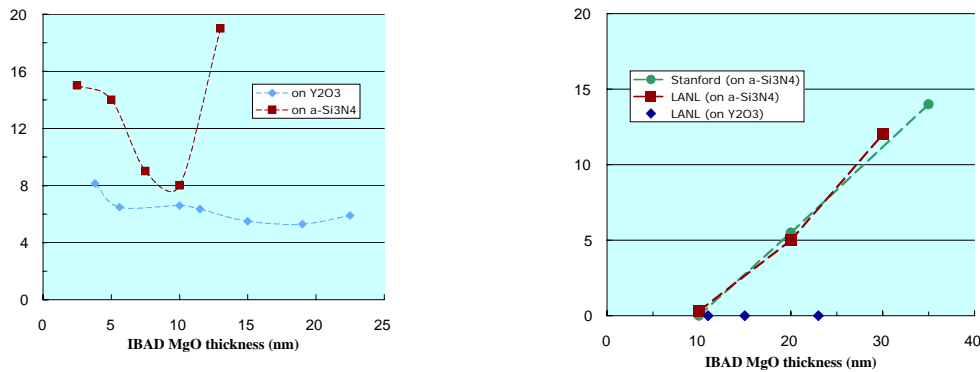


Fig. 6. In-plane texture (FWHM) (left) and c-axis tilt (right) as a function of IBAD MgO film thickness for the nucleation layers Y_2O_3 and $\alpha\text{-Si}_3\text{N}_4$.

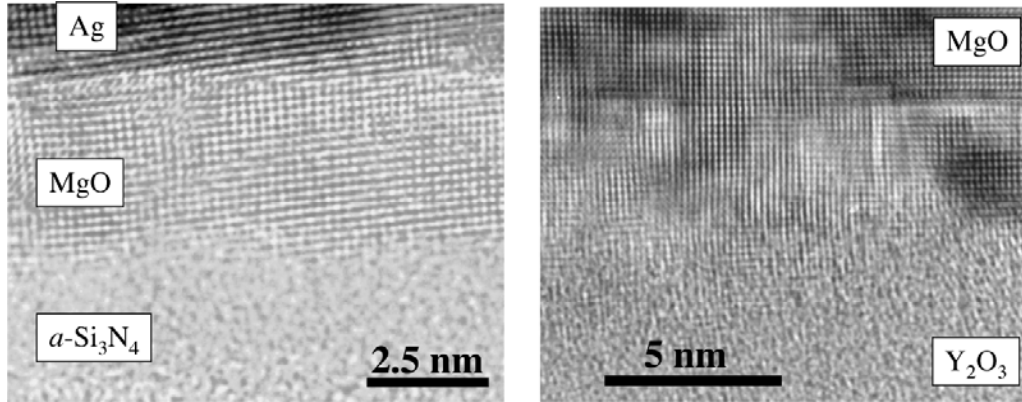


Fig. 7. HRTEM cross sectional images of IBAD MgO layers on two different nucleation layers.

HRTEM also shows that the yttria nucleation layer is nanocrystalline, as shown in Fig. 8. Under IBAD deposition conditions, differing sputter yields of Y_2O_3 and nascent MgO grains are thought to result in increased roughness of the interface prior to the transition to (100) oriented MgO. This results in smaller, more numerous grains in the early IBAD growth stages relative to the films grown on $a-Si_3N_4$.

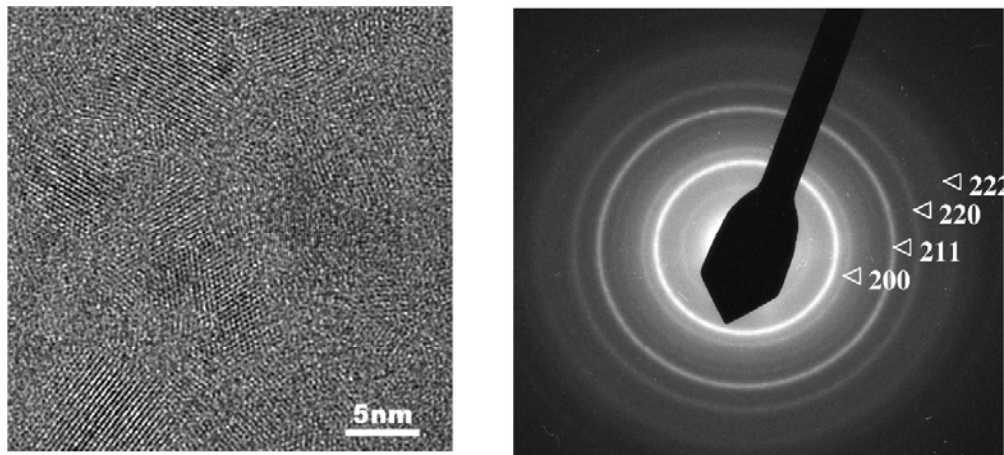


Fig. 8. Plan view of 10 nm thick Y_2O_3 film (left), and SAD pattern of the Y_2O_3 nucleation layer (right) also showing random orientation.

We interpret these observations as follows. The buildup of defects is thought to be responsible for c-axis tilt of films on $a-Si_3N_4$. The defects are mobile and annihilate efficiently on grain boundaries and film surfaces. Since the initial IBAD MgO grains on Y_2O_3 are smaller, the probability for annihilation of defects is enhanced. Thus, the onset of the c-axis tilt for the IBAD is delayed when Y_2O_3 is the nucleation layer.

Now, turning our attention to temperature dependences, the difference in damage accumulation for the three orientations was greatest at the lowest implant temperatures (Fig. 9a), which prompted a study of IBAD MgO texturing vs. deposition temperature, with results shown in Fig. 9b. The stationary substrates were held at fixed temperatures by silver pasting to a copper block during the deposition. The deposition rate was held constant for all cases. Non-weak linked YBCO properties (large J_c , good field dependence) were demonstrated for IBAD MgO templates with $\Delta\phi \leq 8^\circ$ FWHM [S.R. Foltyn et al., Appl. Phys. Lett. 82, 4519 (2003)]. Thus, the results indicate that cooling of the metal substrate during reel-to-reel deposition will expand the processing window.

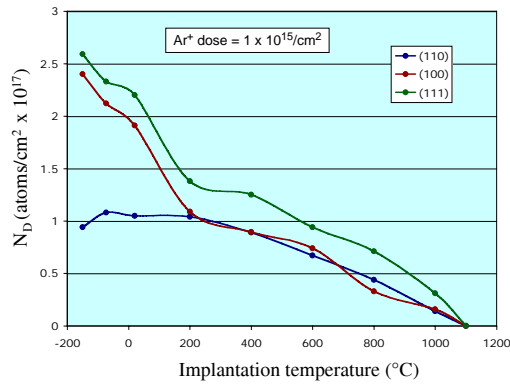


Fig. 9a. Number of interstitial atoms as a function of implantation temperature.

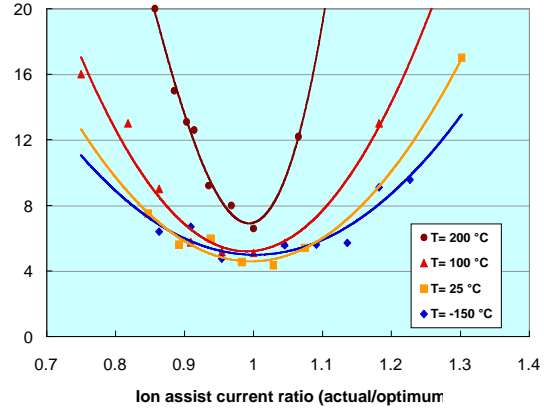


Fig. 9b. In-plane texture as a function of ion assist current ratio for various temperatures.

The ion-assist beam current density and the film thickness variations along the deposition zone are known to affect IBAD MgO film texture. Fig. 10a shows the deposition system, and Fig. 10b illustrates the variation in several parameters along the deposition zone. These results also reinforce the desirability to cool the substrates during reel-to-reel operation, as seen in Fig. 9b, before attempting to increase the deposition zone length.

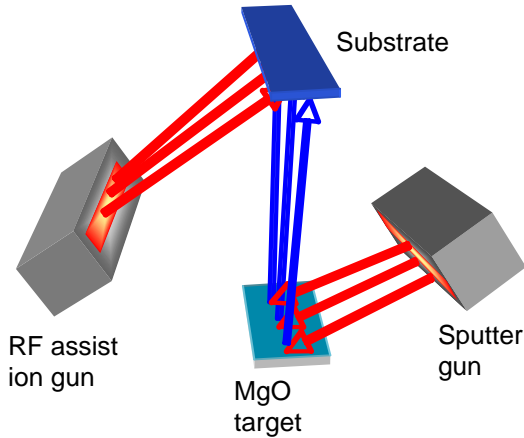


Fig. 10a. Schematic of IBAD deposition system.

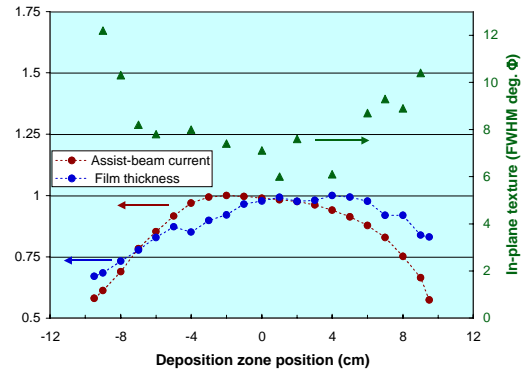


Fig. 10b. Film thickness, assist beam current, and in-plane texture along the deposition zone. $T_{\text{dep}} \sim 150^\circ\text{C}$.

Moving substrates can actually be cooled to the lower, more desirable IBAD processing temperatures using a cooling block, engineered to enhance contact with the moving tape. The ion-assist beam (I_B , V_B) was set for SuperPower's IBAD processing conditions. The tape temperature (Fig. 11a) was measured while it was moving continuously along the length of the deposition zone. Next, the texture as a function of ion assist current for depositions at different temperatures was measured to see if it was consistent with the data taken in stationary mode. In these measurements, Fig. 11b, the deposition rate was held constant and the assist rate was varied to optimize the texture. Indeed, the texture is improved for depositions at the lower temperature, even for a longer zone.

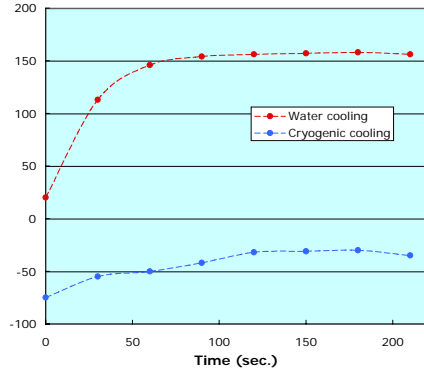


Fig. 11a. Temperature of moving tape during IBAD MgO deposition as a function of time.

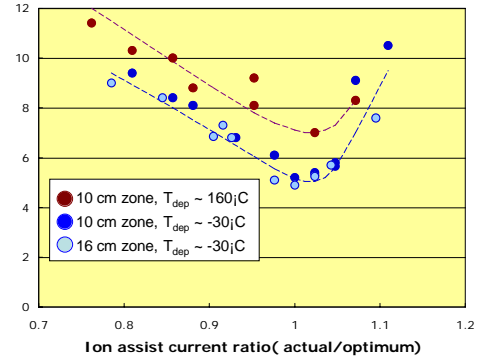


Fig. 11b. Film thickness, assist beam current, and in-plane texture along the deposition zone. $T_{\text{dep}} \sim 150^\circ\text{C}$.

To summarize this study, at the lower deposition temperature: the IBAD MgO processing window ($\Delta\phi < 8^\circ$) expands by about a factor of 2, and, overall, $\Delta\phi$ is $\sim 2^\circ$ lower. The result is a more robust IBAD MgO process such that the manufacturing yield and quality is improved.

We have also investigated the tolerance of YBCO for one of the substrate's transition metals, Ni. To accomplish this, 200 nm thick YBCO films were produced by pulsed laser deposition using YBCO targets with and without a small wedge of Ni foil, as shown in Fig. 12a. T_c and J_c were measured in the usual fashion, and the Ni concentration was measured using Particle Induced X-ray Emission (PIXE). Below about 0.25 at.% there was no affect on the superconducting properties of YBCO (Fig. 12b).

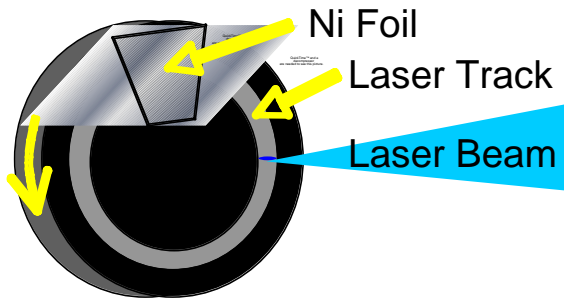


Fig. 12a. Schematic of PLD target with Ni foil wedge.

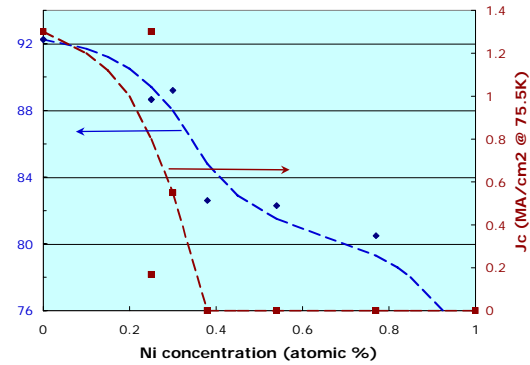


Fig. 12b. T_c and J_c as a function of Ni concentration in 200 nm thick YBCO films.

LANL has been developing the MIST (Magnetic Imaging of Superconducting Tape) method of measuring the local magnetic field across the width of a current carrying superconducting tape and then using Maxwell's laws to calculate the current distribution. Recently, the algorithm has been modified to provide a more accurate and rapid interpretation of local I_c values from magnetic imaging data. Fig. 13 shows that the current profile is now more physically realistic, with zero current in free space outside the tape. Such a technique is now amenable to on line implementation in a reel-to-reel measurement system.

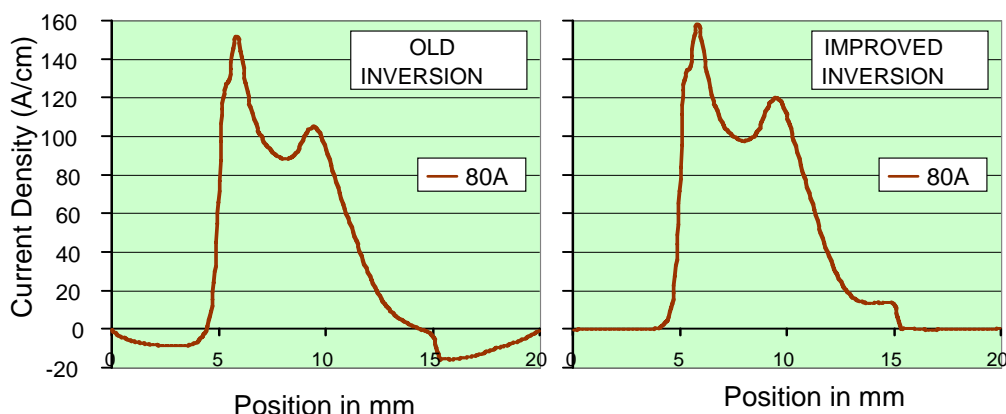


Fig. 13. Current distribution as a function of position across the width of a superconducting tape with a transport current of 80 A.

SuperPower also supplied a 9 m length of 4 mm wide coated conductor tape to LANL for winding into a small coil (Fig. 14). This coil was 7.5 cm long 2.85 cm ID and 3.3 cm OD. It was composed of 6 layers with 16 turns per layer, insulated by Kapton film and showed no degradation in its I_c of 100 A/cm after winding. The coil was capable of generating a field of 0.12 T at 64 K.

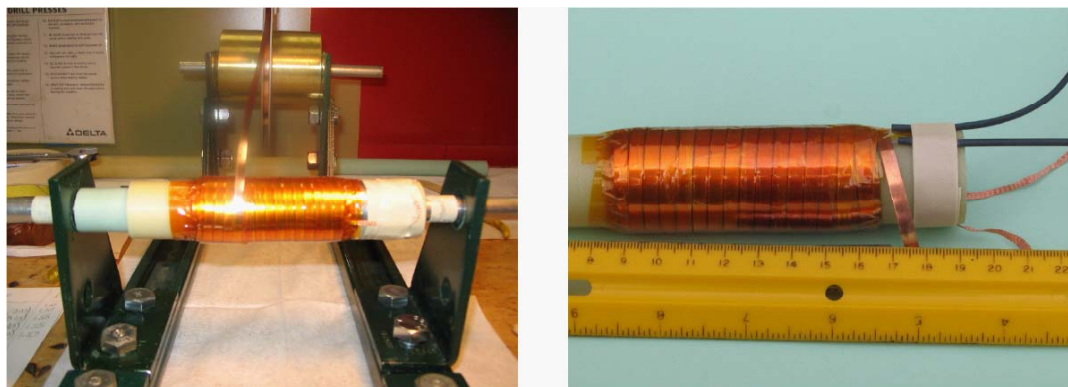


Fig. 14. SuperPower MOCVD YBCO/IBAD MgO coated conductor wound into a coil at LANL. Coil being wound (left) and completed (right).

We now summarize our work with SuperPower in support of their development of coated conductors. We succeeded in replacing two buffer layers with a single layer (RE-Zr oxide) that is compatible with SuperPower's high rate reactive sputter processing. We refined our damage anisotropy data (the (100) and (111) orientations of MgO are removed faster than the (110)) - correlating experimental annealing anisotropy data with theoretical prediction. We determined that using Y_2O_3 as the nucleation layer leads to reduced c-axis tilt and better in-plane texture. We improved our understanding of IBAD MgO texturing mechanisms, leading to improved texture in a deposition zone twice as long. In particular we showed that IBAD deposition at a lower temperature results in less sensitivity to the ion assist ratio and better in-plane texture. We determined that Ni metal diffusing from the substrate had little effect on T_c or J_c for concentrations < 0.25 at. %. We developed a transport current algorithm to interpret magnetic imaging data that is faster and more accurate than previously. Finally, we wound a small coil from 9 m of SuperPower MOCVD YBCO/MgO IBAD tape and produced a field of 0.12 T at 64 K.

2.12 Self field and in-field performance enhancement for coated conductors

S.R. Foltyn, L. Civale, H. Wang, B. Maiorov, Q.X. Jia, P.N. Arendt, J.L. MacManus-Driscoll (also at Cambridge Univ.), J.R. Mantei (also at Univ. Wisconsin-Madison), Y. Li, Y. Lin, and M.P. Maley

Many problems related to the critical current density J_c performance of coated conductors have been solved. Examples of these are the extremely high self-field J_c of very thin films, 7 MA/cm², already 10% of the depairing current, the theoretical upper limit for J_c , and further improvements are unlikely. Another example is the J_c of IBAD MgO-based coated conductors, which is the same as that for YBCO on single-crystal substrates, and therefore is not limited by grain boundaries imposed by the IBAD MgO. However, two important areas of coated conductor performance still require improvement. These are the thickness dependence and the field dependence of J_c , as illustrated in Fig. 15.

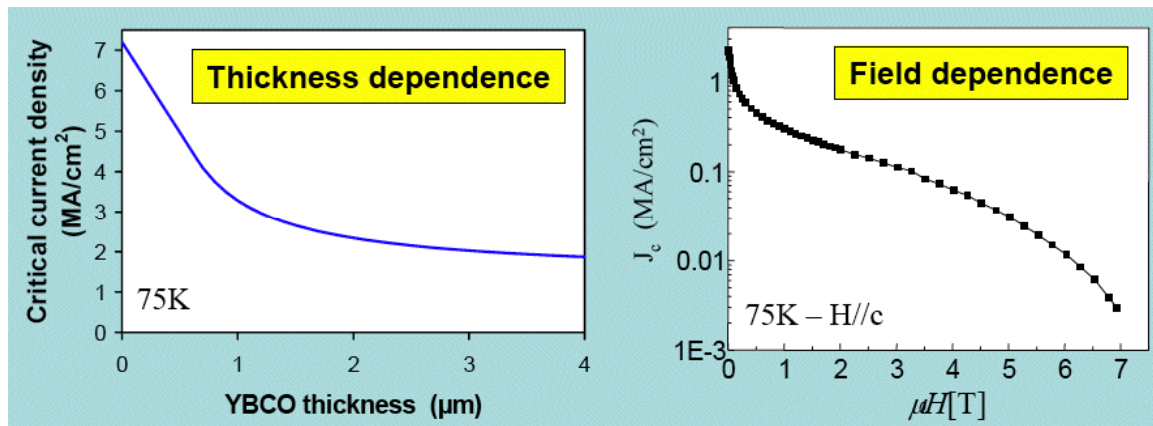


Fig. 15. Critical current as a function of film thickness (left) and of applied magnetic field H/c for IBAD MgO coated conductors.

Recently we were able to show that multilayer coated conductors could have I_c values above 1000 A/cm-width, Fig. 16. This figure shows a comparison of I_c s for single layer films with that achieved with multilayers composed of six 0.55 μm thick YBCO layers with intervening CeO_2 layers. Here the arrow indicates starts from the expected J_c of 4.75 MA/cm² for a single 0.55 μm YBCO layer to the measured J_c of 4.0 MA/cm² for the six layer, 3.5 μm thick multilayer with an I_c of 1400 A/cm width.

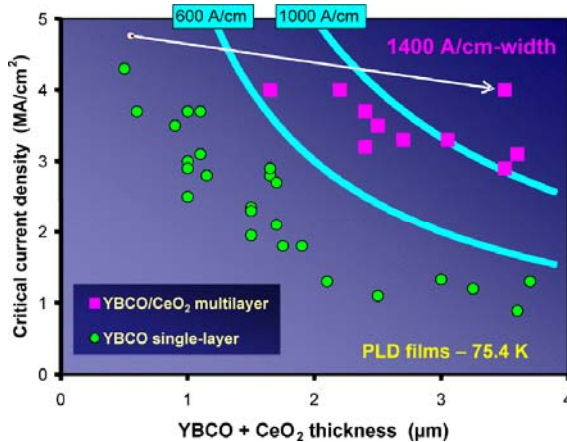


Fig. 16. Critical current density as a function of total film thickness for single layer and multilayer films.

To investigate how multilayers work, we developed a model for the incremental j_c within a film. A schematic of this model is shown in Fig. 17a. In the model, the highest value of j_c is at the film-substrate interface. Then j_c is a function of the distance from the substrate, z , decreasing to a constant value at a distance z_r . By applying this model to a set of experimental data for films of different thicknesses (Fig. 17b), the fit is found to be good, and the value of z_r can be determined. We recently validated this model by comparing it with actual $j_c(z)$ obtained from ion-milling data, as shown in Fig. 17c. In this experiment, the I_c of the film is measured, a thin layer is removed by ion milling, and the I_c of the remainder is measured. The change in I_c is then calculated, the layer thickness is measured, and the J_c of the layer [= $j_c(z)$] is measured. This is repeated until $t=0$ is reached.

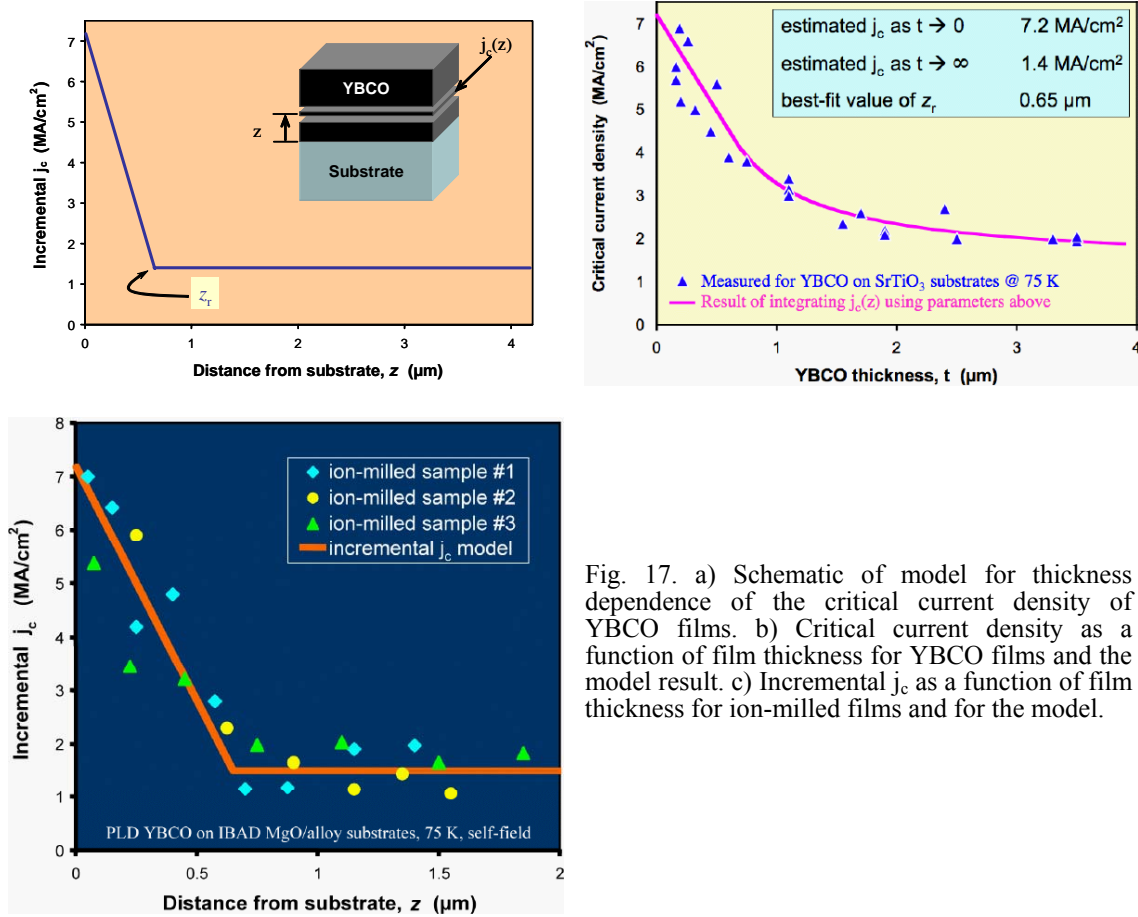


Fig. 17. a) Schematic of model for thickness dependence of the critical current density of YBCO films. b) Critical current density as a function of film thickness for YBCO films and the model result. c) Incremental j_c as a function of film thickness for ion-milled films and for the model.

The next step is to investigate three possible explanations for the shape of the incremental j_c function. The first hypothesis is that the j_c is a result of microstructural changes: the microstructure quality decays with distance from the substrate and then becomes constant above z_r . The second hypothesis is that for thin films, the pinning is two dimensional (2D) in character, and then above z_r , this changes to 3D collective pinning. The third hypothesis is that there is an interfacial influence, which decreases with distance from the substrate, and then the film becomes characteristic of "typical" YBCO.

The first hypothesis was tested by taking plan view SEM micrographs on the surface of thick single layer and multilayer films, Fig. 18. These showed that the morphology of the surface for multilayer films using either SmBCO or CeO₂ films was improved over that for a single layer YBCO film. The substrates are IBAD MgO on Hastelloy C276.

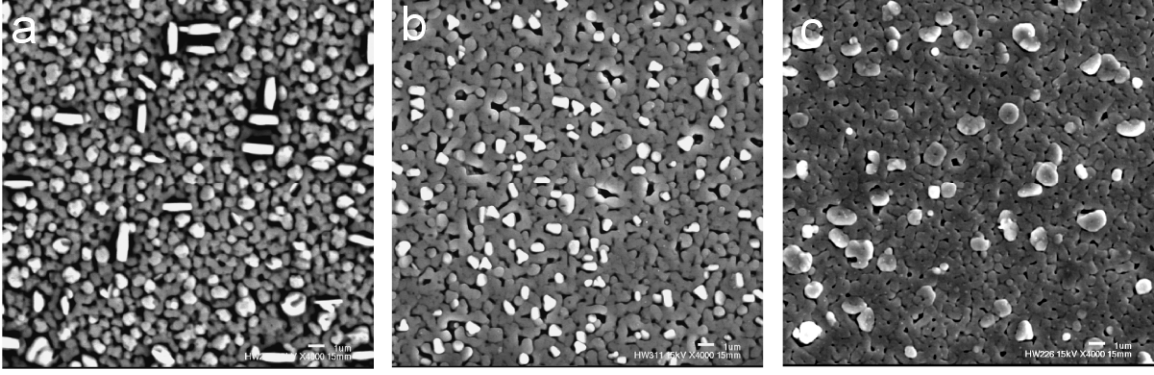


Fig. 18. SEM plan view image of a 25 x 25 μm square region of a film surface for a) a 3.7 μm thick single layer YBCO film, b) a 3.2 μm thick YBCO/SmBCO 6-layer multilayer, and c) a 3.1 μm thick YBCO/CeO₂ 6-layer multilayer film.

The difference between the results using SmBCO and CeO₂ buffer layers suggests that morphological improvement does not strongly affect $J_c(t)$. As a test, we replaced CeO₂ interlayers with SmBCO, keeping all other process conditions as constant as possible. The result was that the YBCO/SmBCO multilayers have J_c values more like that of the YBCO single layers than that of the YBCO/CeO₂ multilayers, Fig. 19a. The microstructure does deteriorate with increasing film thickness, but it tends to do so linearly with thickness, unlike the J_c dependence. Fig. 19b shows that linear dependence in the rocking curve peak width. We find similar results for the variation with film thickness for 45° rotated YBCO grains, RBS channeling, film density, and average screw dislocation.

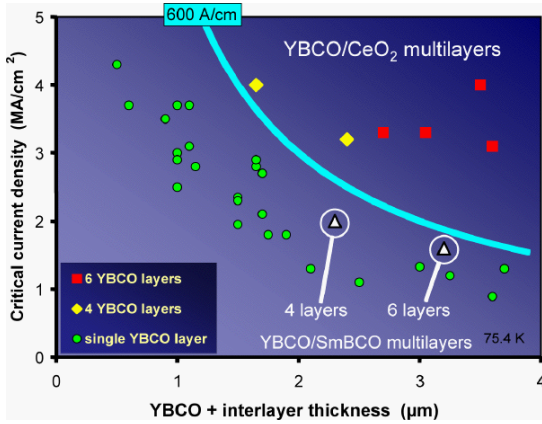


Fig. 19a. Critical current density as a function of YBCO film thickness for single YBCO layers and both YBCO/CeO₂ and YBCO/SmBCO multilayers.

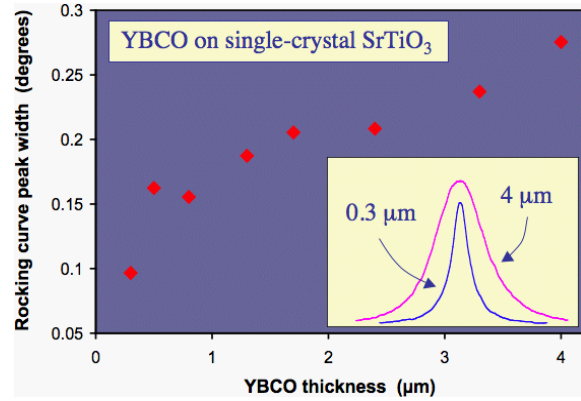


Fig. 19b. Rocking curve peak width as a function of YBCO film thickness.

A second potential explanation for $J_c(t)$ is a 2D to 3D crossover in the collective pinning regime. In a model presented by A. Gurevich, et al., at the DOE 2004 Annual Peer Review, short vortices in thinner films (Fig. 20a) are rigid and cannot easily accommodate to random pinning sites; J_c is proportional to $t^{-1/2}$ (Fig. 20b). Longer vortices in thicker films (Fig. 20c) can more easily flex to intersect random pinning sites, and J_c is a constant.

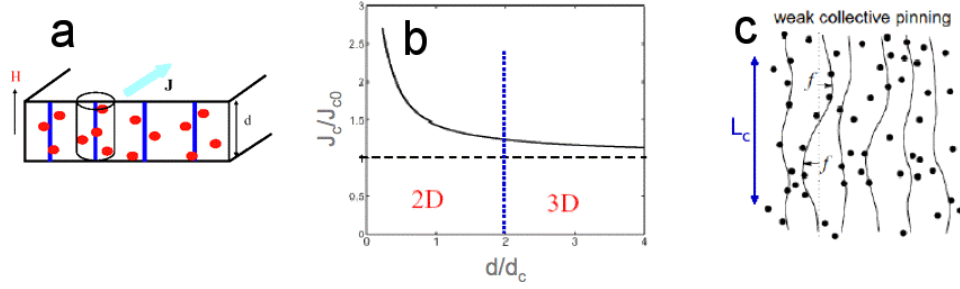


Fig. 20. a) Schematic of straight vortices in a thin film. b) Normalized thickness dependence of J_c in the model. c) Schematic of flexible vortices in a thick film.

To test this hypothesis it is necessary to isolate and measure slabs of YBCO from a thick film, because in the 2D-3D model, J_c is determined by the YBCO thickness and will be constant regardless of the slab's location in the film. Since it is not possible to remove a slab of YBCO and measure it, we need to deposit films on "invisible" spacer layers having the properties of not being superconducting, and of having a perfect lattice match to YBCO. PrBCO closely matches the invisibility criterion, so we made a series of bilayers with varying PrBCO thicknesses (Fig. 21). In this way the nonsuperconducting PrBCO isolates the vortices from the defect-rich interface. The PrBCO/YBCO interface is nearly homoepitaxial and relatively free of defects (Fig. 21, right).

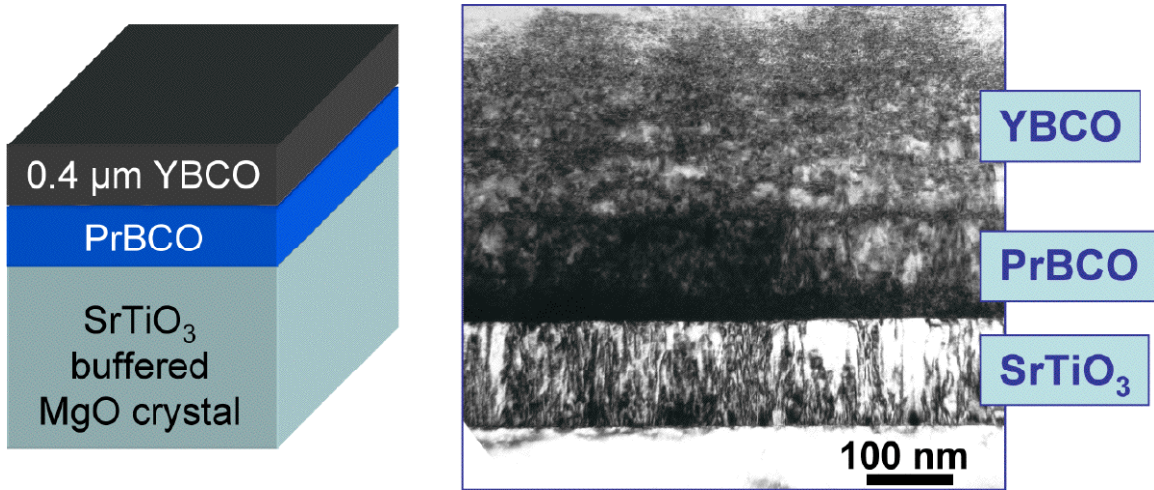


Fig. 21. (Left) Schematic of bilayer films with PrBCO layer and (right) TEM micrograph of layers.

However, the constant J_c s predicted by the 2D-3D crossover model are not observed in the PrBCO/YBCO bilayers (Fig. 22a). Instead, if we calculate J_c of the bilayer films based on the incremental j_c function (Fig. 17a), noting that the YBCO layer starts at a distance from the substrate determined by the PrBCO layer thickness, the experimental results match the calculation (Fig. 22b) suggesting that $J_c(t)$ is interface related.

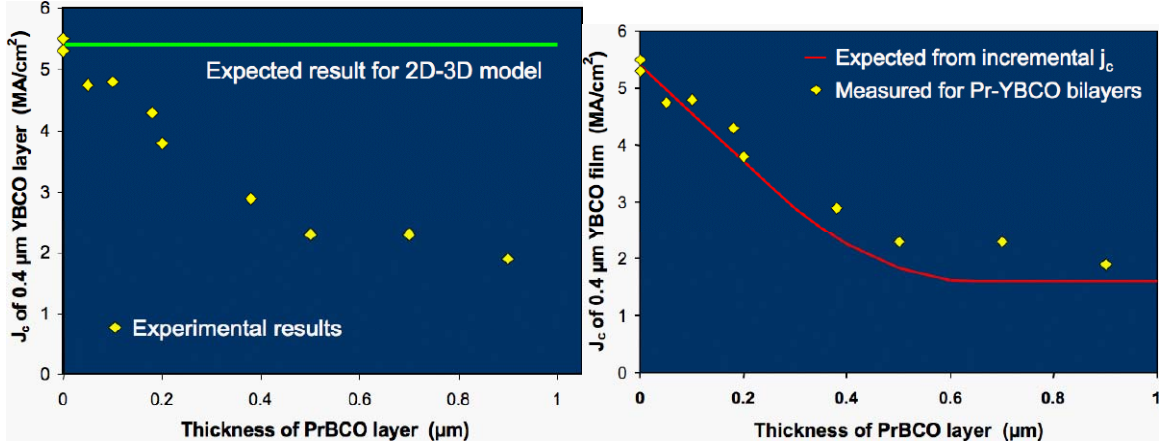


Fig. 22a. J_c for a YBCO/PrBCO bilayer and results of 2D-3D model as a function of PrBCO layer thickness.

Fig. 22b. J_c for a YBCO/PrBCO bilayer and results from incremental j_c model as a function of PrBCO layer thickness.

The importance of the interface is further supported by adding a CeO_2 layer between the PrBCO and the YBCO. The CeO_2 layer "restores" J_c to the level of a 0.4 μm YBCO single layer film, as shown in Fig. 23.

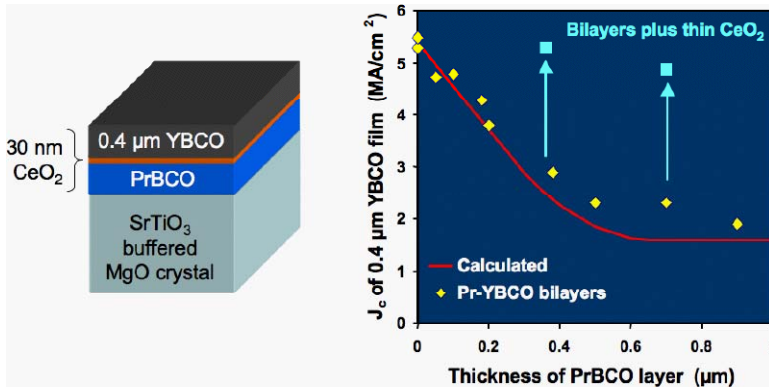


Fig. 23. Schematic of stacking sequence and results on J_c of added a CeO_2 layer to the PrBCO/YBCO bilayer film.

Having identified that pinning is related to the interface, the detailed microscopic source of the strong pinning needs to be identified. Fig. 24a shows two possible types of defects that might be responsible for the $J_c(t)$ in YBCO. The dark band at the YBCO/buffer interface indicates a higher density of defects that could produce strong pinning at the film-substrate interface. The threading dislocations between growth columns are the kind of defects that can give rise to the constant $j_c(t)$ observed beyond 0.65 μm. Fig. 24b shows that the dark band is due to misfit dislocations at the interface.

The dislocations are deduced to be parallel to the YBCO b axis because of the larger misfit with the a axis. The misfits between the STO lattice and the YBCO a- and b axes are -2.4% and -0.7%, respectively. Fig. 25a shows TEM plan views of these misfit dislocations. The observed ~17 nm spacing is consistent with the presence of a-axis dislocations. These dislocations have also been observed at the YBCO- CeO_2 interface. Since the a axis has two possible orientations, misfit dislocations form a net that seems ideal for strong pinning. Fig. 25b shows two adjacent growth islands in a YBCO film. The a and b axes for the two islands are rotated 90 degrees with respect to one another, and the misfit locations in each island are orthogonal.

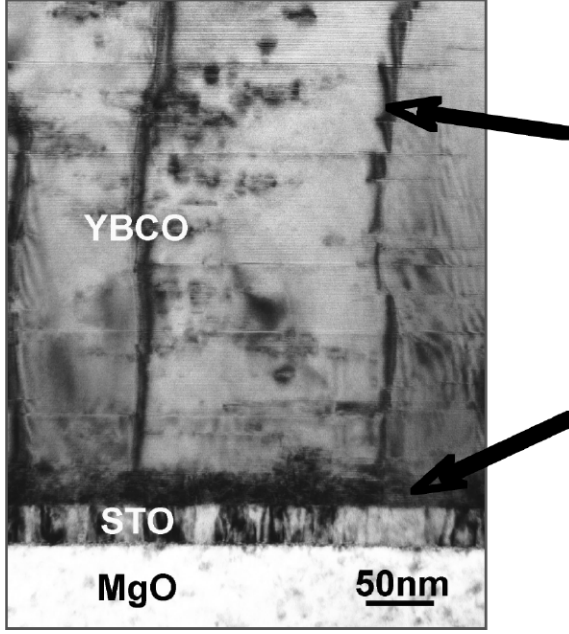


Fig. 24a. TEM micrograph of PLD YBCO on STO-buffered single crystal MgO showing a high density of defects near the interface (lower arrow) and threading dislocations parallel to the columnar grain boundaries.

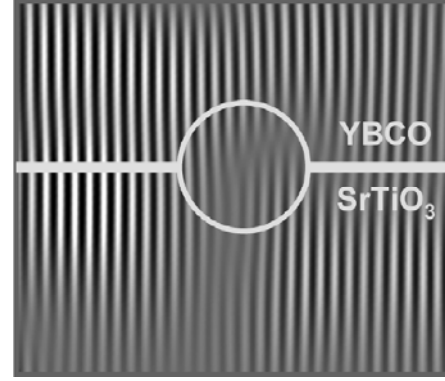


Fig. 24b. Fast Fourier filtered image of a high-resolution cross section of the dark band in Fig. 10a indicating the presence of misfit dislocations.

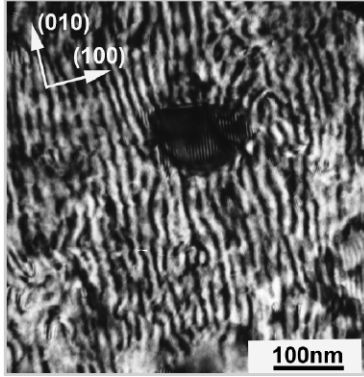


Fig. 25a. TEM plan view images of a ~20 nm thick YBCO film on a STO single-crystal substrate. Observed dislocation spacing is ~17 nm.

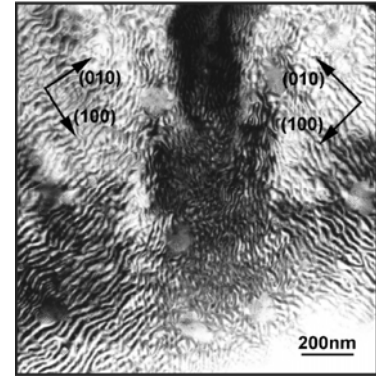
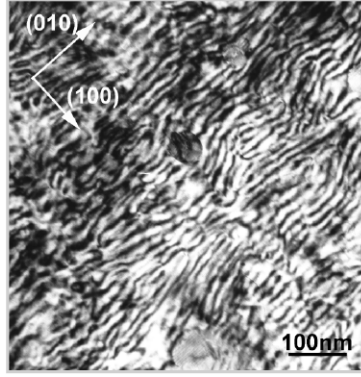


Fig. 25b. TEM plan view showing two adjacent growth islands in a 20 nm thick YBCO film on STO.

However, strong pinning by the dislocation cores is inconsistent with the PrBCO bilayer experiment, Fig. 22 and 26, for which the pinning enhancements extend much farther into the film than the thickness of the defected layer. The results in Table 1 show that for a variety of substrates, the range (parameter z_r) has changed little over time.

We conclude at this point that the evidence is not yet sufficient to determine whether microstructural decay causes the J_c thickness dependence. The SmBCO and CeO₂ interlayers both improve film morphology and texture, but the multilayers have very different J_c values. Sometimes, the apparent correlations between J_c and microstructure can be misleading. For instance, the rocking curve peak width for a 1.6 μm thick YBCO film on a single-crystal substrate is $\sim 0.25^\circ$ and on IBAD MgO it is more than 3 times

larger, 0.8° , yet the J_c values are the same. We also conclude that intrinsic effects, such as a 2D-3D crossover are also not responsible for the J_c thickness dependence. In bilayer experiments, J_c of a $0.4\ \mu\text{m}$ YBCO layer should be independent of the PrBCO thickness, and this is not the case (Fig. 22). PrBCO-based multilayers should also have J_c comparable to CeO_2 -based ones, but they do not (Fig. 27).

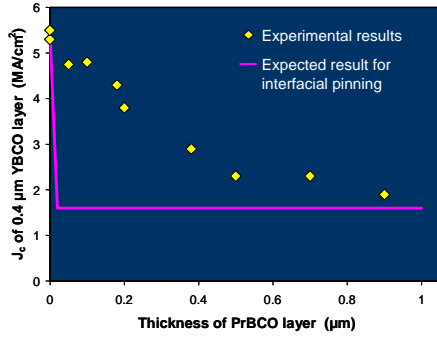


Fig. 26. Measured critical current density as a function of PrBCO layer thickness and that expected for interfacial pinning for a YBCO-PrBCO bilayer.

Table 1. Interfacial and bulk j_c and range z_r for YBCO films.

| Substrate type | Year | j_c at interface (MA/cm ²) | bulk j_c (MA/cm ²) | Range (z_r) (μm) (± 0.1) |
|--|------|--|----------------------------------|------------------------------------|
| Single-crystal YSZ + CeO_2 | 1993 | 5.5 | 0.75 | 0.65 |
| IBAD YSZ + CeO_2 | 1999 | 3.8 | 0.5 | 0.65 |
| Single-crystal SrTiO_3 and IBAD MgO + SrTiO_3 | 2004 | 7.2 | 1.4 | 0.65 |
| Single-crystal MgO + SrTiO_3 | 2005 | 7.1 | 1.6 | 0.65 |

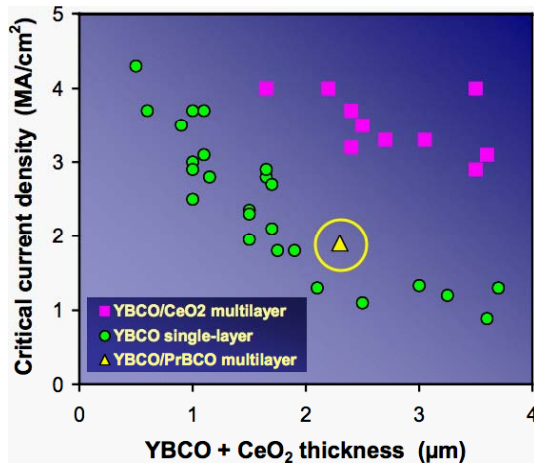


Fig. 27. J_c for YBCO single layers and YBCO/ CeO_2 and YBCO/PrBCO multilayers as a function of total multilayer thickness.

However, there is much evidence that the J_c thickness dependence is due to enhanced pinning near the interface. The highest incremental j_c occurs nearest the interface. Heteroepitaxial interfaces (e.g., CeO_2/YBCO or $\text{Y}_2\text{O}_3/\text{YBCO}$), which contain misfit dislocations, result in high- J_c multilayers. Nearly "homoepitaxial" interfaces (e.g., SmBCO/YBCO or PrBCO/YBCO), which contain relatively fewer defects, do not

increase multilayer J_c . Finally, moving YBCO farther away from the interface (with PrBCO) decreases J_c in a systematic way.

We next apply the tools of the field, angular, and temperature dependences of J_c , which allow us to identify pinning mechanisms and regimes, to investigate the thickness dependence. Three different regimes can be identified in the angular dependent pinning of YBCO (Fig. 28a). Near the ab planes, intrinsic pinning and ab -plane correlated pinning is observed; near the c axis, correlated pinning due to dislocations, twins, etc., is observed, and at all angles there is a background of random pinning that is characteristic of anisotropic scaling. Of particular importance for these analyses is $J_c(H||c)$, as shown in Fig. 28b. Below a characteristic field H_{cr} , J_c decays as a power law in H with exponent α , which is temperature independent. Above this field, J_c falls off more rapidly towards the irreversibility field H_{irr} .

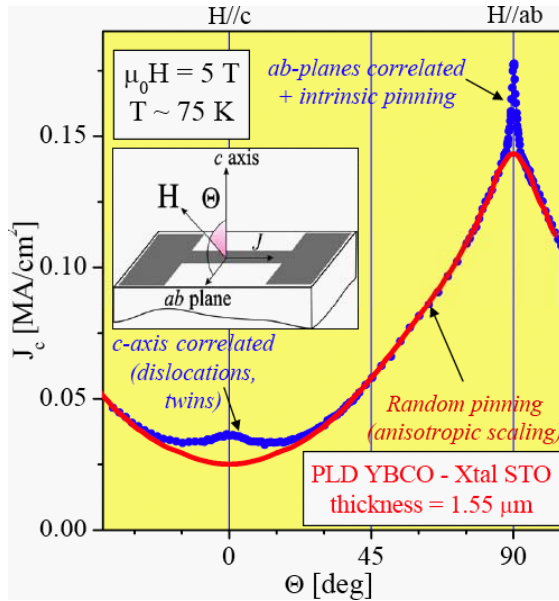


Fig. 28a. Critical current density as a function of angle for a YBCO film at 5 T and 75 K.

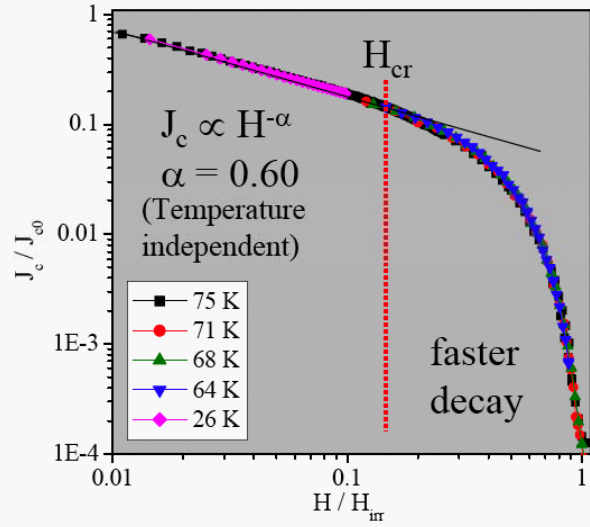


Fig. 28b. Normalized critical current density as a function of normalized magnetic field $H||c$ axis.

Ion milling of a thick PLD YBCO film from $t = 5 \mu\text{m}$ down to $0.7 \mu\text{m}$ demonstrated that the shape of $J_c(T, H, \Theta)$ remains almost the same, as shown in Fig. 29. Even though J_c changes by orders of magnitude, to a first approximation, $J_c(T, H, \Theta)_t \sim C^* J_c(T, H, \Theta)_{5 \mu\text{m}}$. In fact, curves for all thicknesses can be overlapped (Fig. 30) by just dividing by a factor, which is the same one obtained for self field (inset of Fig. 30b). This implies that the thickness dependence is not related to vortex physics.

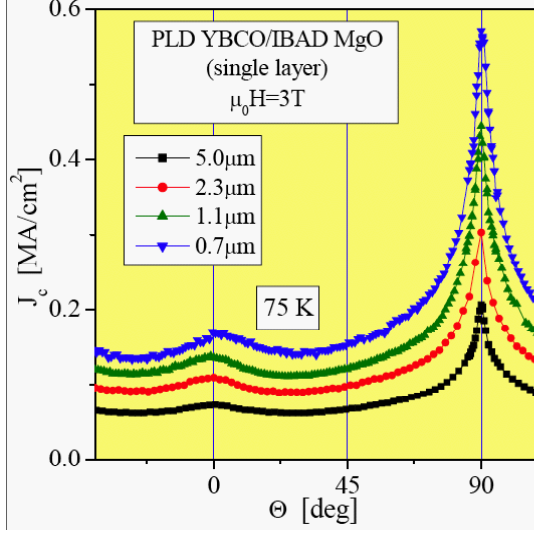


Fig. 29a. Critical current density as a function of angle for an ion milled YBCO film.

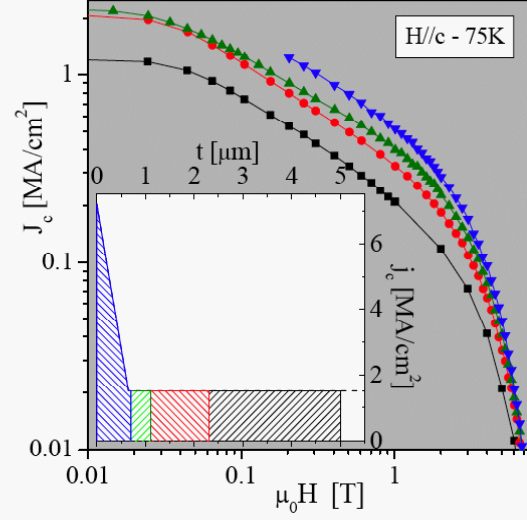


Fig. 29b. Critical current density as a function of magnetic field \parallel c. The inset shows the layer thickness removed by ion milling at each step.

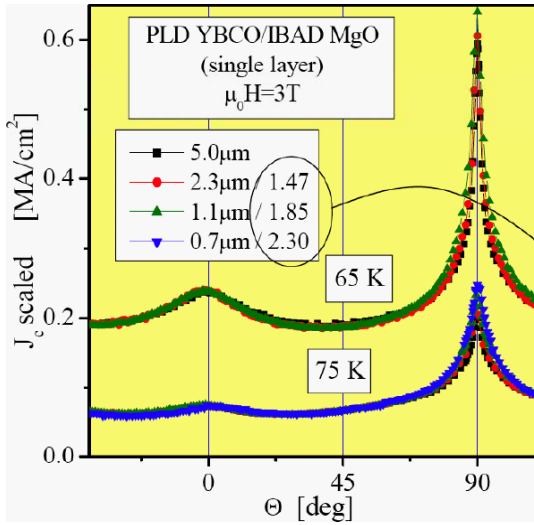


Fig. 30a. Scaled critical current density as a function of angle for the ion milled YBCO film of Fig. 29.

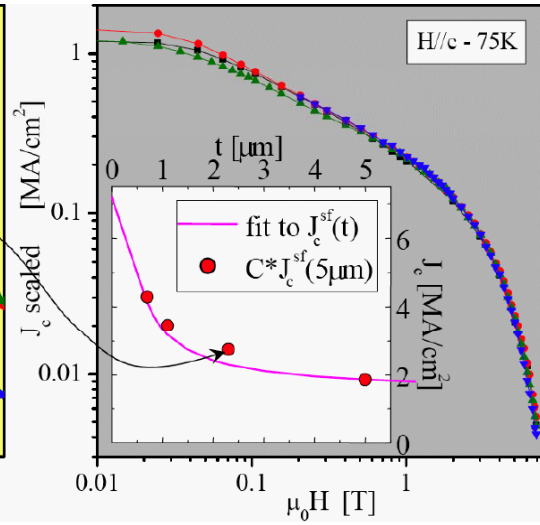


Fig. 30b. Scaled critical current density as a function of magnetic field \parallel c. The inset shows the normalization factors derived at self field.

Clearly, there are more and/or stronger defects near the interface. We can study this by looking at the angular/field dependences for YBCO directly on STO and then with an intervening PrBCO film, similar to the self-field study above (Figs. 22, 23, 26). Fig. 31 shows that for the same thickness YBCO films, the J_c s are different: the film on STO has more and/or stronger pinning centers. The films have a different dependence on Θ : additional defects close to the STO buffer are different from "bulk" defects. The fact that there are no large peaks for $H \parallel c$ and $H \parallel ab$ for the film on STO suggest that the additional defects are uncorrelated. The faster decay with H (not shown) implies that the additional defects in the film on STO are large and scarce. These infield studies put additional restrictions on the possible origin of the stronger pinning in thinner films, ruling out the possibility of the defects being correlated.

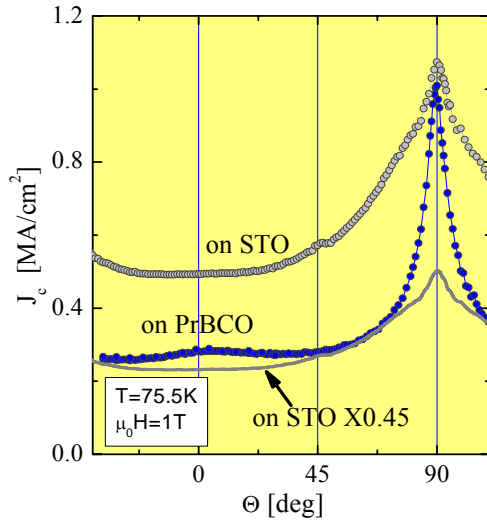


Fig. 31. Critical current density as function of angle for YBCO on STO and with an intervening layer of PrBCO.

We believe that multilayer films retain the high self-field J_c of thin films by "resetting" the interface-induced pinning (Fig. 32a). However, the real goal is to improve J_c at technologically relevant H and T . In that context, we consider the field dependence of single layer films (Fig 32b) where α parameterizes the power law decay of J_c with field.

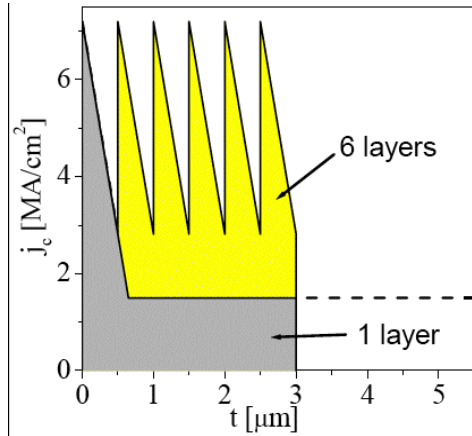


Fig. 32a. Schematic of mechanism for improvement of self field J_c of multilayer films.

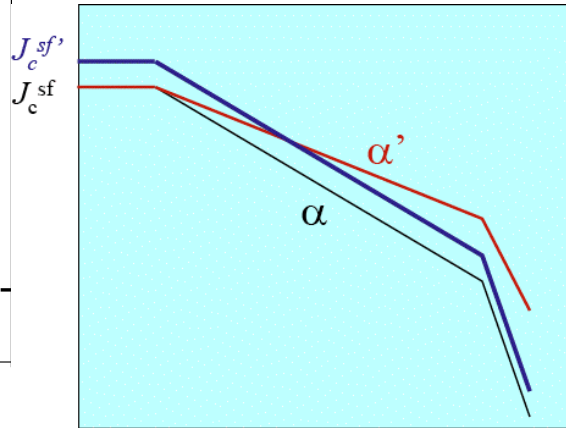


Fig. 32b. J_c as a function of field as J_c^{sf} and α change.

The α values are robust for given film deposition parameters and can be used as a characterization tool. For instance, the α for PLD YBCO is ~ 0.6 on single-crystal STO and ~ 0.45 to 0.55 on STO buffer (Fig. 33) layers as a result of measurements of many samples. Previously, we showed that the lower α value on STO buffer layers is due to pinning by dislocations associated with STO outgrowths. α values as low as ~ 0.4 can be obtained by reducing the STO deposition temperature, but at the price of reducing J_c^{sf} .

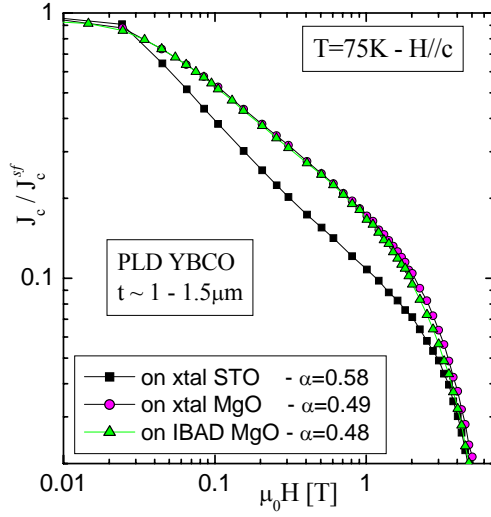


Fig. 33. Normalized J_c as a function of magnetic field for YBCO on single-crystal STO and on STO buffer layers (lower two entries in legend).

YBCO/CeO₂ multilayers (Fig. 34a) result in an in field J_c increase due to a higher J_c^{sf} with no deterioration in α . The self field J_c for single layer YBCO is 2.1 MA/cm² and 3.25 MA/cm² (880 A/cm) for a YBCO/CeO₂ multilayer. Fig. 34b shows the large I_{cs} possible and the same field dependence for 1, 4, and 6 layers and for both CeO₂ and Y₂O₃ interlayers. As an aside, the 2.2 μ m thick multilayer (Fig. 35) comfortably exceeds the value of 115 A/cm-width at 65 K and 3 T, worst orientation - this is a DOD Title III goal. A thick enough (5.5 μ m) PLD single layer film with a low enough α (0.43 using STO outgrowths) also exceeds the requirement.

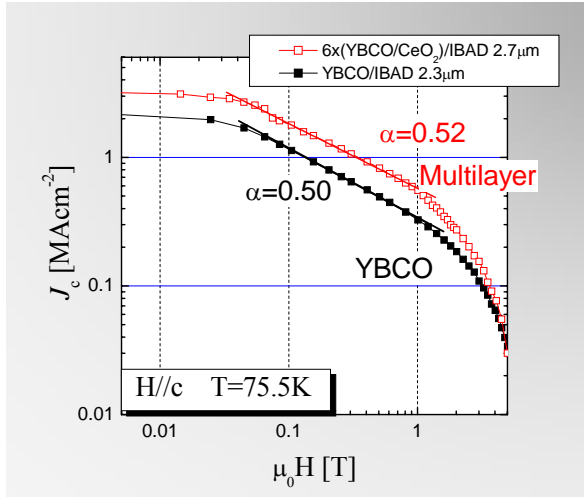


Fig. 34a. Critical current density as a function of $H||c$ for a single layer and multilayer.

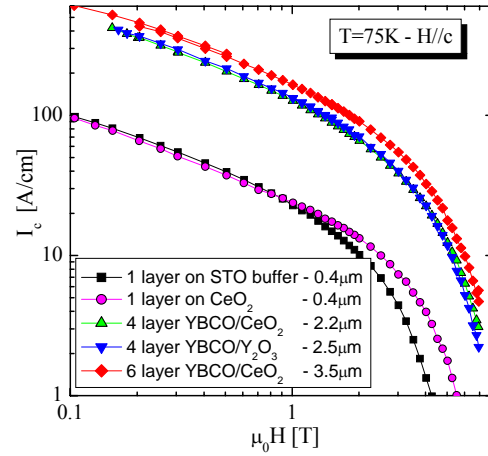


Fig. 34b. Field dependence of I_c for 1, 4, and 6 layer multilayers.

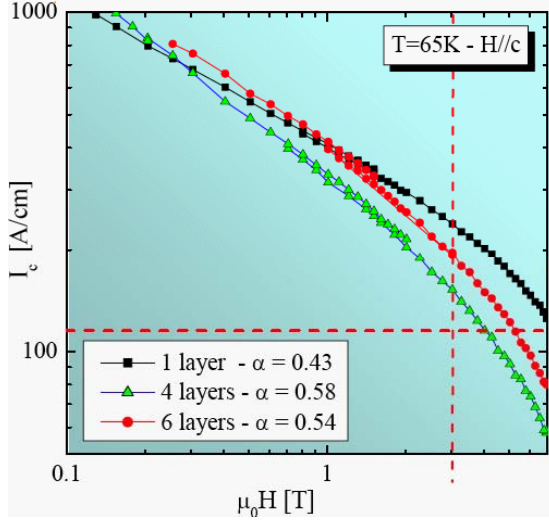


Fig. 35a. Critical current as a function of applied field $\parallel c$ for multilayer films and a single layer film with STO outgrowths.

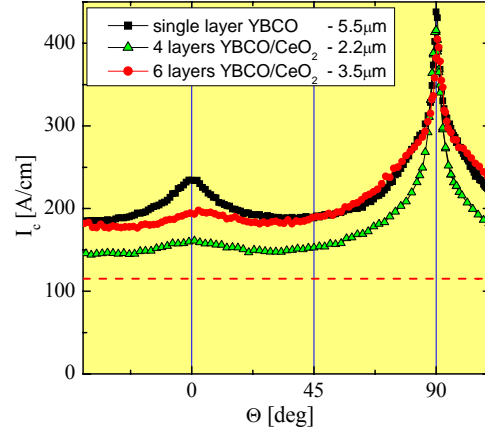


Fig. 35b. Critical current as a function of angle at 65 K and 3 T. Minimum J_c is greater than 120 A/cm-width.

Previously we have shown (Fig. 36) that the introduction of BaZrO₃ (BZO) nanoparticles results in smaller α and no significant decrease in J_c^{sf} . The α parameter decreases from ~ 0.5 - 0.6 to ~ 0.3 with BZO doping.

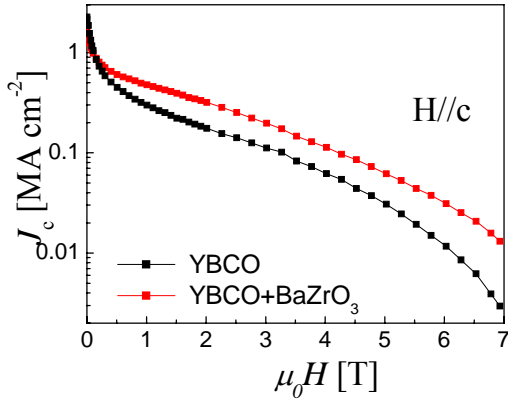


Fig. 36a. Critical current density as a function of applied magnetic field parallel to c for YBCO and YBCO doped with BZO nanoparticles.

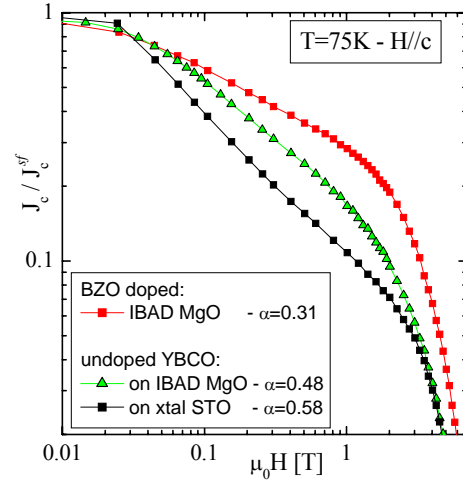


Fig. 36b. Normalized critical current density as a function of magnetic field parallel to c for BZO doped and undoped YBCO. (J.L. MacManus-Driscoll et al. Nature Materials 3, 439 (2004).

Upon further improvement in the BZO doping technique, we have obtained a record low α of ~ 0.20 , Fig. 37. This low value is directly related to the very large c -axis peak (Fig. 37a). The J_c is dominated by additional c -axis correlated defects (dislocations), and the natural anisotropy of pure YBCO [$J_c(H \parallel ab) > J_c(H \parallel c)$] can be reversed (Fig. 38a), and more importantly, without deterioration of $J_c(H \parallel ab)$. The random pinning contribution to the pinning (fine curves in Fig. 38a) is very similar for doped or undoped samples, and thus the particles themselves make only a minor contribution.

With the random pinning contribution subtracted, as shown in Fig. 38b, we see that for the undoped sample, the trapping angle ϕ_t within which vortices are pinned by the c-axis correlated defects, is $\sim 65^\circ$ for pure YBCO but nearly 85° for BZO doped YBCO. The pinning energy, as reflected in the height of the peak at 0° , is 3x to 4x higher the BZO doped sample. Finally, the peak for $H \parallel ab$ (90°) is the same as that in standard YBCO.

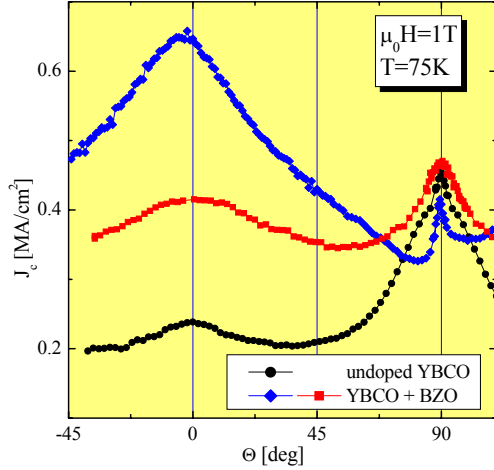


Fig. 37a. Critical current density as a function of angle for undoped YBCO and YBCO + BZO (red - early work; blue - recent result)

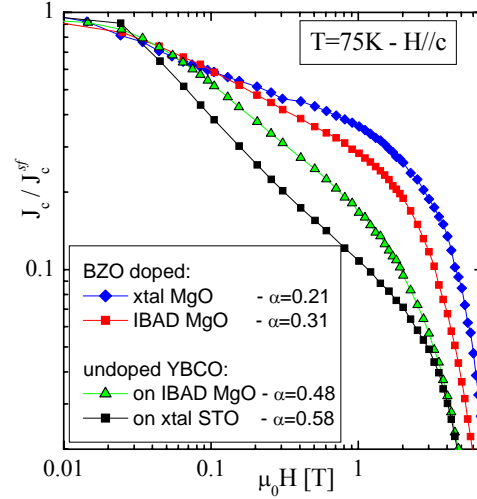


Fig. 37b. Normalized critical current as a function of magnetic field for undoped YBCO and BZO doped YBCO.

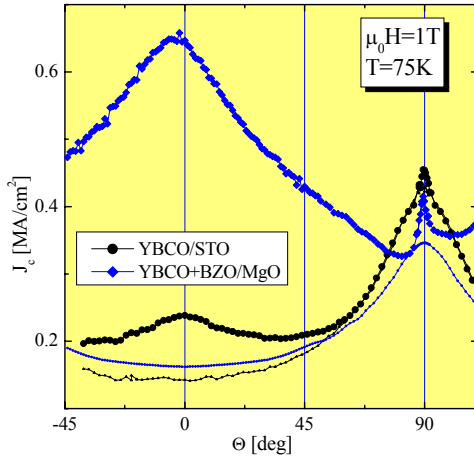


Fig. 38a. Critical current density as a function of angle for BZO doped and undoped YBCO. The finer curves show the random pinning component (from anisotropic scaling).

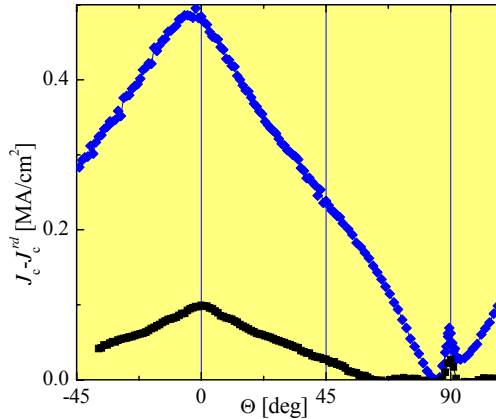


Fig. 38b. Critical current density minus the random pinning contribution for the samples of Fig. 38a.

In contrast to the behavior of BZO nanoparticles in PLD YBCO, which produce aligned defects parallel to the c axis (Fig. 38), the nanodots produced by adding Er to MOD YBCO produce a splayed-like strain field (Fig. 39a) reduce the ab plane peak and produce a very broad, flat nearly isotropic J_c as a function of angle.

Defect Model

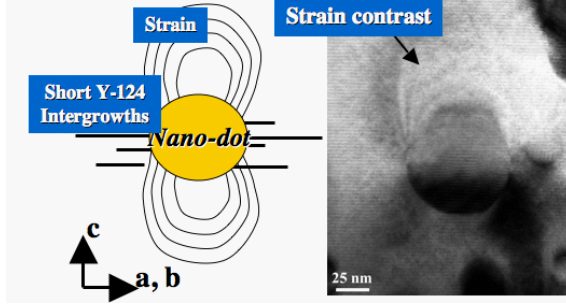


Fig. 39a. Schematic and micrograph of defect model for Er additions in MOD YBCO.

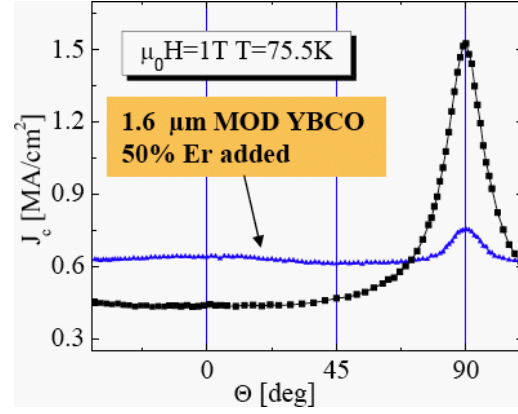


Fig. 39b. Critical current density as a function of angle for MOD YBCO with & without Er additions.

The density of c-axis correlated defects (dislocations) can be estimated from TEM images. Fig. 40a shows the defects schematically. With a mean dislocation distance d of 40 nm and dislocation length l of 120 nm, the number of dislocations that cross an ab-plane per unit area can be determined. By casting this density in terms of a "matching field" B_ϕ , for which the defect density equals the flux line density, we find that $B_\phi = \phi_0(1/d)^3 l$, where ϕ_0 is the flux quantum, is ~ 4 T. This is confirmed by the appearance of a "bump" in the irreversibility line near ~ 5 T for the BZO containing sample (Fig. 40b). Such features have been previously observed for HTS materials irradiated with heavy ions, which produce columnar defects, another type of correlated defect by Civale et al. (PRL 67, 648 (1991) and PRL 78, 1829 (1997)).

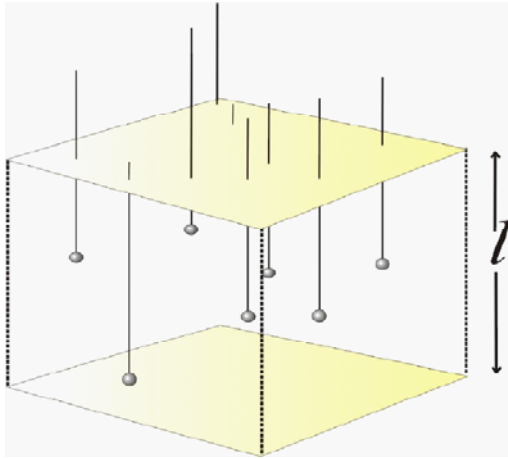


Fig. 40a. Schematic of dislocations in BZO doped YBCO, each emanating from a BZO nanoparticle. Typical dislocation separation d is 40 nm and length l is 120 nm.

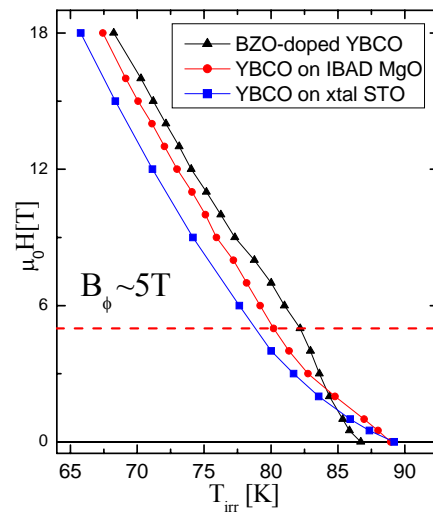


Fig. 40b. Irreversibility line for YBCO samples near 5 T showing "bump" feature near 5 T characteristic of the matching field for correlated defects.

The record low value of α (Fig. 41) is maintained at lower temperatures, as shown in Fig. 41a. In addition, this 1 μm thick film almost achieves the DOD Title III target of 115 A/cm-width at 65 K and 3 T (worst orientation).

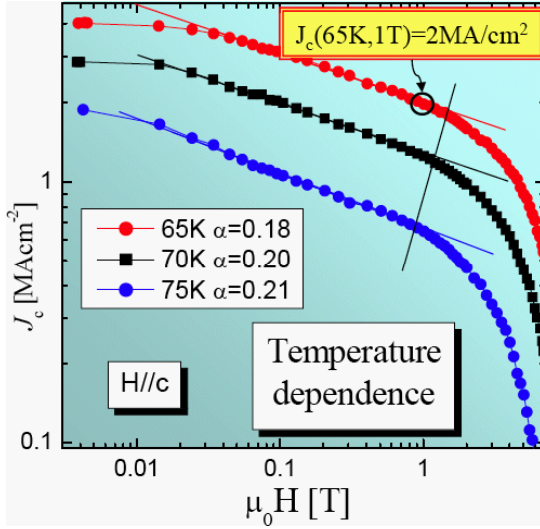


Fig. 41a. Temperature dependence of critical current density as a function of applied field $H||c$.

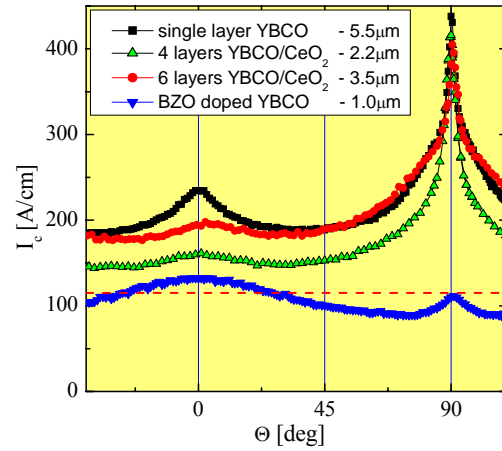


Fig. 41b. Critical current density as a function of angle for thick YBCO, multilayer YBCO and BZO doped YBCO as a function of angle at 65 K & 3 T. The dashed line is the DOD Title III target of 115 A/cm-width.

Moving now to the question of the temperature dependence of α in pure YBCO, transport measurements in liquid Ne (26 K) (Fig. 42) gave the same α values as were obtained from 65 K to 75 K. However, several open questions remain. The behavior of α in the technologically important range of 30 K to 50 K is unknown. The temperature dependence of H_{cr} is also unknown. Also, from a practical perspective, transport measurements in liquid Ne are slow and expensive and carry the risk of sample damage due to contact heating. As a result, we decided to incorporate a complementary technique: namely, that of determination of J_c by magnetization.

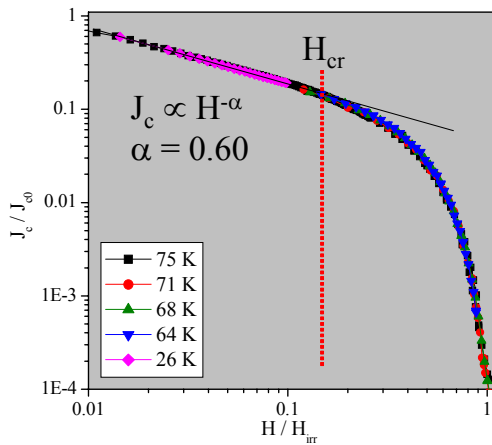


Fig. 42. Normalized critical current density as a function of normalized field for YBCO at a range of temperatures.

Magnetization measurements of J_c allow us to explore the entire temperature range from 4 K to T_c . Magnetization measurements have the additional advantages that they are fast, requiring no patterning, and there is no risk of sample damage (e.g., from contact heating). The critical state model can be used to derive from the width Δm of the magnetization loop at a particular field and temperature (Fig. 43a) the critical current

(density) (Fig. 43b) However, there are a few complications to the analysis. The magnetization has an equivalent "voltage criterion" of $\sim 10^{-10}$ to 10^{-11} V/cm, which is several orders of magnitude lower than what is achievable in transport ($\sim 10^{-6}$ V/cm). This means that the magnetic J_c is lower than the transport J_c ; this difference is significant for low n in the $V \sim I^n$ curves.

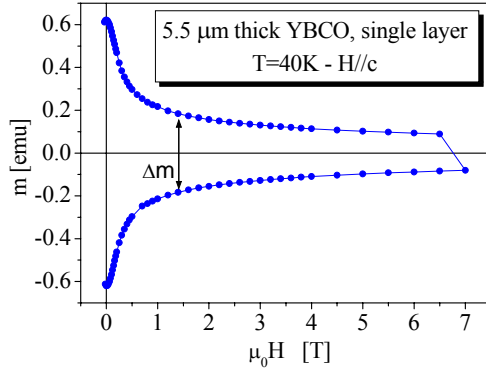


Fig. 43a. Magnetization as a function of applied field parallel to c for a thick YBCO film.

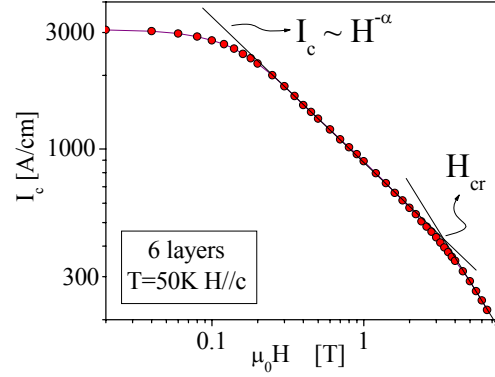


Fig. 43b. Critical current density as a function of applied magnetic field determined from magnetization data.

The magnetization and transport measurements of J_c show excellent agreement if the voltage criterion effect is corrected. The transport J_c and magnetization J_c coincide where the correction is minor (large n /low H) with the difference increasing as n decreases/ H increases (Fig. 44). The magnetization α is higher than the transport α , and the difference is small and systematic. Thus J_c and α magnetization values can be safely compared among samples. For consistency, however, the magnetization values that will be shown are real, not corrected values, and these are always equal to or lower than the corresponding transport J_c value.

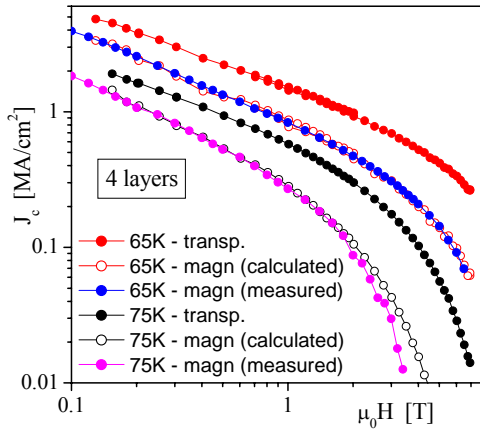


Fig. 44. Critical current density as a function of magnetic field parallel to c from transport, from magnetization, and from magnetization corrected for voltage criterion.

Using this magnetization technique, it is now possible to obtain maps of J_c , α , and H_{cr} over large regions of temperature and magnetic field (Fig. 451a). Fig. 45b shows the temperature dependences of the power law exponent α and the magnetic field parameter H_{cr} . Note the deviation between the transport and magnetization results for α at high temperature; this is where the n value is small and the voltage criterion effect is important. Also, because of the limited maximum magnetic field of 7 T, it was not possible to determine H_{cr} for temperatures below 40 K.

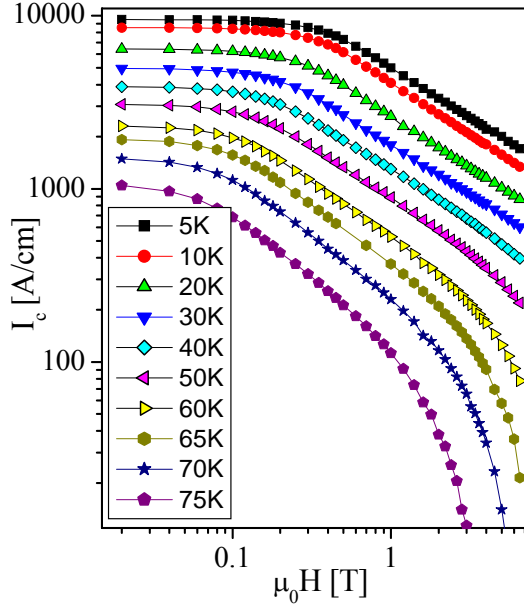


Fig. 45a. Magnetization critical current as a function of magnetic field parallel to c at the temperatures indicated.

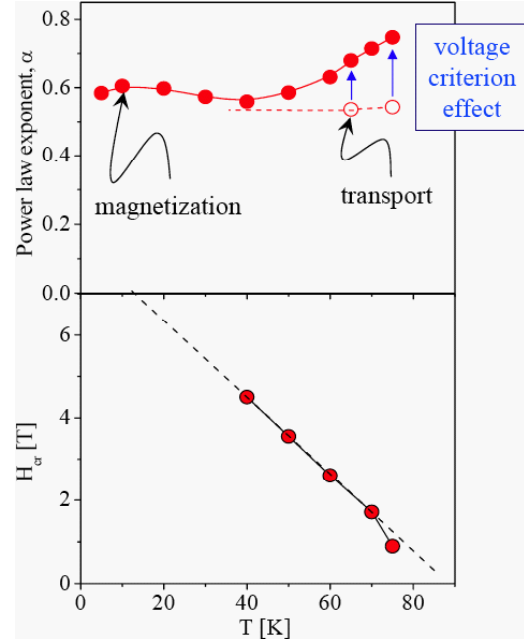


Fig. 45b. Temperature dependence of the power law exponent α and the critical field H_{cr} derived from the data shown in Fig. 31a.

Expanding our measurements to multilayer films of undoped YBCO, we have determined that α is almost temperature independent (Fig. 46a) in all these configurations. The differences at high temperature are due to the voltage criterion effect. Comparing transport and magnetization results, we find very good agreement for the variations among the samples and good numerical agreement. We do see variations of α with temperature that are small but systematic. We find that the multilayers and the thick single layer YBCO films also exceed the DoD Title III target of 450 A/cm at 30 K and 3 T, as shown in Fig. 46b. The 6 layer film at 960 A/cm width achieves double this target.

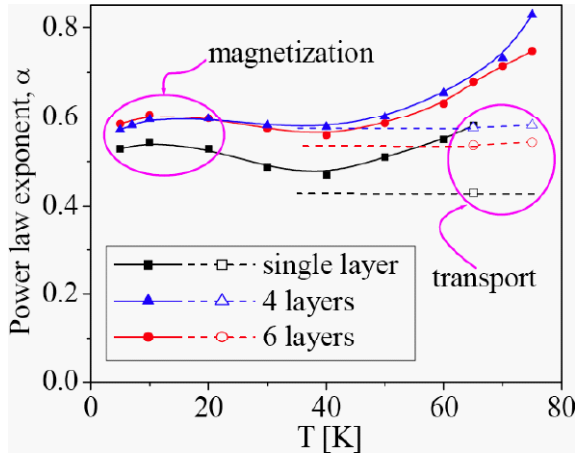


Fig. 46a. Power law exponent α as a function of temperature for single and multilayer undoped YBCO films.

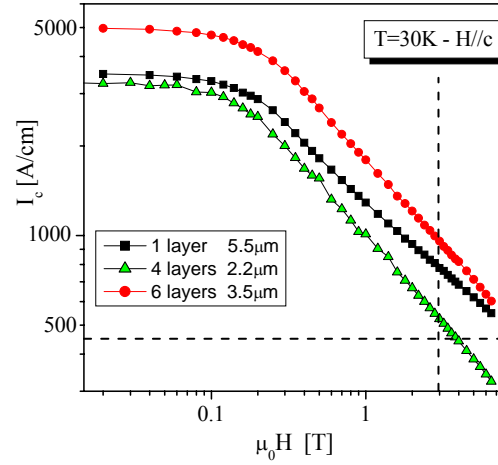


Fig. 46b. Critical current as a function of applied field parallel to c at 30 K for single and multilayer undoped YBCO films.

Summarizing the work reported here, we have validated the incremental j_c model we have proposed using ion milling and repeated measurements of the same sample progressively thinned. We have developed the use of some tools, such as PrBCO/YBCO bilayers, to further analyze the thickness dependence. We have determined the thickness dependence of J_c as a function of temperature and magnetic field amplitude and angle (T , H , and Θ). This has resulted in a significant narrowing of the possible explanations for the thickness dependence of J_c . We have found what we believe to be a "smoking gun" in the presence of misfit dislocations resulting from interfacial effects. We have determined that the defects responsible for the additional pinning in thin films are uncorrelated and scarce. We have demonstrated that multilayer films retain their strong I_c performance in an applied field. These multilayers (and thick single layer) undoped YBCO films surpass all DOD Title III I_c target values. With BaZrO₃ (nanoparticle) doped films, we have found record low values of field decay. Finally, we have introduced new tools, such as magnetization to determine J_c and high-field irreversibility line, for further exploration of vortex pinning.

Future work will be directed towards continuing to refine multilayers to exploit their very high J_c s for thinner YBCO with a goal to achieve 1000 A/cm-width in 2.5 μm . We also intend to extend the angular dependent measurements to non-maximum Lorentz force configurations, with a goal of understanding pinning and current distribution in realistic situations for applications. We will also continue to study pinning enhancement by nanoparticles, rare earth substitutions (variance), and YBCO/CeO₂ multilayers with the goal to achieve 1000 A/cm at 40 K and 3 T.

2.1.3 Microstructures and Vortex Pinning in MOD and PVD-BaF₂ ex-situ YBCO Films on RABiTSTTM

T.G. Holesinger, B. Maiorov, and L. Civale (LANL), Xiaoping Li, Yibing Huang, and Marty Rupich (AMSC), Dean Miller and Vic Maroni (ANL), and Ron Feenstra, (ORNL) [Wire Development Group]

We will first discuss baseline MOD and PVD-BaF₂ ex-situ YBCO films on RABiTSTTM in terms of their characteristic microstructures and baseline pinning microstructures. Then we will investigate microstructure modifications for changing and understanding the pinning characteristics in ex-situ YBCO films. We will look at alternative heat treatments to baseline samples, RE₂O₃ additions (RE= Ho, Er, Pr, Eu, Yb, Sm), and excess Y₂O₃ additions (PVD-BaF₂ by Ron Feenstra-ORNL). The tools that will be used are electron microscopy, Raman, XRD, self-field J_c(T), angular anisotropy measurements of J_c(H,T,Θ), comparisons to in-situ (pulsed laser deposition or PLD) YBCO films.

The same RABiTSTTM-based architecture (Fig. 47) is used for research and scale-up. The WDG research is directly tied to AMSC scale-up efforts. For instance, YBCO films 0.4 to 1.7 μm for the MOD-BaF₂ (Metal-Organic Deposition of precursors) has high J_c and is the process to be scaled commercially. On the other hand, 0.1 to 3 μm thick films for PVD-BaF₂ (Physical Vapor Deposition of precursors) also have high J_c and a conversion process similar to that for MOD, yet PVD is a much more flexible tool for investigating a wide range of films.

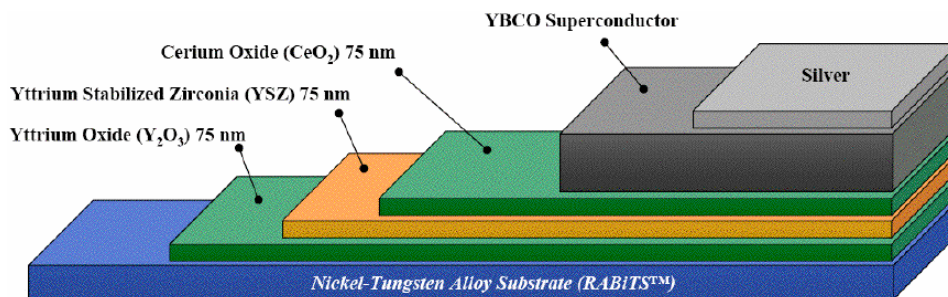


Fig. 47. Architecture of MOD-BaF₂- and PVD-BaF₂/ RABiTSTTM-based tapes.

The MOD YBCO films produced at AMSC are macroscopically uniform. SEM analysis shows few surface defects. There is also essentially no difference in the Raman spectra with regards to individual spectra averaged over many spots.

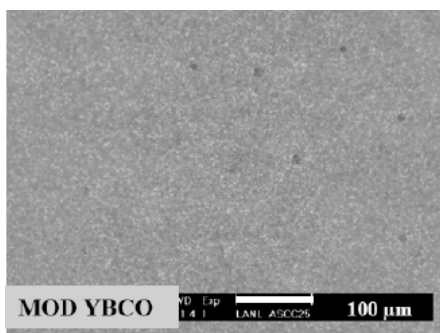


Fig. 48a. SEM of MOD YBCO surface.

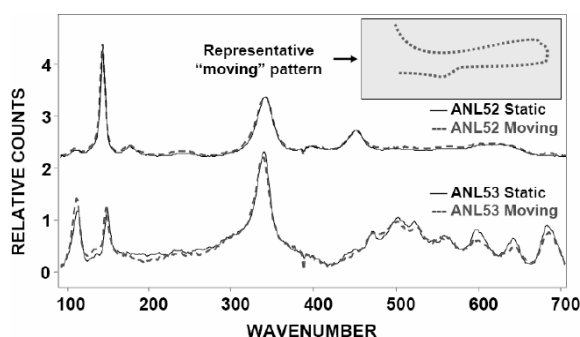


Fig. 48b. Raman of two REBCO films as a function of wave number.
ANL52 has RE=100% Er, I_c=120 A/cm-w; ANL53 has RE=50% Y & 50% Er, I_c=150 A/cm-w. (V. Maroni, ANL.)

At the microscopic level, ex-situ (MOD, PVD) and in-situ (PLD) YBCO films have characteristically different microstructures (Fig. 49). Characteristic features of ex-situ YBCO films (MOD and PVD) include a layered microstructure, mostly non-coherent inclusions, porosity, and grain boundary meandering and overgrowth. In contrast, the PLD films show a dense, columnar structure.

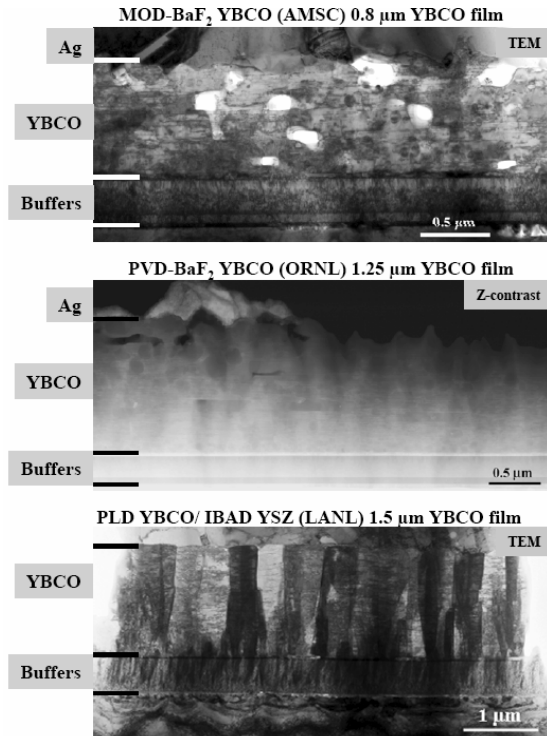


Fig. 49. Characteristic features of YBCO films produced by different processes.

The MOD-BaF₂ film has a J_c of 3.6 MA/cm² for 1.0 μm thick. The PVD- MOD-BaF₂ films have J_c s of 2.8 and 2.3 MA/cm² at 1.1 and 1.7 μm thick, respectively. The PLD/IBAD film has a J_c of 4.1 MA/cm² for 1.2 μm thick.

Stoichiometric in-situ PLD YBCO films have a columnar structure with coherent precipitates and a low density of planar defects, as shown in Fig. 50.

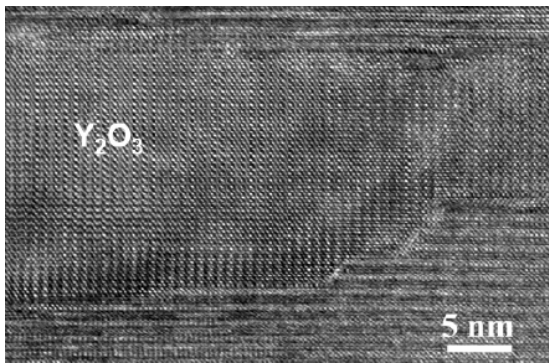


Fig. 50a. Coherent Y₂O₃ precipitate in PLD YBCO.

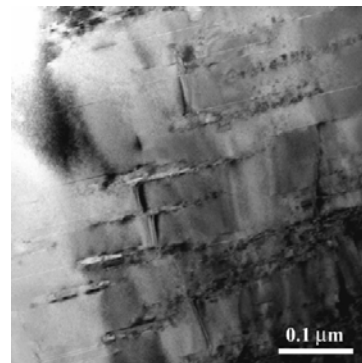


Fig. 50b. LANL 1.5 μm PLD YBCO film on IBAD MgO. The c-axis aligned defects, such as grain boundaries, dislocations, and anti-phase boundaries, are the source of correlated $J_c(H||c)$ pinning.

The J_c angular anisotropy measurements on baseline ex-situ and in-situ films show distinct differences, as shown in Fig. 51. (Leonardo Civalé–Peer Review 2004). In MOD films there is no clear separation between random and ab-plane correlated pinning regimes (Fig. 52a), but can easily be seen for PLD films (Fig. 52b).

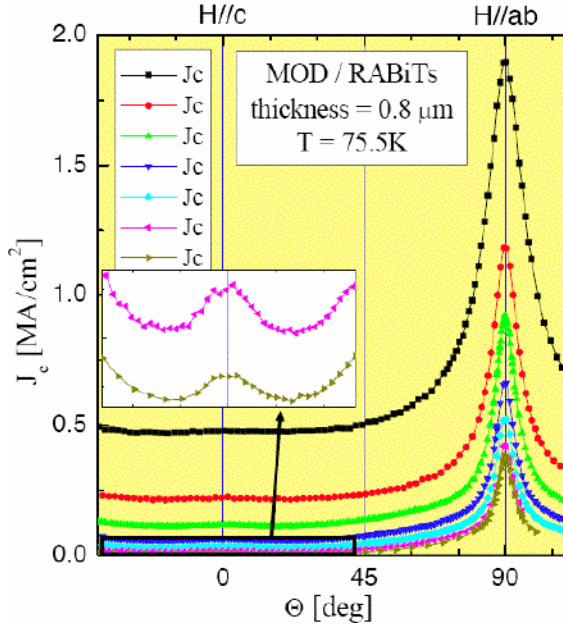


Fig. 51a. MOD films show a very small c-axis peak and a large ab-plane peak.

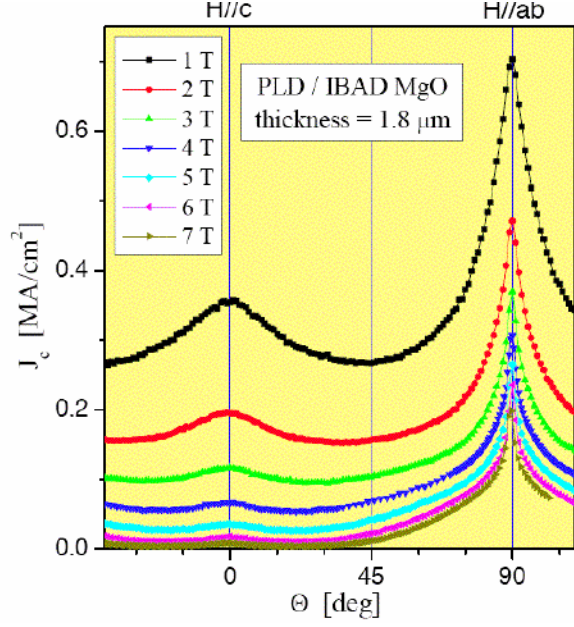


Fig. 51b. PLD films show a large c-axis peak and a small ab-plane peak.

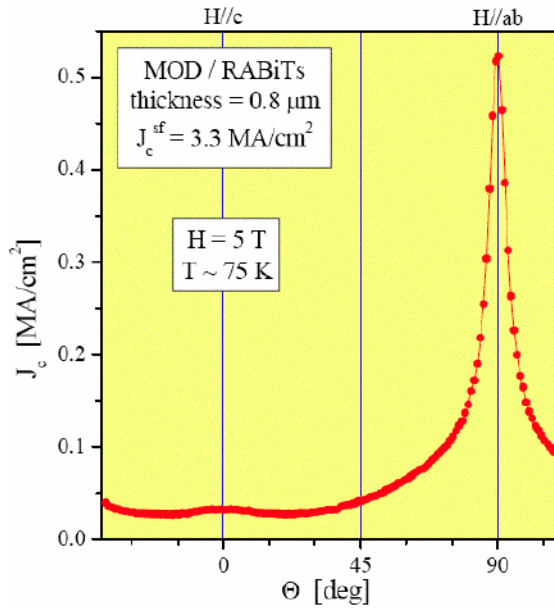


Fig. 52a. MOD films are strongly dominated by ab-plane correlated pinning.

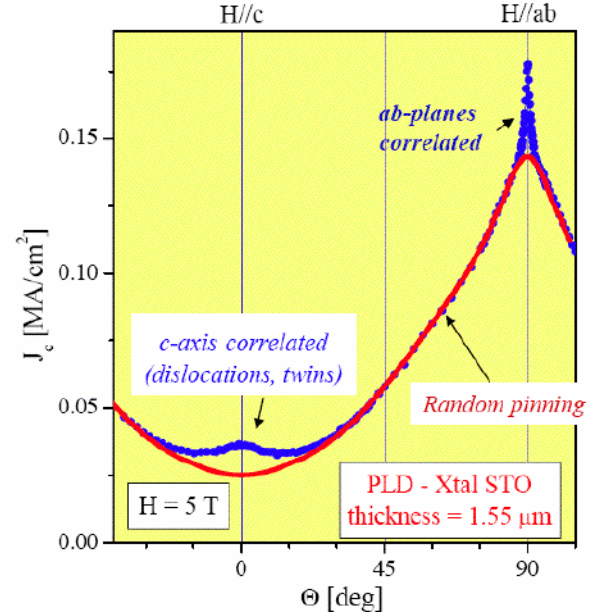


Fig. 52b. PLD films have clearly separated random pinning, c-axis-, and ab-plane correlated pinning regions.

Baseline AMSC MOD ex-situ YBCO films are characterized by defects of various types and length scales. We hypothesize that the Y-124 intergrowths (Fig. 53a) are responsible for the improved (correlated) pinning for $J_c(H||ab)$. The low density of non-coherent inclusions with strain fields, as seen in Fig. 53b, may lead to correlated defects and $J_c(H||c)$. At larger length scales, such features as variable porosity, film tilting, and colony structures are seen (Fig. 54).

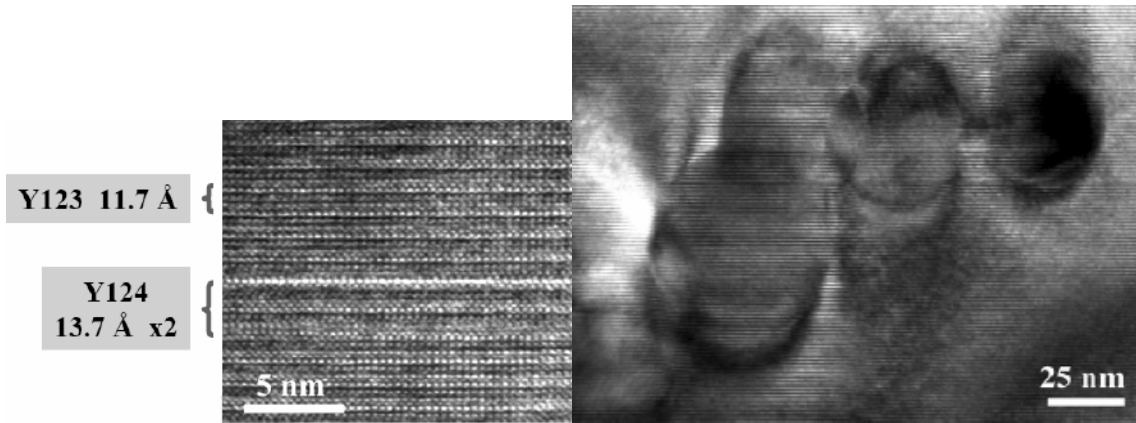


Fig. 53a. HRTEM of MOD film showing intergrowths.

Fig. 53b. TEM image of MOD film showing non-coherent inclusion



Fig. 54. TEM image of MOD film showing porosity and other features.

At the microscopic level, there are point-to-point variations in the microstructure of the ex-situ (both PVD and MOD) YBCO films. These manifest themselves as structural variations, such as porosity, planar defects, sub-grain structure, and film tilt. There are also chemistry variations, including second phase distributions and phase segregation. Some of these features are shown in Fig. 55.

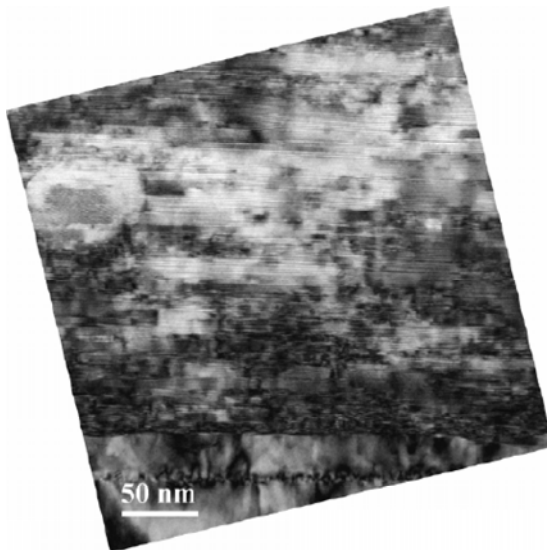


Fig. 55a. TEM of 0.7 μm PVD-BaF₂ film on AMSC RABiTS film showing variations in microstructure and chemistry.



Fig. 55b. TEM of 0.7 μm PVD-BaF₂ film on AMSC RABiTS film showing variations in microstructure and chemistry.

Microstructural variants (Fig. 56) in the MOD and PVD-BaF₂ YBCO films can occur due to changes in the amount of liquid phase during conversion. The understanding of several ex-situ microstructure variants in YBCO films was the result of research on PVD-BaF₂ films.

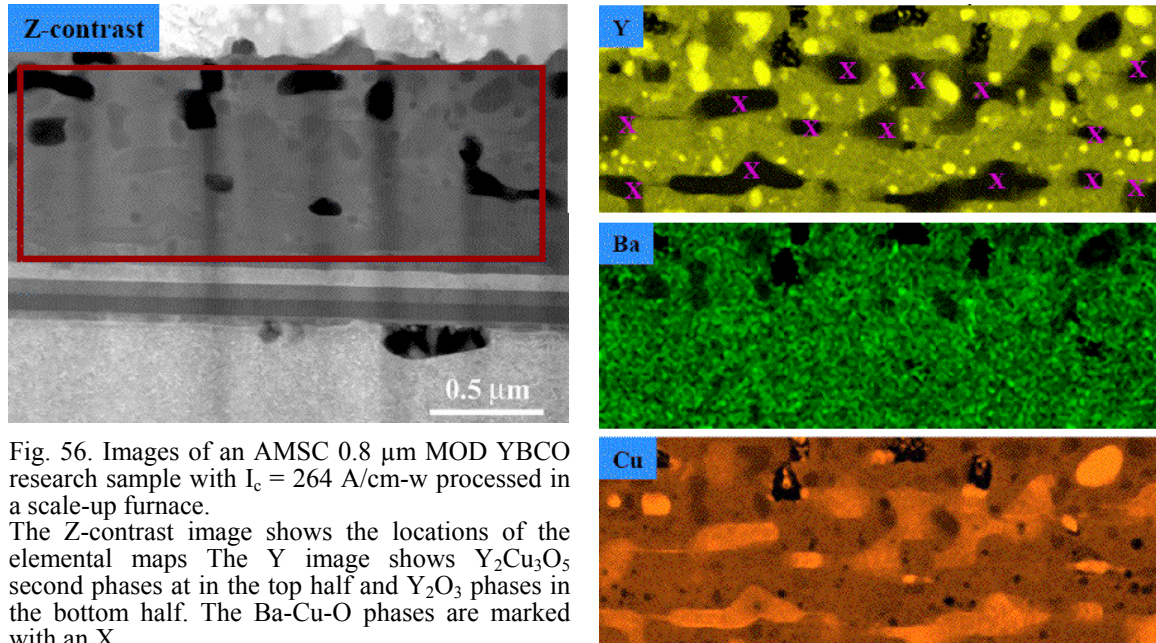


Fig. 56. Images of an AMSC 0.8 μm MOD YBCO research sample with $I_c = 264 \text{ A/cm-w}$ processed in a scale-up furnace. The Z-contrast image shows the locations of the elemental maps. The Y image shows $\text{Y}_2\text{Cu}_3\text{O}_5$ second phases at in the top half and Y_2O_3 phases in the bottom half. The Ba-Cu-O phases are marked with an X.

Long-length AMSC coated conductors have been successfully produced with the same basic high- J_c ex-situ YBCO structure as found in WDG research samples (Fig. 57).

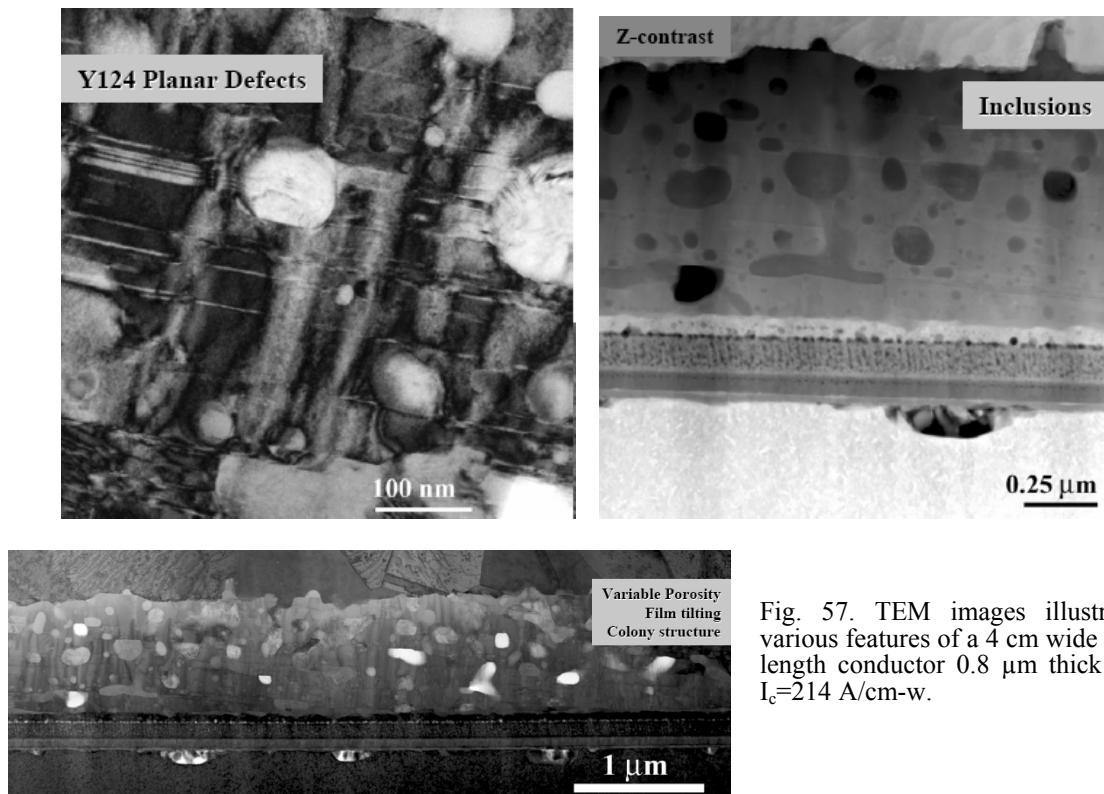


Fig. 57. TEM images illustrating various features of a 4 cm wide long-length conductor 0.8 μm thick with $I_c=214 \text{ A/cm-w}$.

Vortex pinning in baseline MOD ex-situ YBCO films can be changed by modifying the heat treatment schedule as shown in Fig. 58. As a result of the addition of the HTOA small changes in T_c and twin spacing take place but no texture changes in the YBCO film. The properties of these films were then investigated by various techniques.

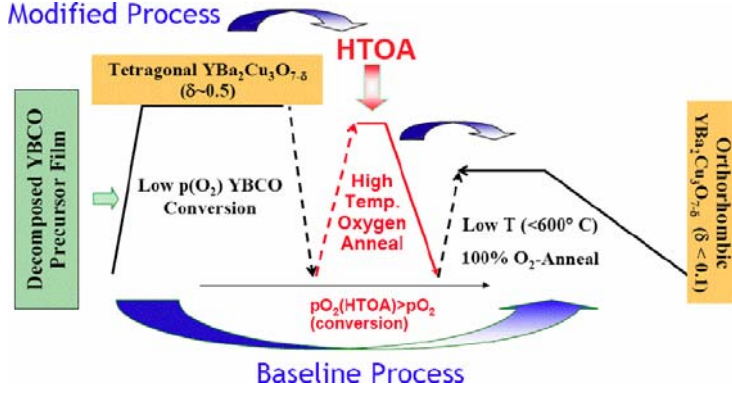


Fig. 58. Schematic of the baseline process for heat treatment of an MOD film and a modified process with a high-temperature oxygen anneal (HTOA) added.

The HTOA generates a c-axis peak that resembles that of the PLD films as shown in Fig. 59. It also reduces the anisotropy significantly by reducing the magnitude of the ab-plane peak. X-ray diffraction analysis suggests that the Y124 intergrowth density (side features on (00l) lines) is reduced with the HTOA. The T_c changes from 91.5 to 88 K and the twin spacing changes from 54.2 nm to 77.3 nm with the HTOA.

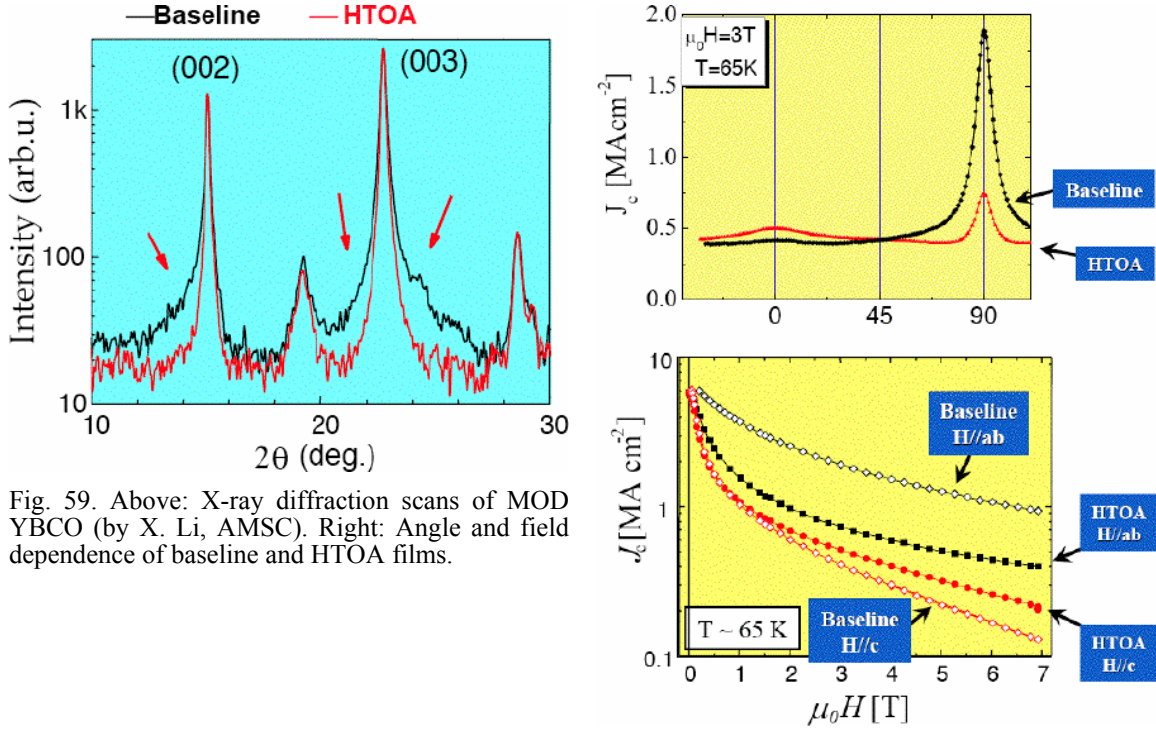


Fig. 59. Above: X-ray diffraction scans of MOD YBCO (by X. Li, AMSC). Right: Angle and field dependence of baseline and HTOA films.

The decrease in the angular I_c anisotropy also correlates to TEM observations of a reduction in the density of Y124 planar intergrowths (Fig. 60). The Y124 planar defects that end within a YBCO grain give rise to stacking faults, anti-phase boundaries, and localized strain that tend to align in the c-axis direction. The change in microstructure and pinning characteristics with the HTOA provides additional evidence for the Y-124 ab-plane correlated pinning effect.

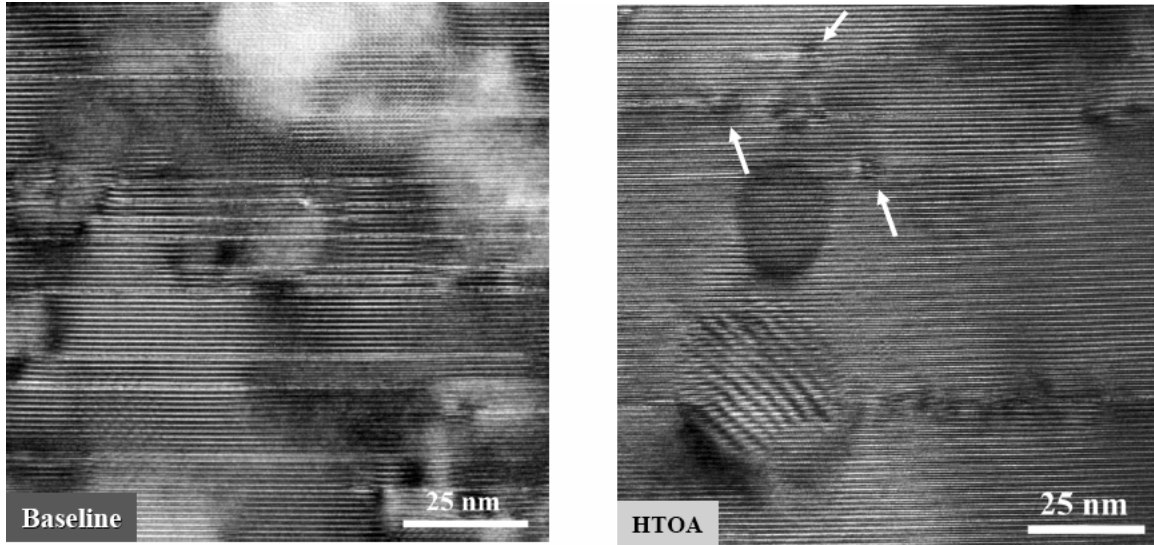


Fig. 60 TEM images of baseline and HTOA MOD films. The c axis is vertical, and the a and b axes are horizontal in these images.

A wide variety of rare earth substitutions ($Y_{1-x}RE_x$) and additions (Y_1RE_x) in MOD ex-situ films have been studied at AMSC for possible pinning enhancements. In contrast to earlier PLD results (Fig. 61a), minimal $J_c(H//c)$ increase is seen by rare earth substitution in MOD, but a significant increase of in-field $J_c(H//c)$ is observed by additions (Fig. 61b).

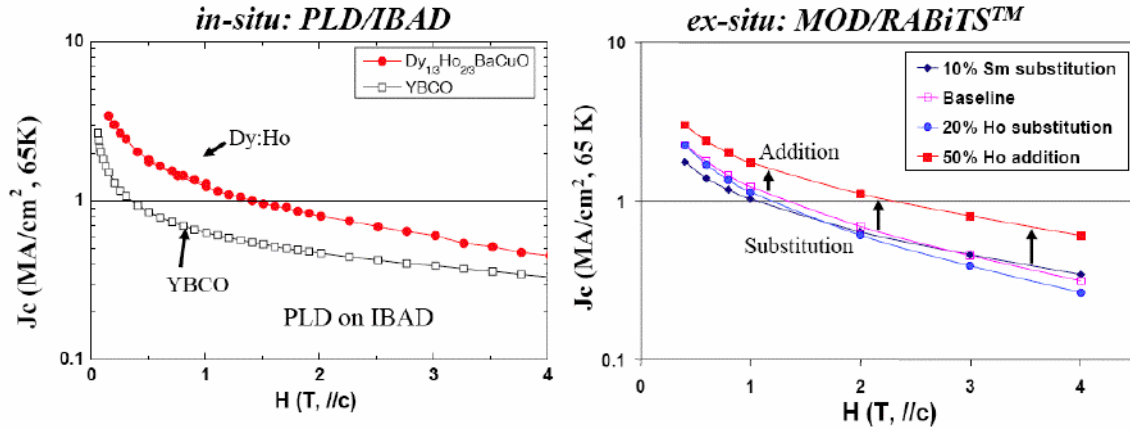


Fig. 61a. Enhanced pinning with Dy substitution in PLD YBCO films.

Fig. 61b. Enhanced pinning in MOD films with Ho addition, but little enhancement with substitution.

Substantial improvements for $J_c(H//c)$ were found for Er_2O_3 additions up to the level of 50% ($Y_1Er_{0.5}Ba_2Cu_3O_y$). There is little effect on the $J_c(\text{self-field})$, and the overall increase in $J_c(H//c)$ is at the expense of $J_c(H//ab)$ (Fig. 62a and b).

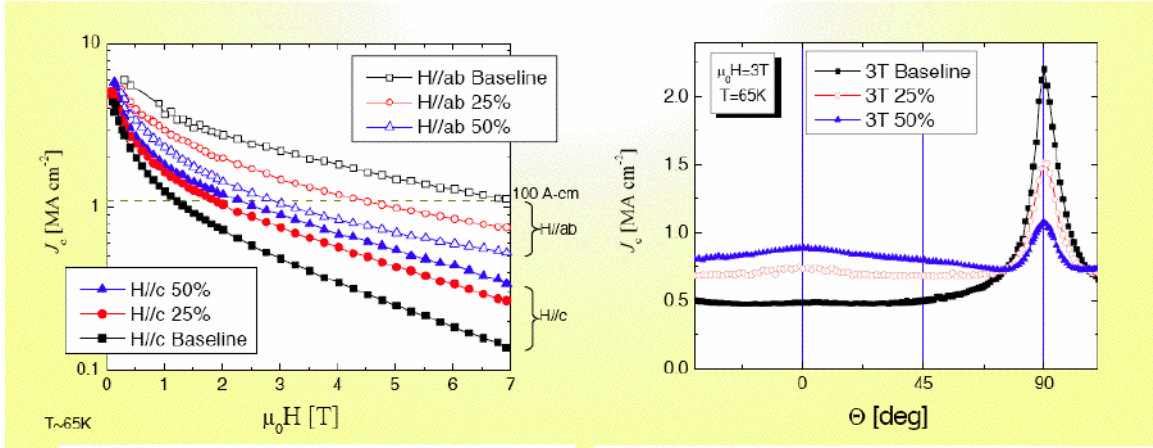


Fig. 62a. Critical current density as a function of magnetic field for Er additions in MOD films. The same trends are observed at 65 K and 75 K.

Fig. 62b. Critical current density as a function of angle for Er additions in MOD films. The I_c (75K, sf) are baseline 250 A/cm and 25% and 50% Er additions 260 A/cm.

The Er_2O_3 additions have been found to produce increasing numbers of $(Y,Er)_2O_3$ and $(Y,Er)_2Cu_2O_5$ inclusions in AMSC ex-situ MOD films as can be seen from Fig. 63. A limit to the Er additions is reached when grain boundary segregation of the rare earths significantly reduces J_c . This is seen clearly in the progression of additions from 25% to 1000% shown in Fig. 64 and in the elemental maps for the 100% Er additions sample in Fig. 65.

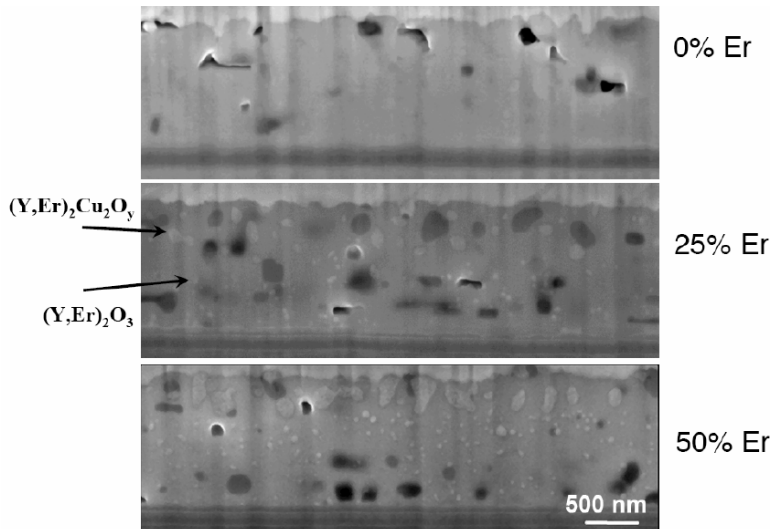


Fig. 63. Micrographs of ex-situ MOD films with varying amounts of Er additions (FIB by Dean Miller, ANL)

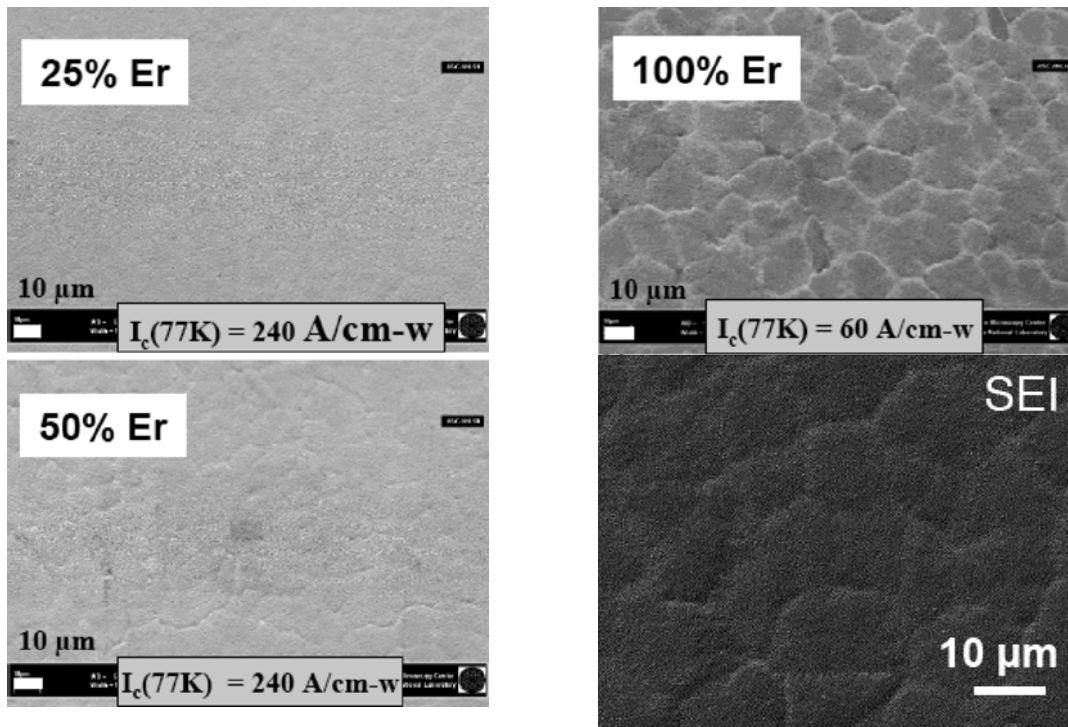


Fig. 64. Micrographs of the surface of ex-situ MOD films with varying amounts of Er additions. The vertical size of the image is 120 μm . The upper right image is a SEI image of the 100% Er sample that was subjected to elemental analysis with results shown in Fig. 65.

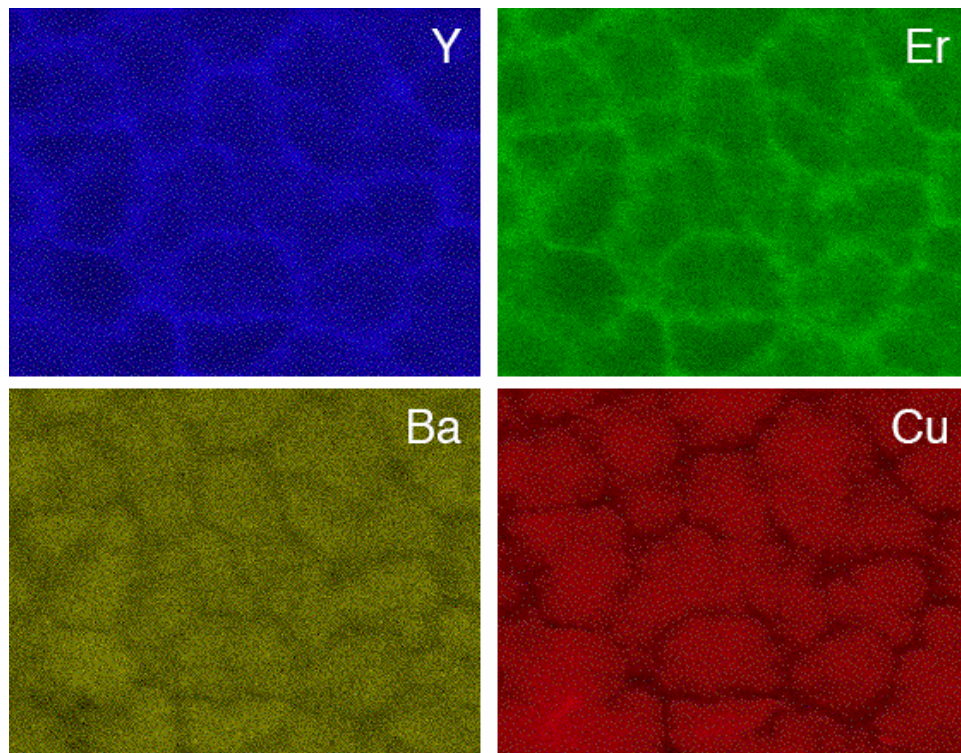


Fig. 65. Elemental maps of the ex-situ MOD film with 100% Er additions shown in Fig. 64.

The RE_2O_3 additions increase the density of the inclusions while significantly reducing the density of the ab-planar intergrowths as can clearly be seen in Fig. 66. The Y-124 intergrowth spacing increases from 16 nm to 111 nm for 0 and 50% Er additions, respectively. In addition the (00 l) peak broadening is reduced with increasing Er_2O_3 additions (Fig. 67). Both these pieces of data provide additional support for the hypothesis that $H\parallel ab$ correlated pinning is due to ab (Y-124) intergrowths

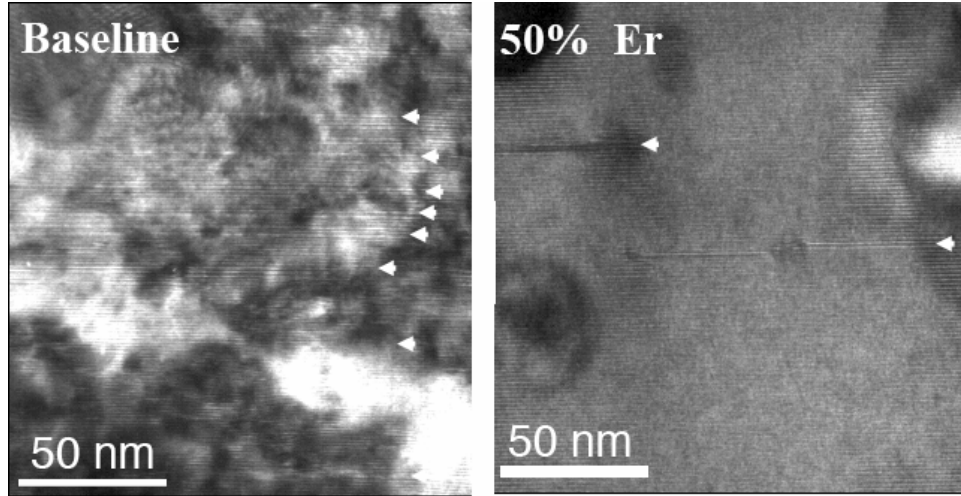


Fig. 66. TEM micrographs of Y-124 inclusions in baseline (spacing 16 nm) and 50% Er added spacing (111 nm) ex-situ MOD films. (Dean Miller, ANL)

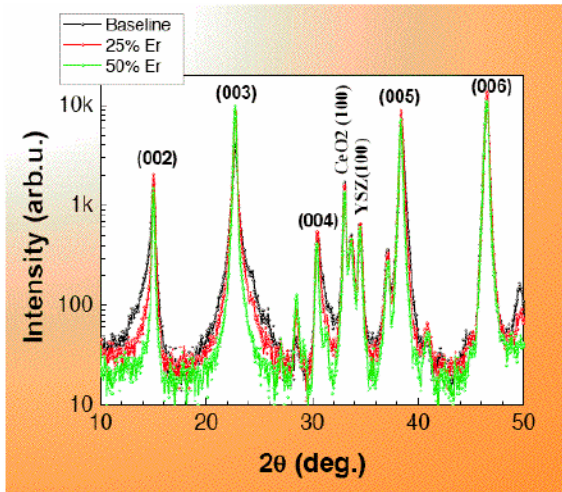


Fig. 67. XRD patterns of ex-situ MOD films at baseline and with Er additions and showing reduced peak broadening. (X. Li et al., AMSC)

The extended defect structure around the inclusions defines a pinning structure that is much larger than the precipitate itself. The extended nanodot structures act like splayed defects, as shown in Fig. 68 rather than c-axis aligned line defects in stoichiometric PLD YBCO films.

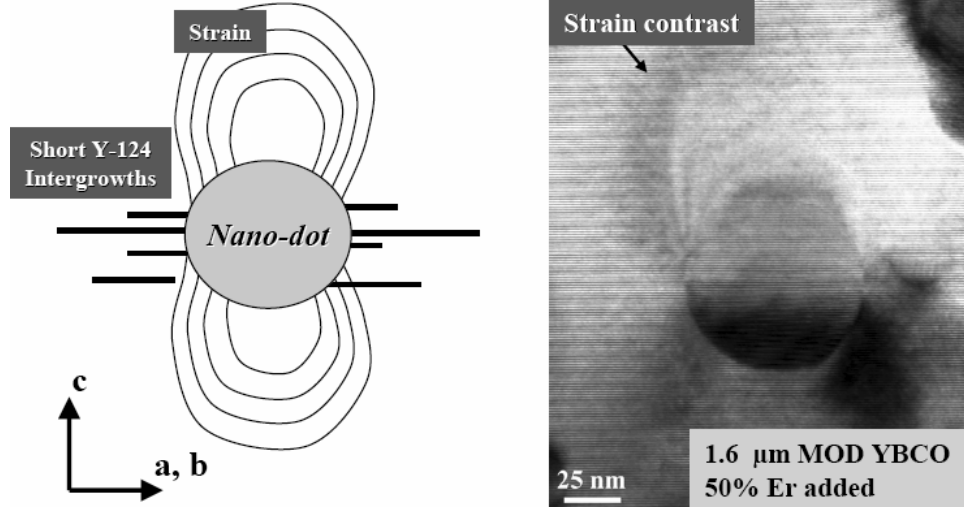


Fig. 68. Schematic (right) and TEM micrograph (left) of nanodot and surrounding strain fields.

Measurements for $J_c(H, \Theta, T)$ for the 50% Er MOD YBCO film show a much broader peak centered around $H \parallel c$ compared to that seen in standard PLD YBCO films (Fig. 69). Considering then all available data, we can correlate specific microstructures with specific characteristics of $J_c(H, \Theta, T)$. For instance, baseline films with a large ab-plane peak in J_c have many Y-124 intergrowths (Fig. 70a), and films with 50% Er additions that show a reduced ab-plane peak and the presence of a c-axis peak have nanodots and extended structures (Fig. 70b).

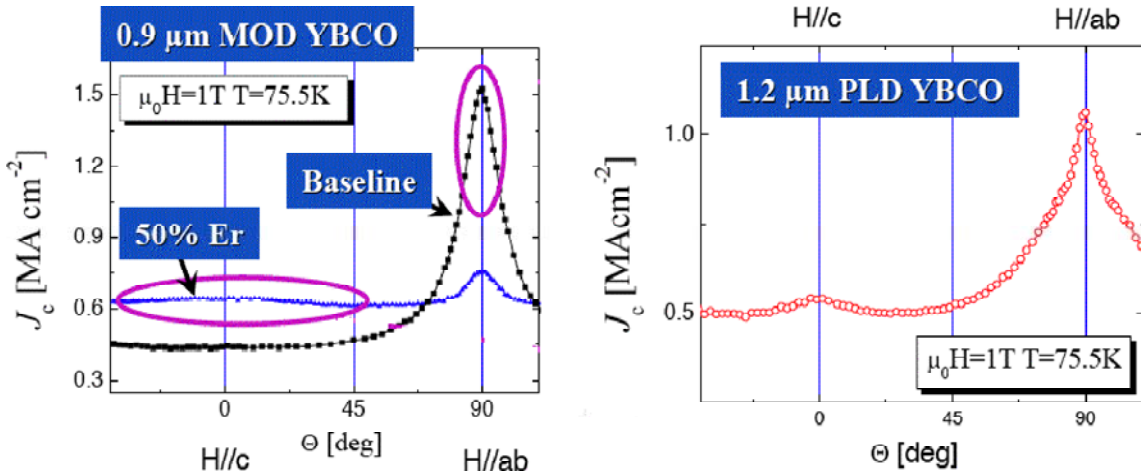


Fig. 69. Critical current density as a function of angle for MOD YBCO films (left), baseline and 50% Er additions and a PLD YBCO film.

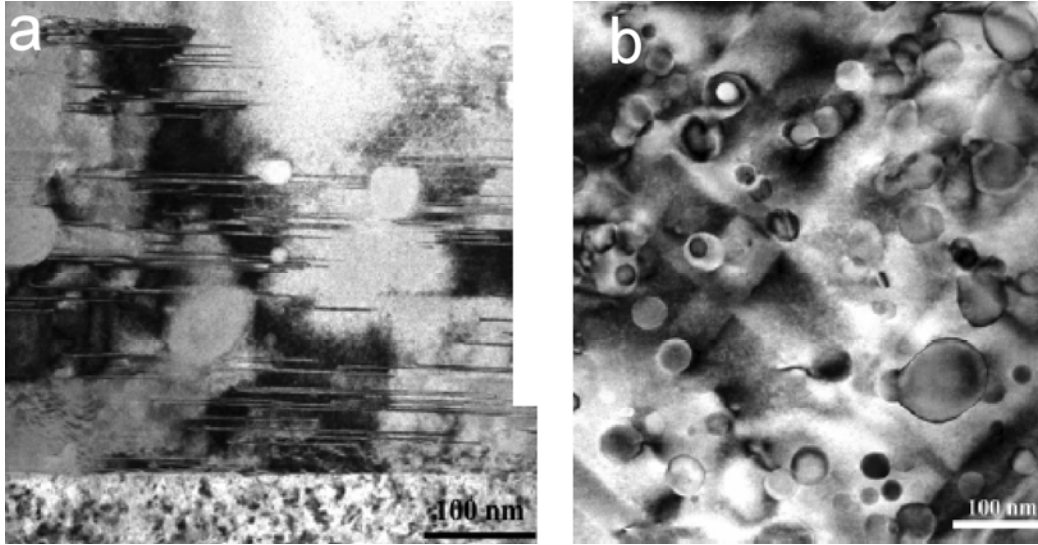


Fig. 70. a) Y124 intergrowths, found in baseline MOD films. b) nanodots plus extended structure found in 50% Er added MOD films.

To summarize, microstructure and electrical characterizations were used to highlight the differences in the structure-property relationships of *ex-situ* (lamellar structure) and *in-situ* (columnar structure) YBCO films. Characterizations of the baseline, RE_2O_3 additions, and HTOA (high temperature oxygen anneal) AMSC MOD YBCO films suggest that the Y124 intergrowths are the dominant ab-plane correlated pinning defect in baseline *ex-situ* films. For improved $J_c(H||c)$ pinning, *ex-situ* and *in-situ* YBCO films differ significantly in their underlying pinning mechanisms. We conclude that nanodots produced through RE_2O_3 additions are best for *ex-situ* $J_c(H||c)$ pinning. Finally, this understanding of the thin film processes of *ex-situ* MOD YBCO films in the WDG has helped AMSC accelerate its scale-up efforts.

2.1.4 Next Steps Towards a Commercializable Coated Conductor

V. Matias, B.J. Gibbons, S.P. Ashworth, P.C. Dowden, J.Y. Coulter, E. J. Rowley, A.T. Findikoglu, F. Grilli, L. Civale, and B. Maiorov

We have set up reel-to-reel fabrication and characterization capabilities set up for research at LANL. These include systems for electropolishing the substrates, deposition of the ion beam assisted deposition (IBAD) template layer, deposition of buffer layers and the HTS layer by pulsed laser deposition (PLD), and systems for characterizing the electromagnetic properties of the tapes.

A schematic of the LANL IBAD Reel-to-Reel system is shown in Fig. 71. The system was designed to be flexible for the R&D of various deposition sequences and sources. It has two electron beam sources, an assist ion source, two RHEED systems, a time of flight ion scattering instrument, and a sputter deposition zone. This latter is used for sputtering of Ta_2O_5 and TiN .

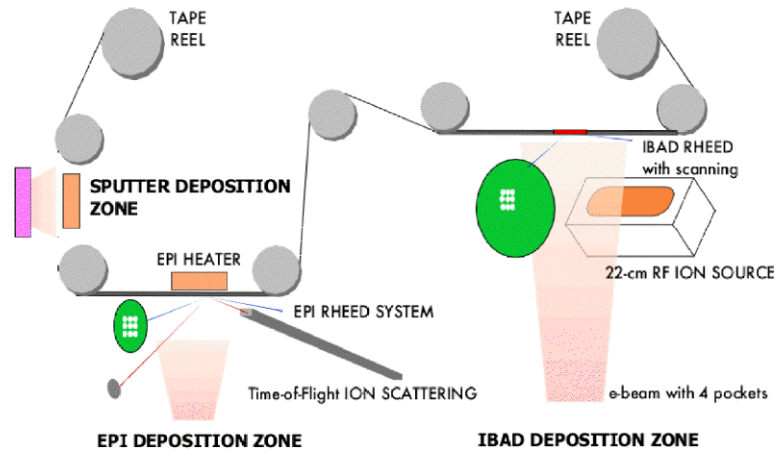


Fig. 71. Schematic of the IBAD system.

The original stacking sequence of layers of the IBAD-MgO architecture is shown in Fig. 72. We wanted to make the IBAD layer stack more robust to withstand higher temperatures and times. This could be achieved by increasing the thickness for the Al_2O_3 layer or the MgO layer. We decided to make a thicker MgO layer and remove the Al_2O_3 layer. This results in a simpler architecture with the bonus of better texture and less Al interdiffusion. RHEED patterns during the deposition are shown in Fig. 73. The Y_2O_3 layer can be deposited in a few seconds, the thick epi-MgO layer of 400 nm at up to 4 nm/s.

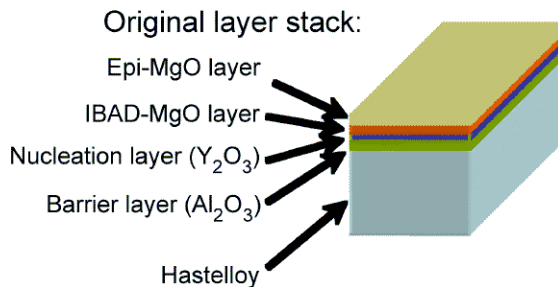


Fig. 72. Original stacking sequence through the epi-MgO layer.

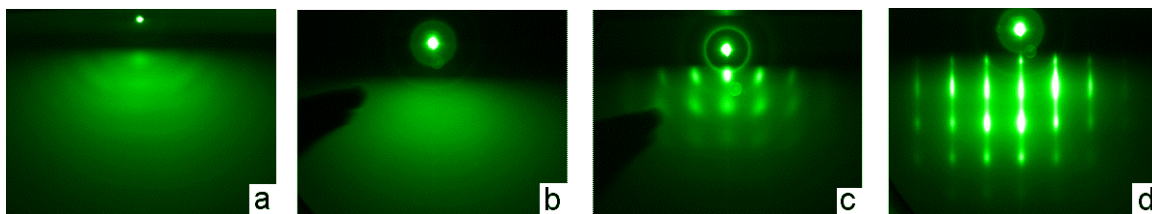


Fig. 73. RHEED patterns during deposition.

a: Hastelloy substrate; b: Y_2O_3 nucleation layer (6 nm); c: IBAD MgO layer (5-10 nm); and d: epi-MgO layer (400 nm).

The resulting IBAD-MgO tape showed good uniformity with improved texture. Fig. 74 shows the texture across the width and along the length of a 10 m tape. Typical in-plane texture for this length is $4 - 6^\circ$.

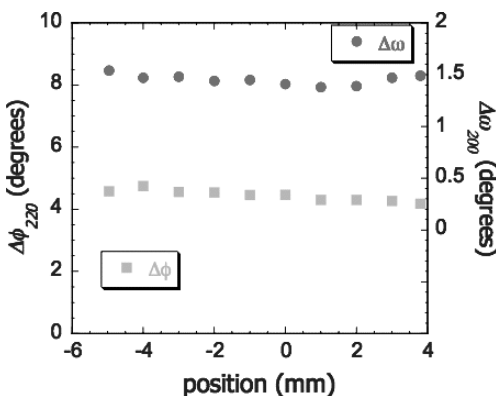


Fig. 74a. Texture across the width of a tape.

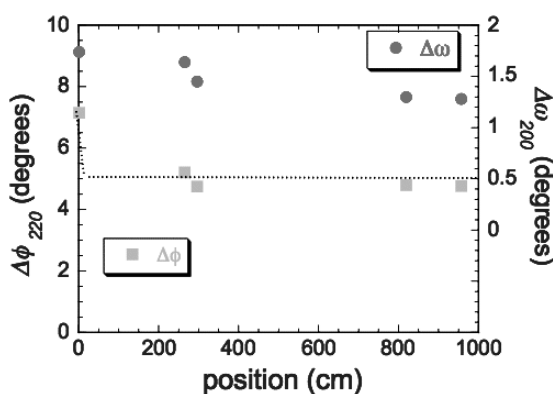


Fig. 74b. Texture along a 10 m length of tape.

Tilt of the MgO lattice is known to occur during IBAD in the plane of the ion direction, i.e., the plane perpendicular to the tape direction (Fig. 75a). We typically observe a tilt in our films of $2-4^\circ$. Tilting of the IBAD MgO lattice determines the vicinal angle (Fig. 75b); this tilt is then transferred to subsequent layers. Understanding of the tilt is poor, but it is known that IBAD atom/ion ration and thickness affect tilt.

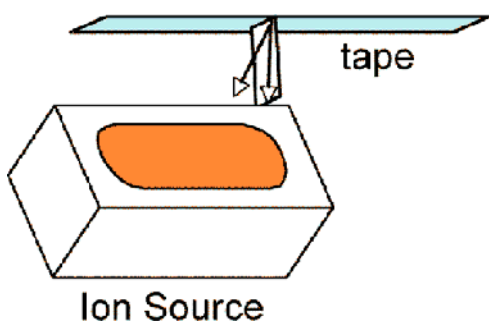


Fig. 75a. Schematic of the assist ion source geometry.

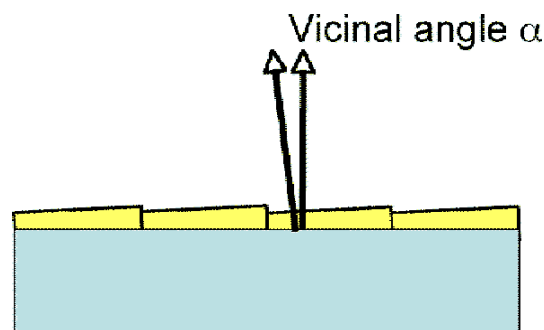


Fig. 75b. Tilting of the MgO c axis results in a stair step template and a vicinal angle α .

We have determined that it is possible to engineer the tilt in the IBAD MgO film. This can be done by pretreatment of the nucleation layer – changing the thickness of the nucleation layer and by ion beam treatment. This has been implemented with a moving tape by adding an adjustable shield (Fig. 76) to screen the MgO deposition at the start of IBAD. Fig. 77 shows the various tilts that have been achieved. To date, we have not observed a significant effect on J_c in the tape direction.

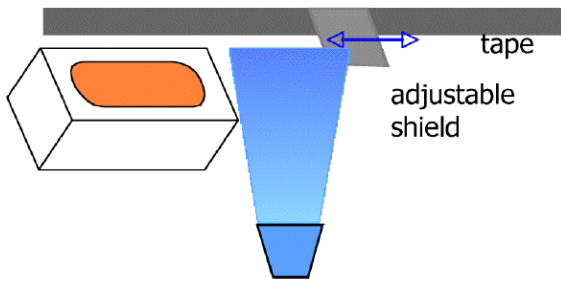


Fig. 76. IBAF deposition geometry with an adjustable shield to allow for nucleation layer pretreatment.

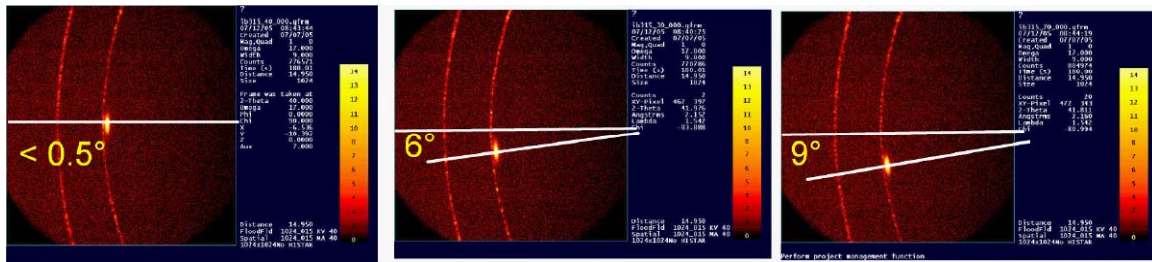


Fig. 77. Tilt of the MgO axis can be controlled by pretreatment of the nucleation layer.

We recently began experiments with a new sol-gel process for tape preparation. We have been investigating whether planarization by sol-gel deposition on unpolished Hastelloy substrate could avoid the need for electropolishing. Paul Clem, Sandia National Laboratory, used solution chemistry to deposit 150 nm films of amorphous Y_2O_3 on unpolished and polished Hastelloy substrates. We determined that the Y_2O_3 sol-gel layer could be used as a nucleation layer for IBAF MgO. AFM surface roughness measurements (Fig. 78) show that the surface finish can be improved to 6.2 nm with the sol-gel layer. Advantages of a sol-gel tape finishing process is that it is adaptable to any new metal substrate, and does not have to be tailored to a specific alloy. Multiple coatings can smooth out the rougher starting substrates. The process coats both sides of a tape to prevent oxidation of the back surface. The coating provides a barrier layer to interdiffusion and is ready as a nucleation layer for the IBAF MgO process. This research direction looks quite promising, but more work needs to be done to optimize the IBAF MgO and particularly the YBCO layer.

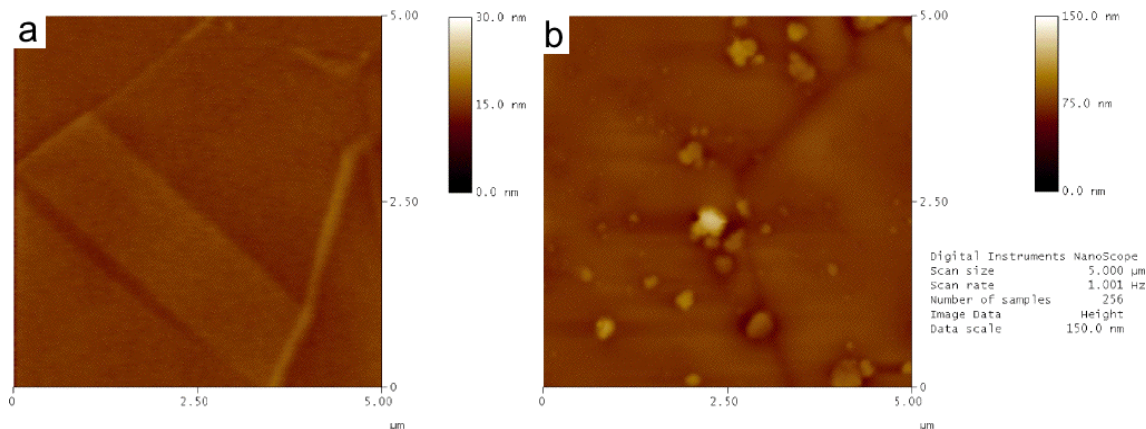


Fig. 78. AFM RMS roughness measurements for Y_2O_3 sol-gel coatings on Hastelloy substrates.

a) Polished Hastelloy 1.0 nm bare 0.6 nm with Y_2O_3 (IBAF MgO $\Delta\phi=4.8^\circ$, $\Delta\omega=1.3^\circ$) (YBCO $J_c > 1.5 \text{ MA/cm}^2$) b) Unpolished Hastelloy 13.2 nm bare 6.2 nm with Y_2O_3 (IBAF MgO $\Delta\phi=6.7^\circ$) (no YBCO results yet).

Previously, we showed that IBAD-MgO texture depends on the ion to molecule ratio *and* on the total deposit thickness as shown in Fig. 79a for IBAD MgO on metal tape with a Y_2O_3 nucleation layer. The best texture can be attained in a wide window for the ion-to-molecule ratio. Other surfaces were found to exhibit somewhat different behavior. Plotting the texture ($\Delta\phi$) as a function of ρ times the gross deposit thickness, i.e., by the total ion beam fluence, shows that the texture scales. The speed of texture evolution is determined by the ion beam fluence. Fig. 79b shows that the curves can be scaled with the amount of sputtered material.

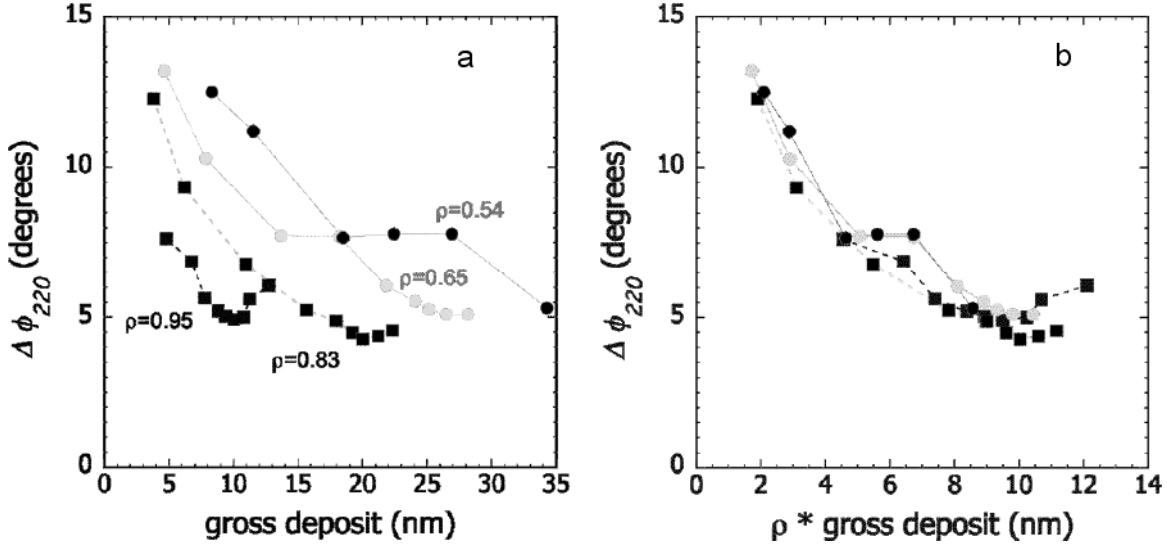


Fig. 79 a) in-plane texture as a function of gross deposit thickness for various ratios ρ of ion/molecule ratio. b) in-plane texture as a function of ρ times the gross deposit thickness.

In the past we have been able to produce IBAD MgO at a maximum rate or 100 m/hr with a $\Delta\phi$ FWHM of 10° . This year, by increasing the deposition zone to 14 cm and optimizing the ion fluence, we have reduced the IBAD time to 1.8 s (Fig. 80) for 7° in-plane texture and a speed of 270 m/hr. Note that more typical operation to achieve better texture is about $1/10^{\text{th}}$ this speed.

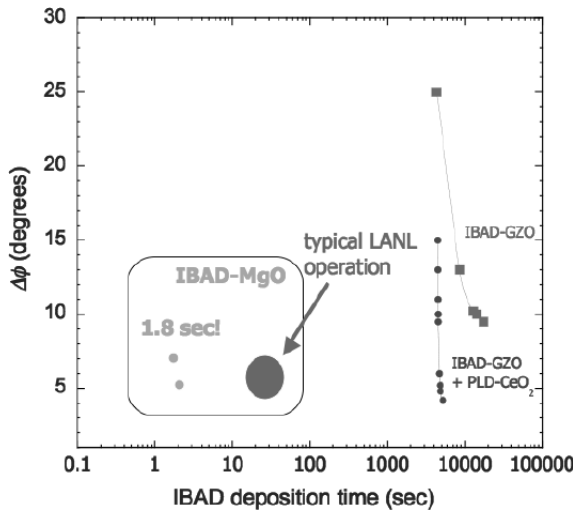


Fig. 80. Texture as measured by $\Delta\phi$ FWHM as a function of IBAD deposition time for IBAD MgO and other competing processes.

In our analysis of the speed of template production, we believe it is necessary to achieve speeds of 1 km/hr for cm-wide equivalent tape. Examining the various layers in the process yields the data shown in Table 2. In our process, the barrier layer has been removed. This leaves the Epi-MgO layer as the slowest of the entire process.

Table 2. Process speeds for IBAD deposition by step

| | Electro-polishing | Barrier layer (Al ₂ O ₃) | Nucleation layer (Y ₂ O ₃) | IBAD MgO | Epi- MgO |
|------------------------------------|-------------------|---|---|----------|----------|
| Demonstrated speed (LANL) cm-km/hr | 0.04 | 0.004 | 0.015 | 0.27 | .004 |
| Lab capable speed cm-km/hr | 0.2 | 0.02 | 0.2 | 1 | 0.015 |
| Industrial scale up to 1 cm-km/hr | OK | ? | OK | OK | ? |

This slowness prompted a study of other IBAD materials that might have similar texture evolution. We have studied NiO, CrO, CoO, and TiN, and all these materials seem to have a similar type (to that of MgO) of fast structure evolution. In addition, TiN is a conducting layer with a conductivity ρ of $\sim 25 \mu\Omega\text{-cm}$, which opens up the possibility of a conducting IBAD layer stack. The best result to date for IBAD TiN (Fig. 81) is 7° FWHM in-plane.

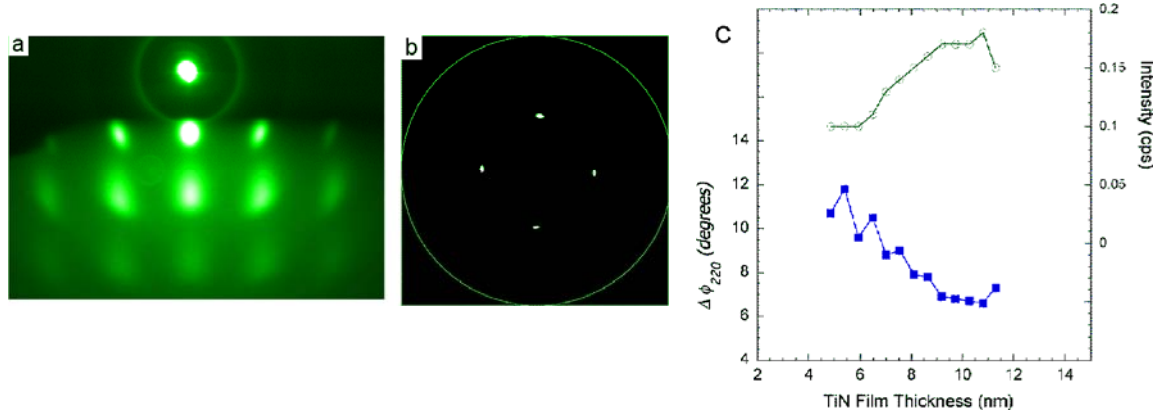


Fig. 81. IBAD TiN properties. a) RHEED pattern for TiN with ion beam at 750 eV and a 45° angle. b) 220 pole figure of IBAD TiN c) $\Delta\phi$ FWHM texture evolution and X-ray peak intensity as a function of film thickness.

We next discuss the subject of superconductor deposition. All of the systems at the Research Park are designed for flexible operation so that we may integrate new ideas (new materials, architectures, and geometries/conductor designs, etc.) into a reel-to-reel deposition environment. This kind of research is much easier in a non-manufacturing environment, and the results of these demonstrations can then be integrated into our industrial partners' processes. Progress in the past year has resulting in an increase from 172 A on 1 m (75 K, self field) to 350 A on 1.2 m and 530 A on a 7 cm short sample. Improvements in the IBAD architecture resulted in significant structural improvement such that the in-plane and out of plane structural parameters and now well below the limits that lead to deleterious intergranular current flow. The excellent texture achieved in a $2 \mu\text{m}$ YBCO film is shown in Fig. 82.

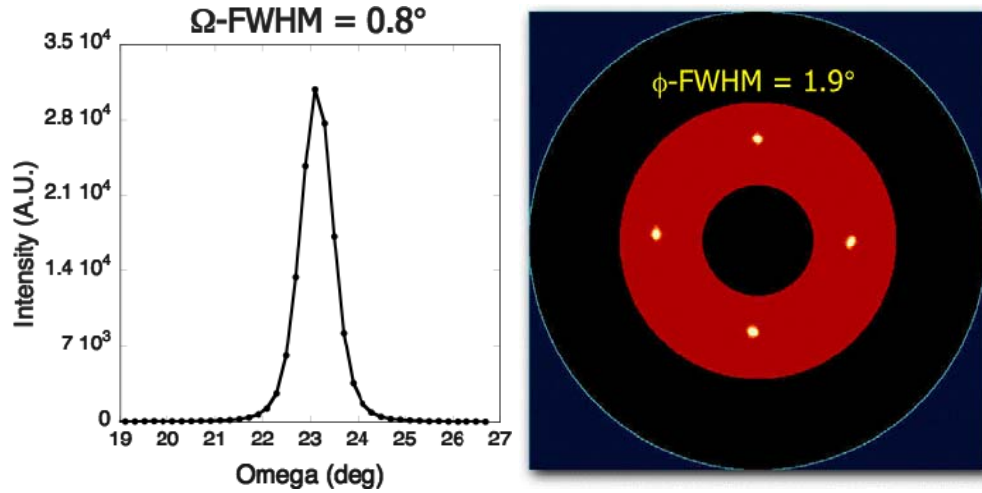


Fig. 82. Out-of-plane (left) and in-plane texture for a thick YBCO film.

These recent samples also yield good uniformity along the length. Fig. 83, left shows a tape with a standard deviation of $\pm 3.5\%$. The most important factor in achieving this goal is the elimination of current “drop outs,” or sections of near zero I_c . A histogram plot of the data of Fig. 83, left indicates an asymmetric distribution (Fig. 83, right) with the tail extending to higher currents than the mean.

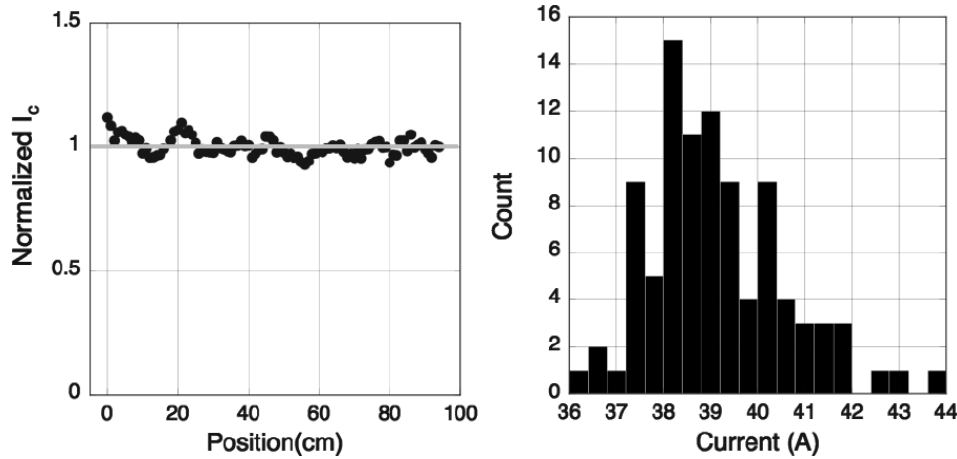


Fig. 83. Uniformity along the length of a coated conductor tape. Left, normalized I_c as a function of position. Right, histogram of the current.

However, the width uniformity can be improved: The J_c for the entire width is lower than expected. By scribing the tape into ten 1 mm wide strips (Fig. 84a) and measuring I_c , the non-uniformity across the tape can be seen in Fig. 84b. We speculate that the thermal environment at the edges of the tape is different during growth.

In the middle, however, our coated conductors show excellent properties as deduced from a magneto-optic imaging (MOI) study by M. Feldmann and N. Nelson, Univ. Wisconsin. Samples were laser scribed into the center portion of a coated conductor tape with a link size of 300 x 850 μm and thickness of 550 nm (Fig. 85). The measurements were made at 77 K. Fig. 86 shows the MOI patterns at different current densities. The flux penetration is extremely uniform.

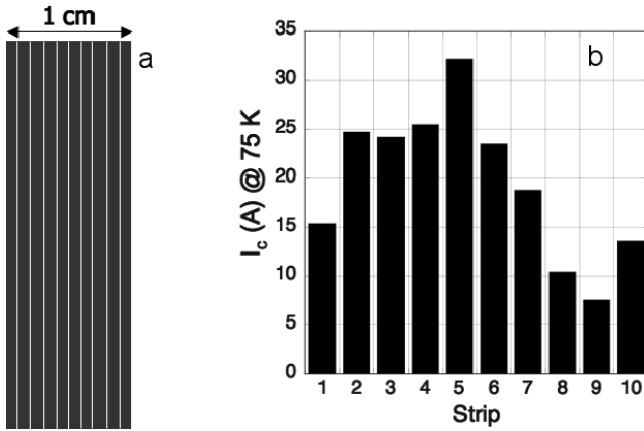


Fig. 84. a) Scribing of tape into 10 strips for b) I_c measurements.

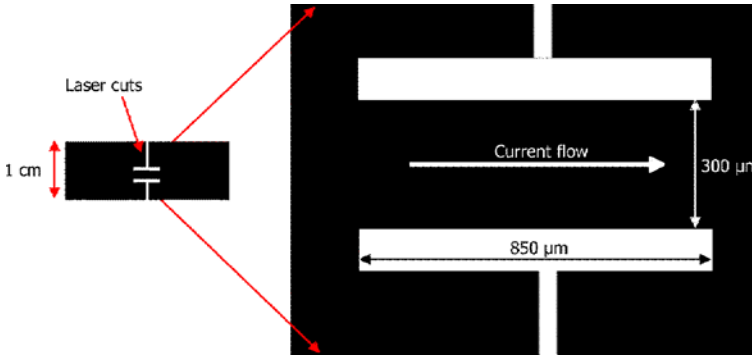


Fig. 85. Geometry of MOI samples cut from middle of centimeter wide tape.

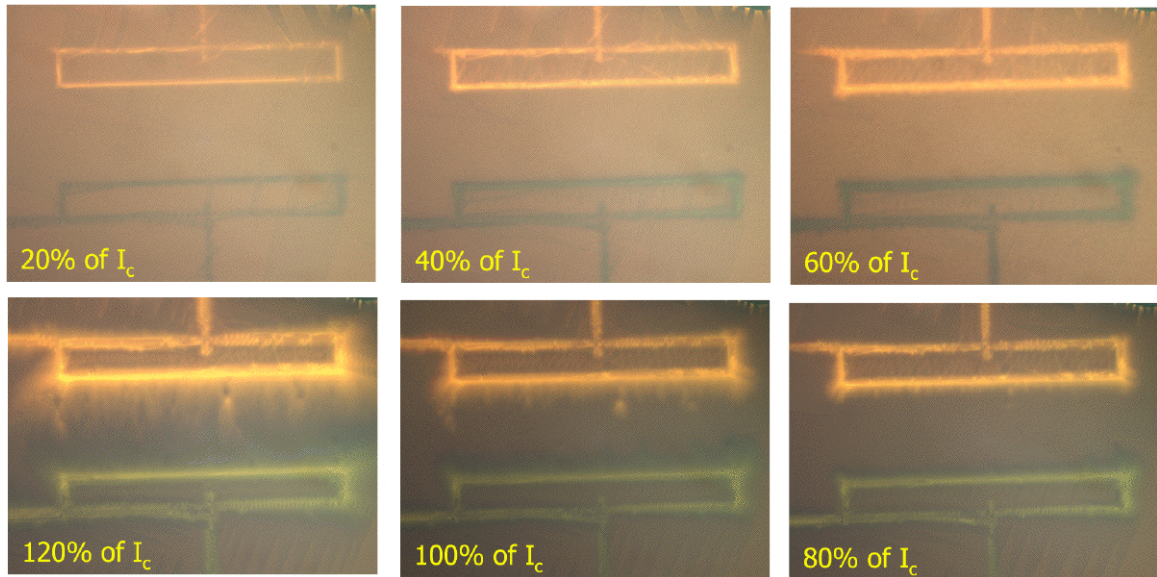


Fig. 86. MOI as function of current density for a coated conductor tape.

Electron back-scattered diffraction results also show very uniform structure. Both the EBS scans sensitive to out-of-plane alignment and in-plane alignment (Fig. 87) show extremely low grain misalignment. Grain boundary structure maps (Fig. 88) also show a very uniform structure.

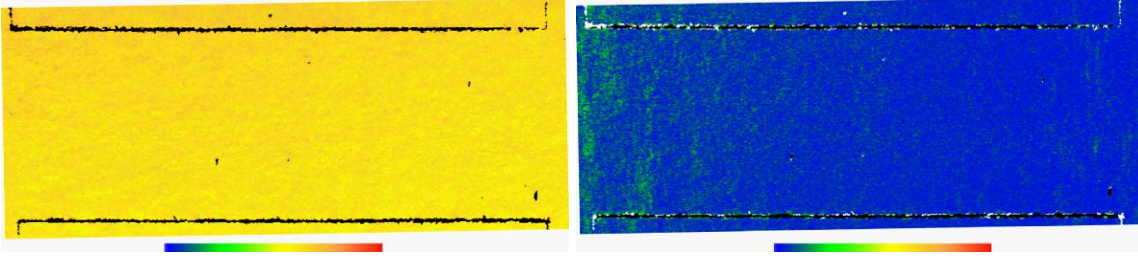


Fig. 87. Electron back-scattered diffraction (EBS) images of the (left) out-of-plane (angle between sample normal and nearest crystal axis) and of (right) in-plane alignment (angle between rolling direction and nearest crystal axis).

Grain boundary maps also show very uniform structure (Fig. 88), in contrast to the presence of well defined grain boundaries for YBCO deposited on RABiTS.

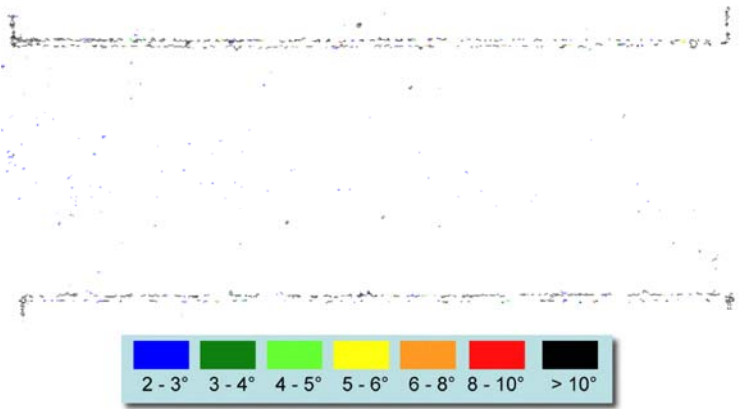


Fig. 88. Grain boundary map of PLD YBCO/IBAD MgO coated conductor.

In-field performance of reel-to-reel deposited films is very similar to that of short samples. In a plot of J_c or Δm , the difference between the magnetization for decreasing and increasing magnetic field, and which is proportional to J_c , as a function of magnetic field shows a power law behavior, $J_c \approx \mu_0 H^{-\alpha}$, where α is a measure of in-field performance with lower value indicating a slower drop off with of J_c with increasing field. The in-field data (Fig. 89) compare quite favorably to that of other films: for a 1 μm thick YBCO/IBAD MgO film $\alpha \sim 0.4-0.5$, and with BaZrO₂ (BZO) doping, $\alpha \sim 0.3$

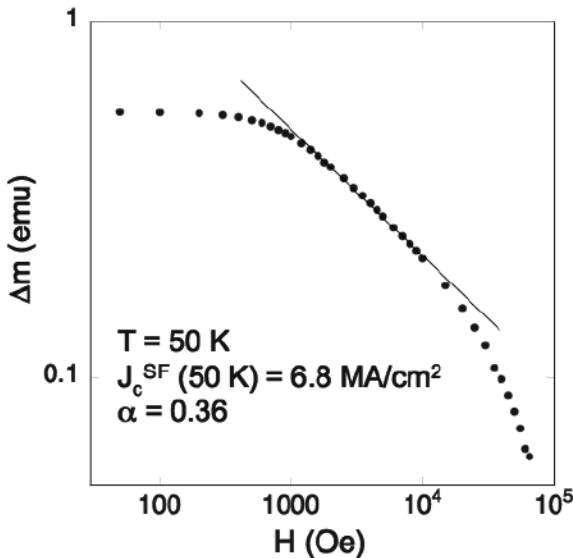


Fig. 89. Δm as a function of applied field for a coated conductor film at 50 K shows power law behavior.

The wire processing program produced a new longer length result (Fig. 90a) for a mean I_c of 350 A at 75 K and self field in a 3 μm thick film - 1.2 m long tape for a J_c of 1.17 MA/cm². On a shorter 7 cm segment (Fig. 90b), the I_c was 425 A, and the n value ($V \sim I^n$) was 27 for a 4 μm thick film. Because of the variation in J_c across the film width (inset of Fig. 90b), slitting the film to a 6 mm width yielded an I_c of 530 A/cm width and a J_c of 1.33 MA/cm².

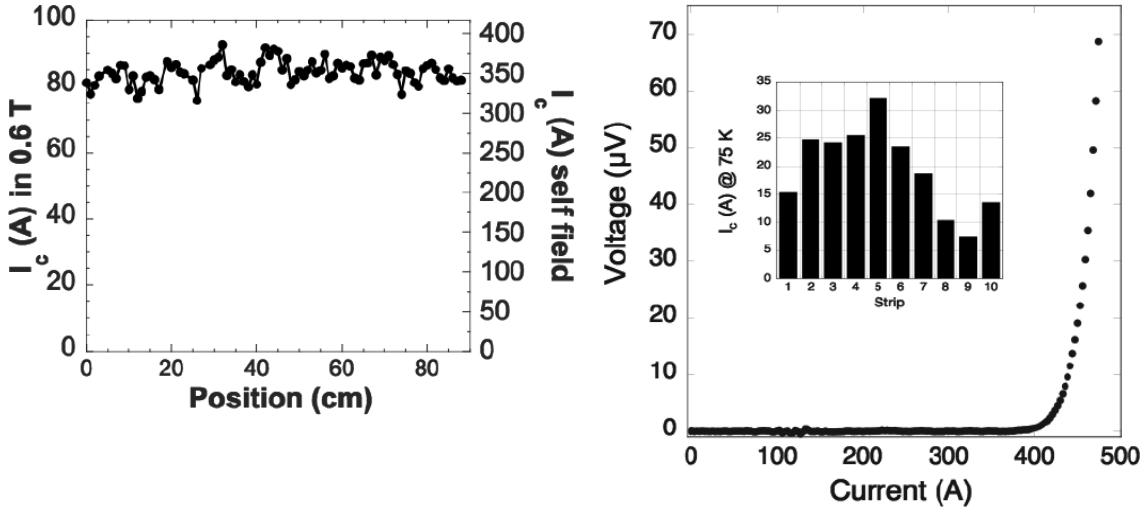


Fig. 90a. Critical current as a function of position along a 1.2 m long tape. Mean I_c (75 K, sf) is 350 A. Fig. 90b. I-V curve and I_c distribution across the tape width of a 7 cm, 525 A tape.

In addition to our work on fabricating coated conductor tape, we have also added the capability to measure critical currents up to 500 A on 4 cm wide material in collaboration with an industrial partner. This system is shown in Fig. 91.

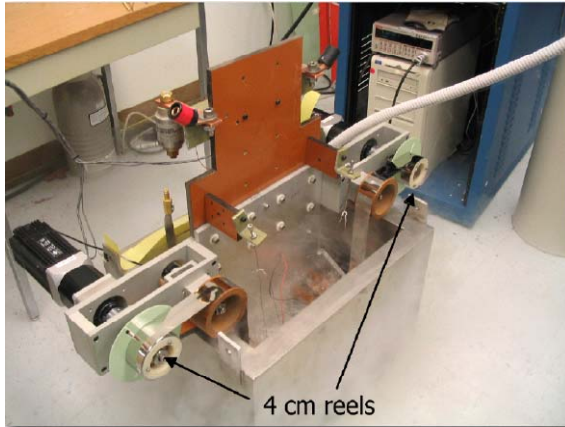


Fig. 91. Photograph of reel-to-reel tape measurement system set up for 4 cm wide conductor.

Fig. 92a shows the improvement in performance of our coated conductor tape over the last 12 months. These results are now comparable to values achieved on small single layer bridges from our research program. Fig. 92b shows worldwide results for coated conductor tape.

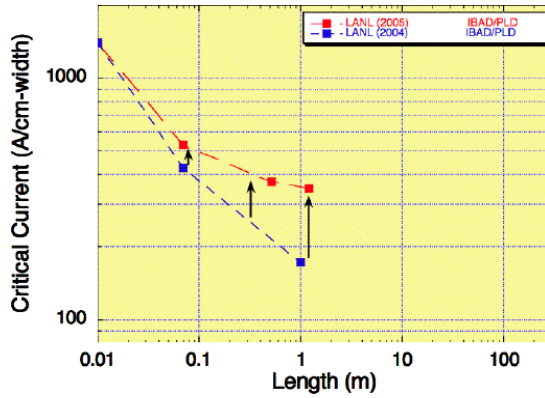


Fig. 92a. Critical current per cm width as a function of length for LANL tapes during the past year.

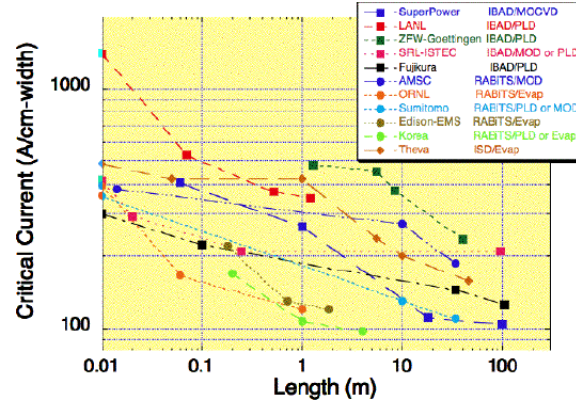


Fig. 92b. Critical current per cm width as a function of length for leading institutions producing coated conductor tapes.

Summarizing the results presented here for our IBAD activities, we have reduced the time for high quality IBAD to less than 2 seconds, simplified the IBAD stack by eliminating one layer, and started research into a new tape preparation process with a sol-gel layer. The high rate deposition allows production of IBAD template film at up to 270 m/h with 7° in-plane texture. Typical production rates result in 10 m lengths of IBAD with texture of $\sim 4 - 6^\circ$. We have developed a robust CC IBAD architecture needed for the different YBCO processes by working with industry resulting in the removal of the $\alpha\text{-Al}_2\text{O}_3$ layer and employing a thicker MgO layer with resultant better texture.

Superconductor results on the IBAD template using PLD to produce the buffers and YBCO, we have achieved 350 A ($J_c > 1 \text{ MA/cm}^2$), on a 1.2 meter length and 530 A/cm-width on short samples deposited on a moving tape. I_c variation on a 2-cm measurement length scale over $> 1 \text{ m}$ was reduced to 7% with the discovery that there was positional variation across the tape width.

We also polished long lengths ($> 100 \text{ m}$) of tape for industrial partners, using special processes to suit their needs. IBAD tape was provided to industrial and university partners. We developed equipment (such as the 4-cm wide I_c measurement) and characterized numerous samples for our collaborators. We collaborated with Sandia NL on barrier/nucleation layer by sol-gel.

2.1.5 Study of Overcurrent Behavior in YBCO Coated Conductors Using a Localized Magnetic Field

J.Y. Coulter, S.P. Ashworth, P.C. Dowden, B.J. Gibbons, V. Matias, and J.O. Willis

Thermal stabilization of $\text{YBa}_2\text{Cu}_3\text{O}_x$ (YBCO) coated conductor high temperature superconductor tape is required in most applications. The conductor must carry currents in excess of the critical current (I_c) without damage during over current events. Conductor damage is the result of joule heating and excessive temperature rise in regions with low I_c . We have developed and applied a measurement technique using a locally applied magnetic field with a high spatial gradient to define a small area over which the I_c is depressed. By measuring the voltage and temperature as a function of current, power dissipation and temperature rise were determined. Unstabilized conductors experienced thermal runaway and are easily damaged. Copper stabilizers applied by electroplating decreased dramatically the temperature rise and increased the level of power dissipation compared with the unstabilized conductor.

At currents in excess of the critical current, I_c , a superconductor, and YBCO coated conductor tape in particular, generates a voltage that can be approximated as $V=V_c(I/I_c)^n$, where V is the voltage, I is the current, V_c is the voltage criterion for determining the critical current I_c , and n is the power law exponent commonly called the n value. Power dissipation in the conductor in the form of joule heating is generated according to $P=VI$. I_c measurements of coated conductors are most commonly made in a bath of liquid nitrogen at temperatures 77 K-64 K. At low power levels convection cooling results in relatively inefficient heat transfer to the cryogen. At higher power levels, nucleate boiling occurs with small nitrogen bubbles generated at the heated surface, which then move away into the liquid. This results in very good heat transfer. Eventually, film boiling and poor heat transfer returns. At these high power levels, the temperature of the conductor can rise rapidly, and conductor damage may result as shown in Fig. 93. This damage has been documented, and a technique for the nondestructive characterization of the positional dependence of I_c has been developed and is currently in use in our laboratory.



Fig. 93. Response of an unstabilized coated conductor tape to an overcurrent.

Within the last several years, practical coated conductors have been fabricated with an integral stabilizer of copper applied by electroplating or by soldering on top of the typically much thinner silver overcoating. This has greatly improved the ability of the conductor to withstand overcurrent conditions without damage. How the addition of stabilizer material affects the voltage / current and the thermal characteristics at high currents is not well known. In this paper, we present a measurement technique that allows the determination of the temperature rise from overcurrents in a small section of conductor defined by the application of a localized magnetic field that depresses I_c . In addition, the applied field reduces the n value in the same localized region from a

typical self field value (I_{csf}) of ~ 32 to values of ~ 10 to 15 in fields close to 1 T. This results in a more gradual increase in voltage, and thus in power and temperature, compared to the situation at self-field, as I is increased above I_c . The areas of the conductor outside the applied field region retain their (higher) self-field I_c and thus do not contribute significantly to heating. We present data on two coated conductor tapes distinguished by different thicknesses of sputtered silver and electroplated copper stabilizer.

This measurement configuration is also more representative of the environment for actual applications, such as power cables, current leads, and other superconducting devices operating in liquid nitrogen and modest magnetic fields. Determining the performance of stabilized conductors and optimizing this for a particular application are the ultimate goals of this research.

To begin, three coated conductor tapes were prepared using $100\text{ }\mu\text{m}$ thick electro-polished Hastelloy substrate with a biaxially textured magnesium oxide template film produced with ion beam assisted deposition (IBAD). Homoepitaxial MgO and other buffer layers were then deposited before the pulsed laser deposited $1.4\text{ }\mu\text{m}$ thick YBCO layer. All samples have a magnetron sputtered silver overcoat for environmental protection and for ease of attaching electrical leads. The samples were 10 - 15 centimeters in length and 1 cm wide. Sample A has a $3\text{ }\mu\text{m}$ overcoat of Ag. Sample B has a $6\text{ }\mu\text{m}$ overcoat of Ag and $25\text{ }\mu\text{m}$ of electroplated copper. Sample C has a $3\text{ }\mu\text{m}$ overcoat of Ag and $50\text{ }\mu\text{m}$ (each side) of electro-plated copper in the fully enclosed, double sided, geometry described by Selvamanickam at the 2004 DOE Peer Review. The electroplated copper was deposited in a standard bright acid sulfate copper-electroplating bath at 0.2 A/in^2 (30 mA/cm^2) of sample area for 90 minutes. The plating bath is used commonly in the plating industry, and its make-up is as follows: copper sulfate 225 g/l , sulfuric acid 70 g/l , chloride ion 30 ppm , UBAC R-1 Brightener (Udylite Company) 0.25% by volume. The solution was used at room temperature with bubbling air agitation.

The measurement and quantification of heating under overcurrent conditions typically has two problems: 1, determination of the exact spot generating the heat, and 2, determination of the area over which the heat is generated. During a V/I measurement of a coated conductor, the first location that will develop a voltage is the one with the lowest I_c . This hot spot will also start heating the sample, and that heat will propagate along the length and width of the tape. The resultant temperature rise lowers the I_c of regions adjacent to the hot spot, which may result in them exceeding their I_c and dissipating energy. This makes the determination of the area of the hot spot difficult.

To avoid these two problems we applied a local magnetic field generated by two rare earth magnets on either side of the superconductor (Fig. 94a) and made use of the $I_c(B)$ dependence of the coated conductor to reduce I_c in a strip across the width of the sample as defined by the magnetic field profile (Fig. 94b). There are many benefits to this method: the region of lowest I_c is precisely located, the area over which the field is applied is well known, and therefore the area of dissipation is known. The surrounding regions have much higher (i.e., self field) I_c values and therefore do not substantially limit the magnitude of the overcurrent in the in-field region.

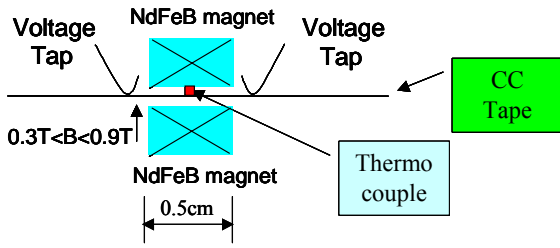


Fig. 94a. Schematic diagram of the experimental measurement configuration.

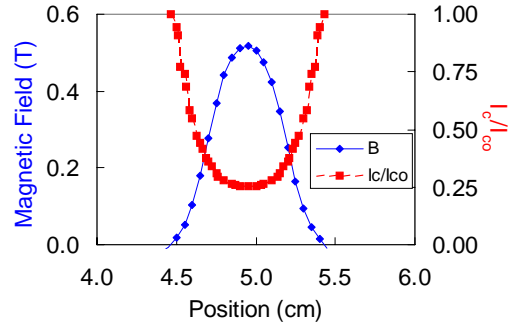


Fig. 94b. Magnetic field generated by 2 NdFeB magnets separated by a distance of 0.64 cm and normalized critical current of a coated conductor tape as a function of position along the tape

Voltage taps were soldered to the coated conductor in close proximity ($\sim 1\text{-}2$ mm) to the magnets (Fig. 94a). An infield value of $(I_{csf})/Y$ allows the current to be ramped to $\sim Y \times I_c(B)$ with negligible dissipation and resultant heating in the regions adjacent to the applied field. The field does vary somewhat over the width of the magnets; however, the peak region of 0.5 cm has only a 10% variation in magnitude. The maximum depression of I_c occurs here. As the overcurrent is increased and dissipation begins to increase, any temperature rise will decrease the I_c in both the region of interest and in adjacent regions with substantial localized magnetic field.

In the present experiment, the sample was suspended equidistant between two neodymium iron boride magnets measuring 0.5 cm by 0.5 cm by 2 cm a distance 0.64 cm apart that generate a magnetic field of 0.3 T, resulting in a ratio $I_c(0.3\text{ T})/I_{csf} \sim 0.33$. From measurements of $I_c(75.5\text{ K}, B)$ of a typical coated conductor without a copper stabilizer, such as the present sample A, we observed no heating in regions adjacent to the region being measured at currents up to $\sim 3 \times I_c(75.5\text{ K}, 0.3\text{ T})$. We then mounted a chromel-constantan differential thermocouple, having a sensitivity of $26\text{ }\mu\text{V/K}$ at 75 K, on the surface of the sample electrically insulated with a thin coating of GE 7031 varnish. Voltage taps were soldered as close as possible to the region of applied magnetic field (Figure 1). Two data sets were taken. In the first set, I_c was measured with a pause time between current steps just long enough to allow the Keithley nano-voltmeter to settle (~ 0.2 s). This data set was used to determine I_c . Voltage along the sample and the thermocouple voltage were recorded in the second data set. This second curve was taken with the much longer pause time between current steps of ~ 2 and 5 s; this accommodated the longer thermocouple time constant. As no appreciable difference was seen between the data acquired at these two pause times, a 2 s pause time was used to acquire the data. The current through the sample was increased above I_c and voltages measured up to 3000 to 5000 μV . All measurements were made with the coated conductor tape plane horizontal, and thus with the YBCO crystallographic c axis oriented vertically, in a liquid nitrogen bath at $\sim 75.3\text{ K}$. The areas for power dissipation into the bath were calculated as that of one surface for samples A and B. Because the thermal conductance of the YBCO, buffer layers and Hastelloy substrates is only about 2% that of copper at 75 K, it was assumed that essentially all the power was dissipated from only the surface closer to the YBCO. For sample C (double sided copper), the calculation assumed that power was dissipated equally from each surface of the tape.

Sample A (3 μm Ag overcoat) had an $I_c(75.5 \text{ K}, 0.3 \text{ T})$ of 25 A and an n value of 12, as shown in Fig. 95a. The thermocouple measurements (Fig. 95b) indicated an ability to sustain a power dissipation (Q) of only 0.05 W/cm^2 with a maximum temperature rise (dT) of 0.07 K . In this region Q is proportional to dT with a constant of proportionality, the heat transfer coefficient (k), of 0.7 W/Kcm^2 . This value of k is typical of convective heat transfer; this is supported by the observation that there was no boiling at the sample surface. At a current of $\sim 1.2 \times I_c$ the dissipation and heating were indicated by a voltage jump reflecting a large change in the power being dissipated. Although the temperature as indicated by the thermocouple reading did not respond proportionately, the measurement was terminated to avoid imminent sample damage.

The stabilized YBCO coated conductor sample B with $6 \mu\text{m}$ magnetron sputtered silver overcoat and $25 \mu\text{m}$ electroplated copper on one side has an $I_c(75.5 \text{ K}, \text{sf})$ of 220 A, an in-field $I_c(75.5 \text{ K}, 0.3 \text{ T})$ of 60 A, and an n value of 13 for voltages less than $100 \mu\text{V}$. At voltages higher than $\sim 2000 \mu\text{V}$, however, the n value drops to ~ 2 , and the feedback process that drives thermal runaway is much slower than for Sample A, resulting in a more stable system (Fig. 96a). Thermocouple measurements (Fig. 96b) indicate a heat transfer coefficient k at low dissipations of 0.42 W/Kcm^2 up to a maximum temperature rise of 2 K and dissipation of $\sim 0.9 \text{ W/cm}^2$. At this dT , boiling commenced on the sample surface, and the temperature and voltage generated both abruptly decreased; above this point k increased markedly to 7.5 W/Kcm^2 . From this we conclude that the superheat required to initiate boiling on these electroplated surfaces is approximately $\sim 2 \text{ K}$.

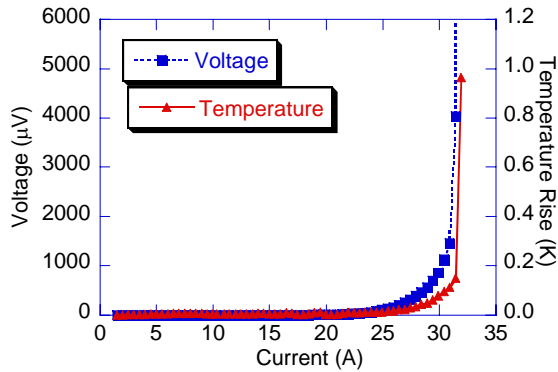


Fig. 95a. Voltage and temperature rise as a function of transport current for sample A (unstabilized). The $I_c(75.3 \text{ K}, 0.3 \text{ T})$ is 25 A; the n value is 12. The sample became unstable above $\sim 33 \text{ A}$ ($\sim 1.2 \times I_c$).

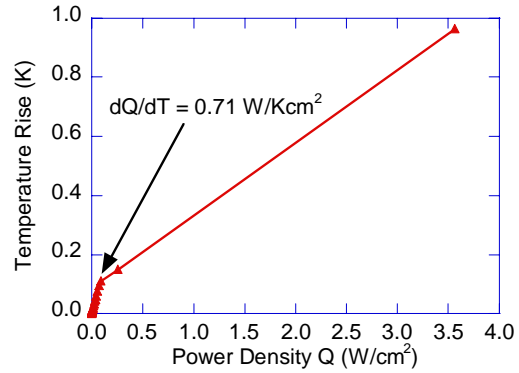


Fig. 95b. Temperature rise as a function of power density for sample A. The sample became unstable at a power density of 0.05 W/cm^2 , at a temperature rise of only 0.07 K .

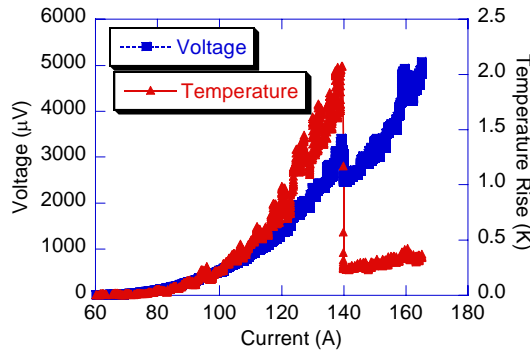


Fig. 96a. Voltage and temperature rise as a function of transport current for sample B with $25 \mu\text{m}$ of copper on one side. Note sharp drop of V and dT near 140 A .

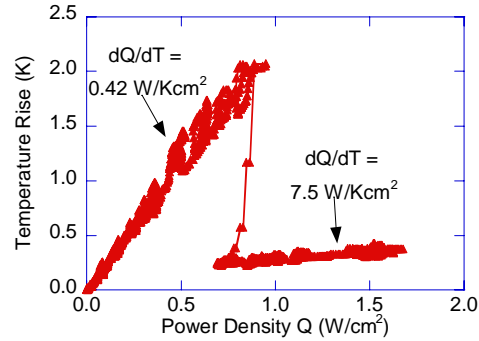


Fig. 96b. Temperature rise as a function of power density for sample B showing clearly the large change of heat transfer efficiency with onset of boiling.

Similar behavior was seen in sample C (Fig. 97), which had a 50 μm thick copper coating on each side. The sample had an $I_c(75.5\text{ K, sf})$ of 220 A, an in-field $I_c(75.5\text{ K, 0.3T})$ of 60 A, an n value of 13 for voltages less than 100 μV and of ~ 2 above $\sim 2000\text{ }\mu\text{V}$. This sample exhibited a higher k below the inception of boiling of 0.21 W/Kcm^2 and a slightly lower superheat to initiate boiling (1.5 K). Once boiling commenced, k increased slightly to 0.87 W/Kcm^2 . The presence of two (relatively rough) Cu surfaces, rather than one smooth (bare substrate) and one Cu surface, may result in the lower superheating temperature for sample C because of the larger nucleation area.

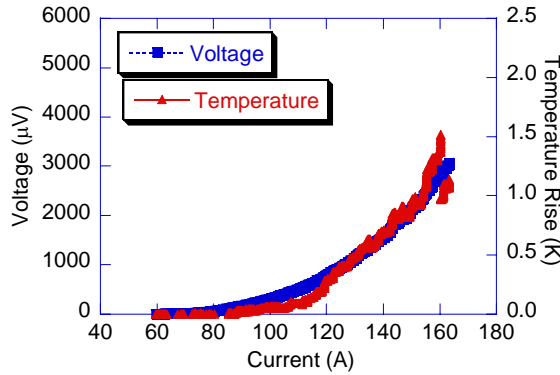


Fig. 97a. Voltage and temperature rise as a function of transport current for coated conductor sample C with 50 μm of copper on each side.

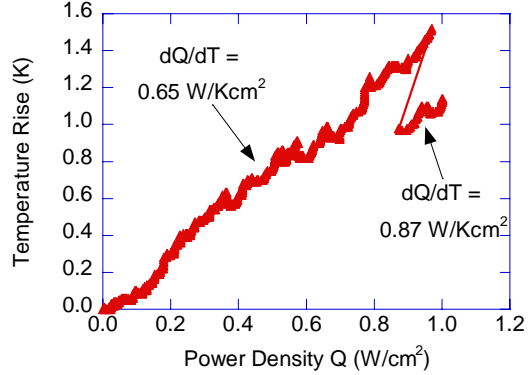


Fig. 97b. Temperature rise as a function of power density for sample C. This sample remains stable at a power density 20 times greater and a temperature rise 23 times greater than that of sample A.

To summarize, a measurement technique for the quantification of locally generated heat flux in coated conductors has been used to characterize three YBCO coated conductors with different current stabilizers. Both Cu stabilized samples (B and C) exhibited similar rates of temperature rise per unit heat flux, which is to be expected as they were measured under the same cooling conditions. The point of critical heat flux varied between the samples, which we attribute to the amount of stabilizer. The function of the stabilizer is to provide a parallel, low resistance current path during over current conditions. The interpolated values for silver and copper resistivity are $0.26\text{ }\mu\text{ohm-cm}$ and $0.20\text{ }\mu\text{ohm-cm}$, respectively, at 75.5 K. Power law analysis of the voltage current curves shows the 3 μm Ag stabilized conductor to have a n value of $>12-14$ for $V < 1400\text{ }\mu\text{V}$. The 100 μm Cu stabilized sample has a high voltage n value of ~ 2 .

Without copper stabilization, sample A goes into thermal runaway before the inception of boiling can increase the cooling efficiency. This is primarily due to the superheat required (about 1.5 - 2.0 K) to initiate boiling on these smooth surfaces. The high n value leads to very strong positive feedback for increasing dissipation as temperature increases. In the copper stabilized samples the effective n value at high currents is reduced by the normal metal ($n=1$) in parallel with the superconductor to an effective value of ~ 2 . It should be possible to reduce the superheat required to initiate boiling by suitable surface treatments; this would allow thinner stabilizer coatings to be used - increasing the engineering current density of the conductor.

2.1.6 Combining modeling and measurements to control the ac losses in coated conductors

F. Grilli, S.P. Ashworth, V. Matias, and B.J. Gibbons

AC Losses are an important problem for coated conductors. Changing the ac magnetic field and/or ac current dissipates energy in all superconductors. This energy (heat) needs to be removed by refrigeration, which is both an economic and an engineering problem. The ac losses are significantly higher than we would like them to be (Fig. 98), in particular the losses due to ac fields perpendicular to the tape face. The vertical arrow indicates the example application of a coil of 10 km of tape with 10% of it in a perpendicular field of 10 mT; the losses would be 1 W/m X 10 km X 0.1 or about 1 kW. The conclusion is that we need to design the conductor for ac applications; simply increasing I_c will not be sufficient to solve the problem.

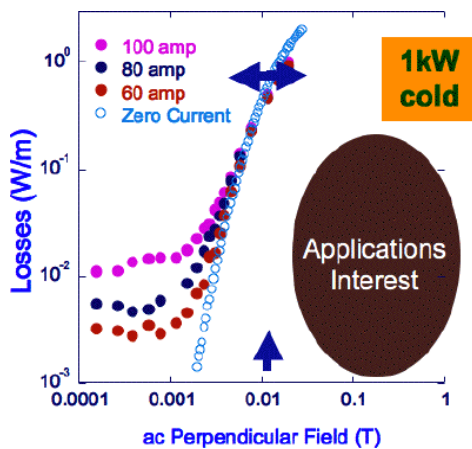


Fig. 98. AC losses for coated conductor tape as a function of ac perpendicular field and ac transport current.

Fortunately, there *are* techniques for reducing AC losses in practical applications. These include reducing losses at both the conductor level and at the coil level. We have found that numerical simulations are a reliable and powerful tool to help us do this, but of course they need to be coupled to experiment. Therefore, we at LANL have implemented an integrated numerical and experimental program that is unique in the US.

It is critically important to evaluate the ac losses before implementation of superconductive devices. The simplest method uses analytical models. However, these are quite limited. They are restricted to an inaccurate description of the voltage-current (V-I) characteristics because they use the critical state model. They are also confined to simple (unrealistic) geometries and either individual tapes or an infinite number of tapes. In contrast numerical methods, in particular the finite element method (FEM), used here can take account of smoothly varying V-I characteristics, of non-constant J_c functions, e.g., $J_c(B)$, $J_c(x,y,z)$, etc., of more realistic geometries, of interactions between a finite number of tapes.

The FEM has been successfully used for calculating ac losses in BSCCO tapes. The software solves Maxwell's equation for transient problems. The geometry is discretized into a grid of elements. The equations are then solved at every point of the grid. From this, electromagnetic quantities may be calculated. The superconductor behavior is modeled using nonlinear electric field – current density (E-J) power law as $E(J) = E_c(J/J_c)^n$, where E_c is the electric field criterion, J_c is the critical current density, and n is the power law exponent. J_c can also vary as a function of magnetic field B or position (x,y,z) as $J_c(B)$ and $J_c(x,y,z)$, respectively.

To move from reality to a useable, useful model, we use the measured current-voltage characteristic to get the constitutive law for superconductors. We also transition from a multifilament tape with many variations to a discretized filament model.

There are only a few groups in the world that focus on FEM of high temperature superconductors: at Yokohama National University (Japan), at the Swiss Federal Institute of Technology – Lausanne (Switzerland), and at the University of Southampton (UK), with little previous effort in the US. Now, LANL has developed a strong combination of experimental and modeling expertise.

We first examine the magnetic losses, i.e., those induced by the presence of an applied ac magnetic field, of individual tapes. Fig. 99 shows the various results. The analytical model and the FEM with a constant J_c show a slope of 4 for fields below full penetration. However, the experimental results for a variety of samples show a lower slope, typically 3.0 to 3.6. If we make the hypothesis that J_c is non-uniform across the tape, the $J_c(x)$ dependence shown in the inset results in a FEM result for the losses in good agreement with the experimental data. DC critical current measurements are also necessary to confirm $J_c(x)$. The conclusions are that the tapes are not uniform across the width but that FEM calculations work.

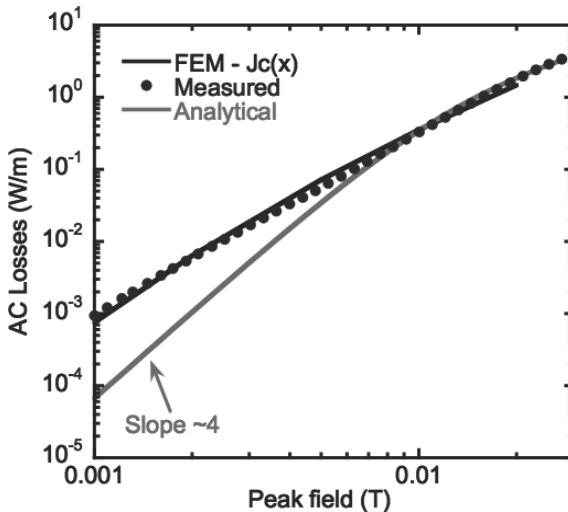


Fig. 99. Comparison of measured and calculated ac losses as a function of applied perpendicular ac magnetic field.

How can we reduce the magnetic losses of individual tapes? The losses are inversely proportional to the square of the width of the tape. This implies multifilamentary tapes for low losses, Fig. 100a. However, the filaments must also experience the same electromagnetic environment (magnetic flux must be able to get between all filaments); this usually means transposition, which is not easy in practice. An alternative way to achieve this goal is to striate the superconductor into filaments AND periodically break the filaments with transversal cross-cuts, Fig. 100b. For this configuration, flux can enter between the filaments and all of them look the same electromagnetically.

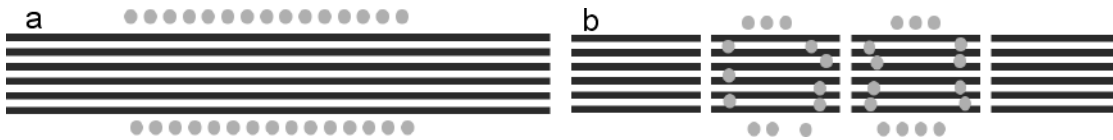


Fig. 100. a) Multifilament tape prevents flux from entering. b) Multifilament tape with transversal cross cuts allows flux to enter between filaments.

We have determined that flux can travel quite far from a cross-cut during an ac cycle. We performed an experiment for a 100 Hz perpendicular ac field on a tape with the configuration shown at the top of Fig. 101. There are no filaments to the left of the cross-cut, and flux can only enter at this point. The flux is then measured as a function of distance from the cross-cut. There is no flux to the left of the cut, and in the filament region, the flux moves at least 10 cm in a cycle. Therefore, 5 cuts per meter are sufficient for significant loss reduction at 60 Hz. Finite element analysis (Fig. 102) confirms this result.

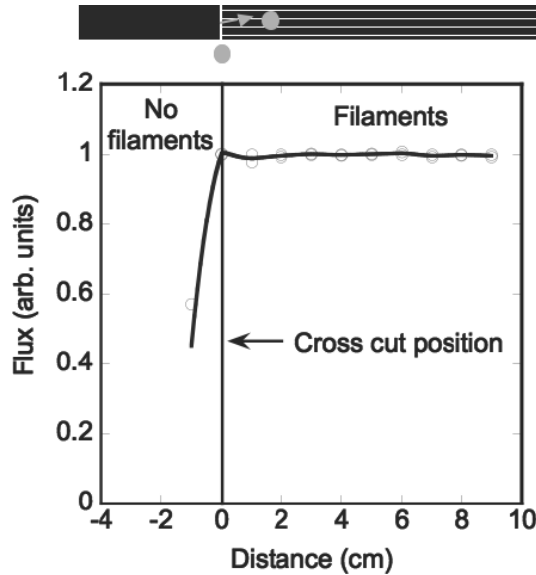


Fig. 101. Top: Schematic of experiment to determine extent of flux penetration into multifilament tape. Bottom: Penetration of flux into the tape as a function of position away from the cross-cut.

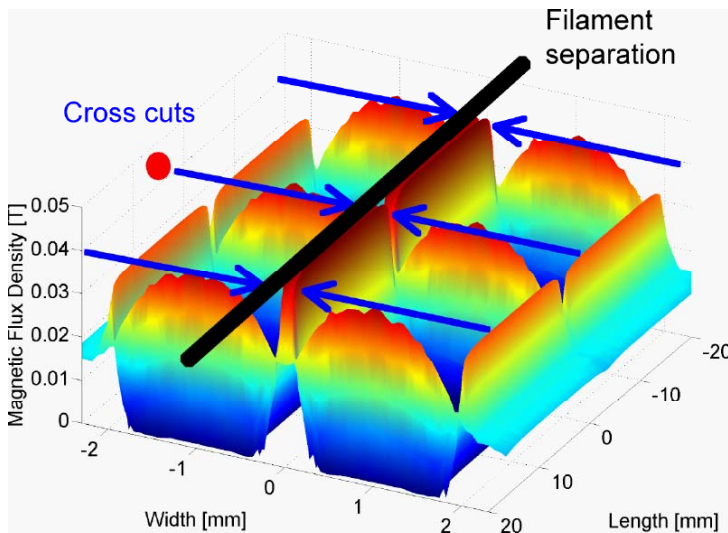


Fig. 102. FEM results for the multifilament tape with crosscuts every 20 cm.

After making the cross-cuts, it is necessary to bridge the cross-cuts with normal metal to carry the transport current. Two types of experimental bridges were made: 50 μm of indium solder and indium plus 25 μm of copper. These bridges produce a resistance of 4 $\mu\Omega$ for a 4 mm wide tape. The cross-cut plus bridge produces a self-field, ohmic ($\sim I^2 R$) loss that is significantly higher than the ac transport loss in the superconductor, Fig. 103a. However, the decrease ($\sim \times 100$) in the much larger magnetic losses, shown in Fig. 103b, dominates.

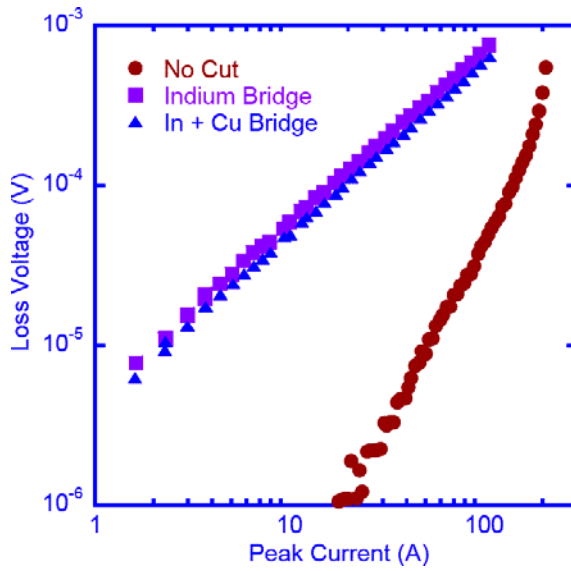


Fig. 103a. Transport current loss for 10 mm wide, 10 filament tapes with and without cross cuts as a function of peak current.

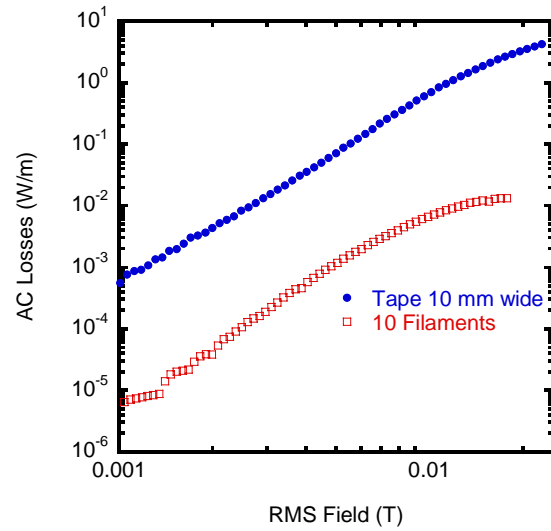


Fig. 103b. Magnetization ac loss for a 10 mm wide tape and one cut into 1 mm wide strips as a function of applied magnetic field.

In the real world case of combined transport current and an ac perpendicular field, Fig. 104a, in very low fields, the 10 mm wide bridge has lower total losses, but above about 4 mT, the experimental bridge with 10 filaments and 5 cross-cuts/m has $\sim x100$ lower total losses at magnetic fields of interest. Possible further improvements can also be achieved by a couple of techniques. Reducing the resistivity of the cross-cut bridge to $0.4 \mu\Omega\text{-cm}$ (as calculated by FEM) gives the Low R bridge curve in Fig. 104b. Decreasing the filament width, or equivalently, increasing the number of filaments to 25/cm width also reduces the losses substantially, and is even more effective at higher frequencies, because the ohmic loss is frequency independent.

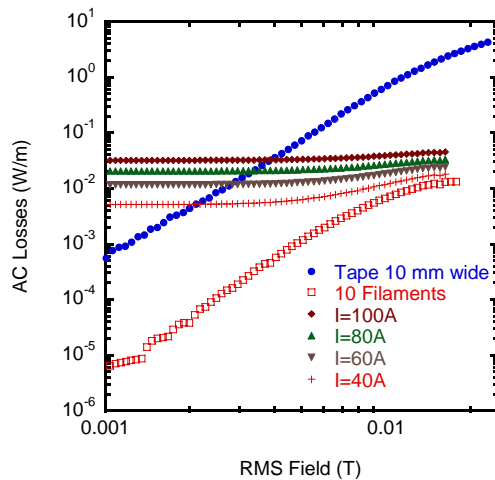


Fig. 104a. Magnetic losses and total losses for a 10 mm wide tape and one with 10 filaments and cross cuts as a function of transport current and magnetic field.

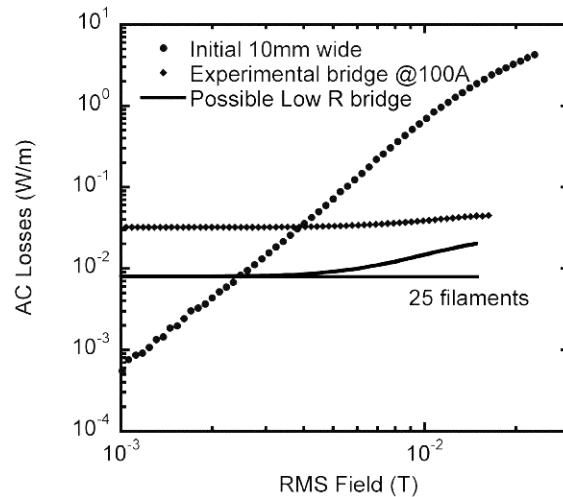


Fig. 104b. Total losses for several tape configurations as a function of magnetic field.

We have also developed a low cost route to filament manufacture using mechanical scribing with microtome blades. This is a continuous process with low additional cost. It has been set up to scribe 10 mm wide tape into 25 filaments at a speed of 1 m/min. We have made lengths to 50 cm. Fig. 105 shows the scribe pattern on the surface of a tape.

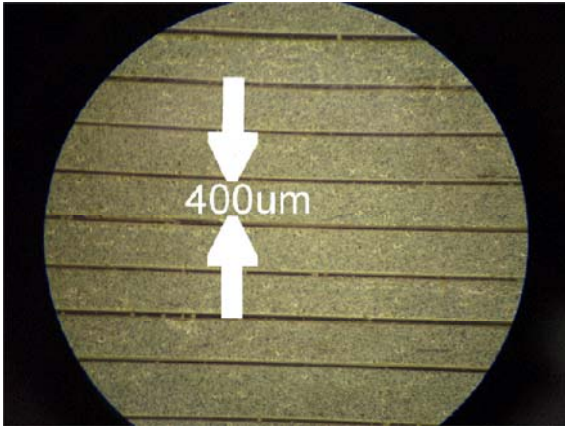


Fig. 105a. Section of cuts in 10 mm wide tape made by microtome blade pack with spacing of 400 μm .

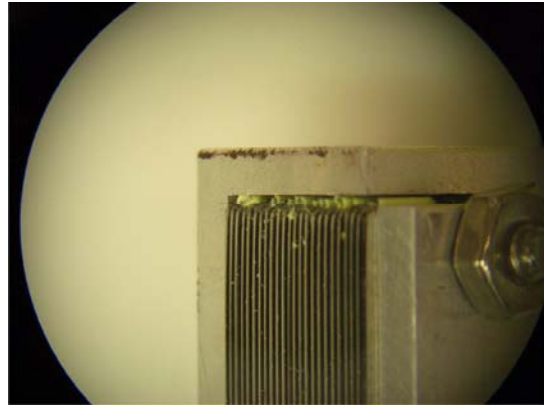


Fig. 105b. Cutting portion of 24-blade microtome blade pack.

The standard microtome blades are held together in a pack and the tape translated under the blades to form the grooves as shown in Fig. 106a. Because it is difficult to align the blades precisely in the vertical, some flexure in the pack is allowed to ensure alignment, as shown in Fig. 106b. Fig. 106c shows the topography of a cut.

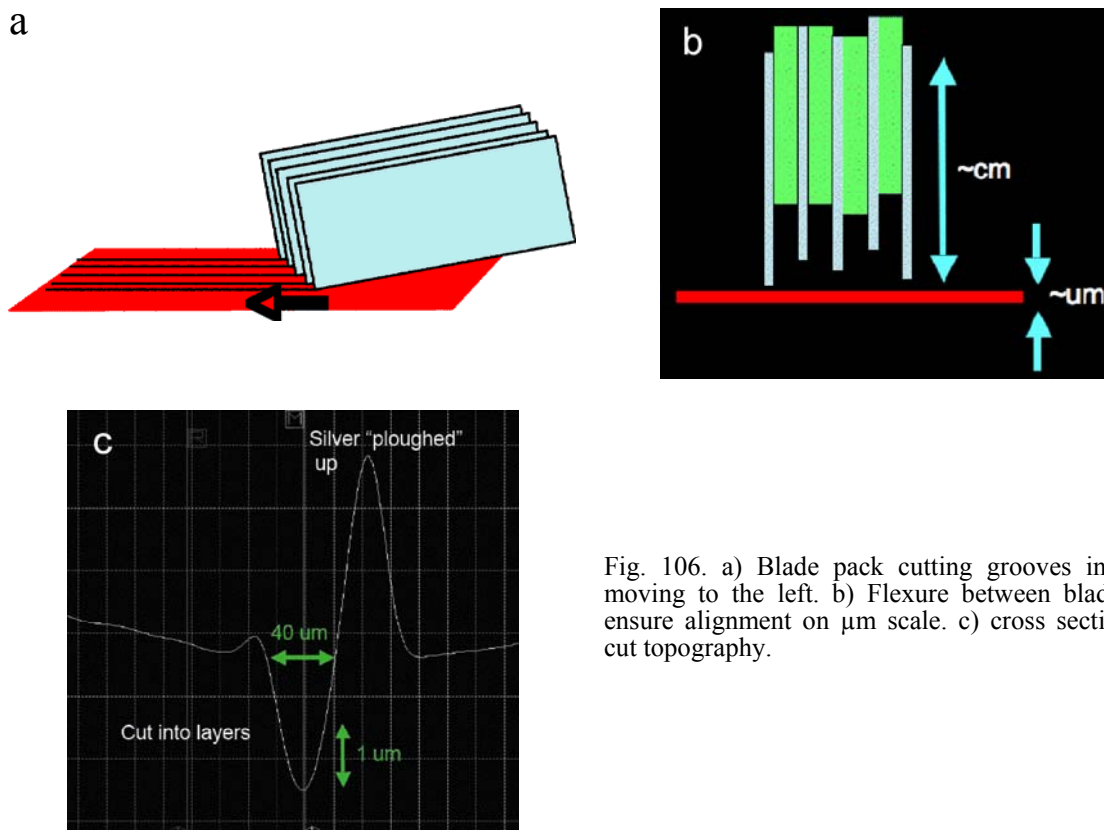


Fig. 106. a) Blade pack cutting grooves in tape moving to the left. b) Flexure between blades to ensure alignment on μm scale. c) cross section of cut topography.

To summarize our work on single tapes, we have demonstrated a loss reduction of nearly 2 orders of magnitude for a tape at 100 A, 10 mm wide, in a 30 mT peak field using the technique of filamentarization and cross cutting. We have also indicated a couple of methods for a loss reduction of 2 to 3 orders of magnitude for the same conditions. However, it is still necessary to twist the conductor to achieve zero net flux threading the superconductor or else eddy currents will be induced. For conventional low temperature superconductors, the pitch length was on the order of a centimeter, not easy to achieve in tapes. However, in a typical coil, one twist every turn (also suggested by M. Sumption, IEEE Trans Appl. Supercond. 2005) is actually sufficient, and in very high symmetry coils, no twist is required.

We have considered the loss reduction in individual tapes, but real devices are assemblies of tapes, and electromagnetic interactions make things more complicated. Stacking of multiple tapes changes the losses. Analytical models, which are available for infinite stacks of tapes, predict that the losses decrease with decreasing separation in an applied field (Fig. 107a) and that the losses increase with decreasing separation for tapes carrying a transport current (Fig. 107b). In the combined case of conductors carrying a transport current in a perpendicular magnetic field, the analytical models predict that there is no optimum separation, but that the transport losses should dominate. Finite element model simulations of an 8-tape stack show (Fig. 108a) very high concentration of magnetic field intensity at the edges of the tapes.

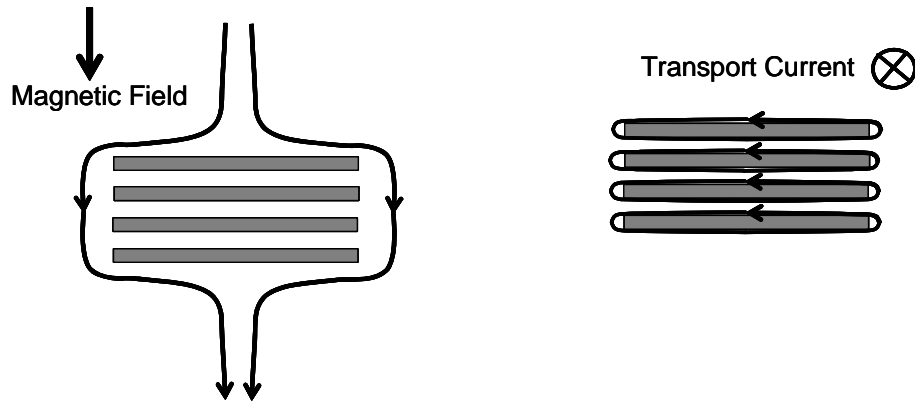


Fig. 107a. Magnetic field distribution for a stack of tapes in an applied perpendicular magnetic field.

Fig. 107b. Magnetic field distribution for a stack of tapes carrying a transport current.

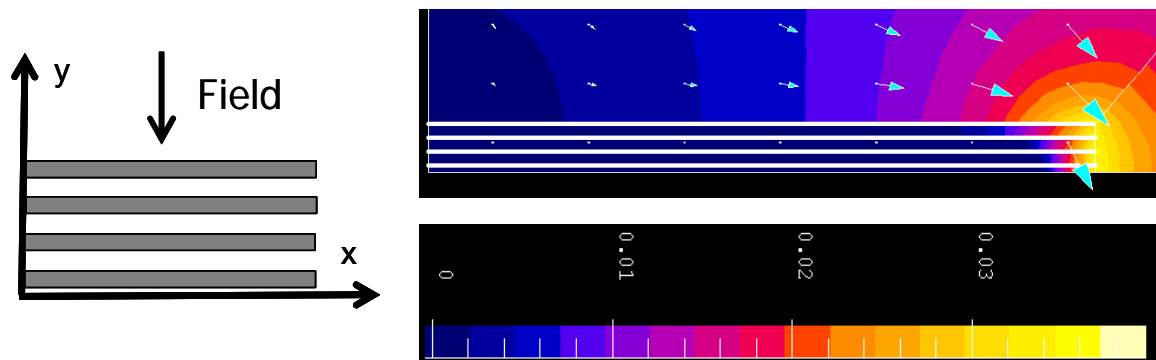


Fig. 108a. Symmetry considerations reduce the volume of material for FEM simulation of a stack of 8 tapes to 1 quadrant and to a 2D problem.

Fig. 108b. Results of FEM simulation of an 8-tape stack. The arrows indicate the direction and magnitude of the magnetic field. The scale in the lower part of the figure shows the field intensity color code.

In contrast to the predictions of the analytical model, the FEM simulations predict that the loss per tapes decreases significantly as the tape separation decreases. Fig. 109 demonstrates this result. The upper curve is just the sum of the losses of the 8 tapes, as there is no interaction when they are far apart. At a separation of 1 mm, the simulations predict (middle curve) that the losses will decrease by a factor of 10. Finally, for a separation of 0.1 mm (lowest curve in Fig. 109), the losses decrease by a factor of 30.

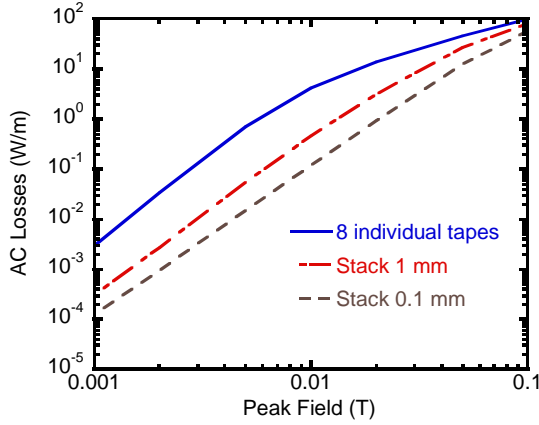


Fig. 109. AC losses as a function of peak perpendicular applied field for 8 individual tapes and stacks of 8 tapes with separations of 1 mm and 0.1 mm.

We find that both our FEM simulations and actual measurements on stacks of 1 to 8 tapes confirm (Fig. 110) that the losses per tape decrease as the number of tapes increases.

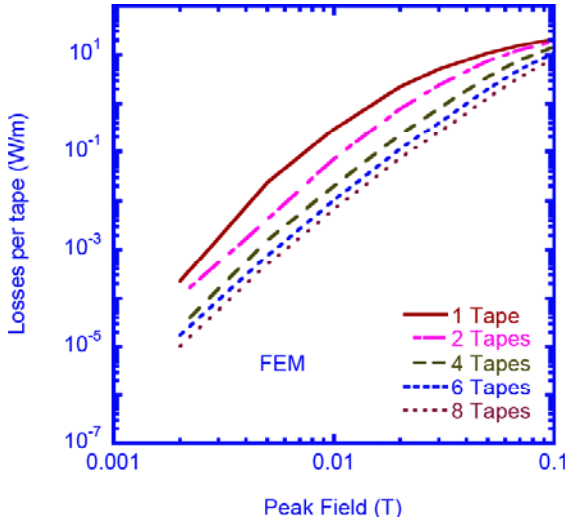


Fig. 110a. FEM simulations of the ac losses per tape as a function of peak field for a stack of 1 to 8 tapes.

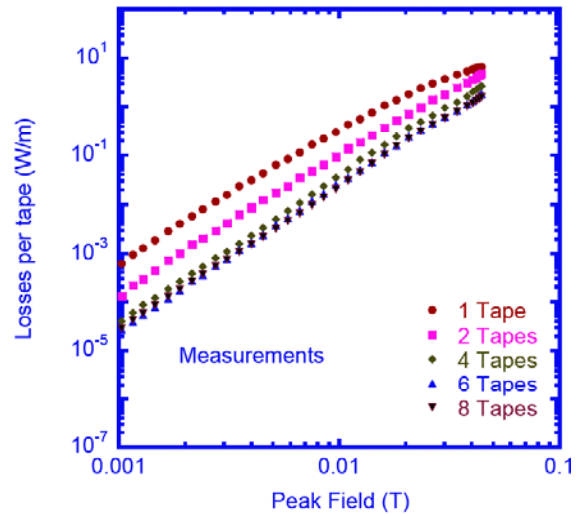


Fig. 110b. Measured ac losses per tape as a function of peak field for a stack of 1 to 8 tapes.

Our FEM simulations also indicate (Fig. 111a) that the transport losses do increase moderately as the separation of a stack of tapes decreases. The losses for a stack of 8 tapes are a factor of 6 to 7 greater than that for 8 separate tapes. Note that this is much lower than the >100 increase in loss predicted by the analytical model. Thus, the FEM simulations show that the loss increase here is not unreasonable and is outweighed by the reduction in magnetic losses. Fig. 111b shows the results of measurements of the transport losses for a stack of 4 tapes. Here, no increase is seen and may be the result of non-constant $J_c(x)$ (across the tape); this result is not yet understood.

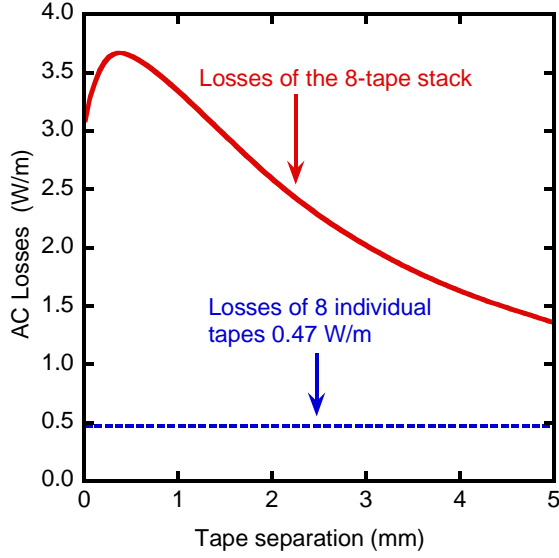


Fig. 111a. FEM simulations of the transport losses of 8 individual tapes and of an 8 tape stack as a function of tape separation.

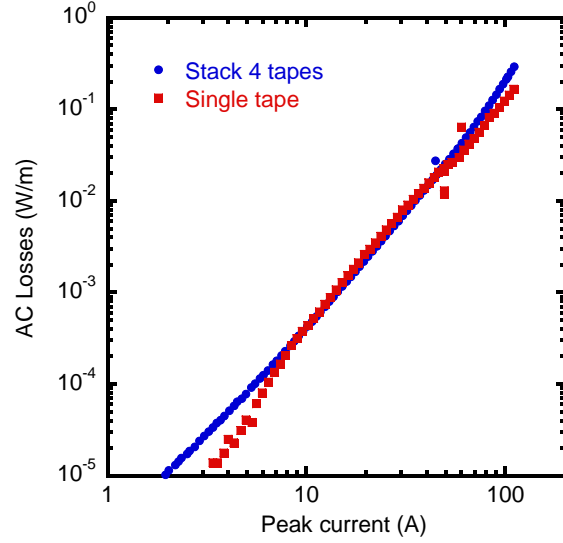


Fig. 111b. Measurements of the transport losses of a single tape and stack of 4 tapes. The result is not understood and may be the result of sample non-uniformity.

Summarizing these results, we find from both FEM simulations and from measurements that we can reduce ac losses in systems of tapes. In an applied magnetic field, the loss decreases by a factor of 10 to 30 for <1 mm separation. With a transport current, the loss increases a factor of 6 to 7 for <1 mm separation. This means that there is a window of reduced losses for current and field applications.

For the future, we plan to develop and test conductors ~ 10 cm long having losses <0.1 W/m when carrying 100 A in 0.1 T (10 mT at present) ac fields. We also plan to develop a route to conductors having losses <1 W/m in ac fields to 1 T. This is a very severe requirement, but it is needed. We plan to work with the software developer to develop a technique for calculating losses in a coil, for example. This will merge micro and macro regimes to calculate the losses in a ~ 1 m scale coil based on HTS tape $\sim 10^{-6}$ m thick. We would like to further extend and validate our models, checking against experiment, in particular, to examine the interaction of transport currents.

2.2. Systems Applications

2.2.1 Design and development of a 100 MVA HTS generator

E.N. Schmierer, T.A. Jankowski, F.C. Prenger, J.A. Stewart, J.A. Waynert, S.P. Ashworth, D.E. Peterson, and (Univ. New Mexico) A. Razani

This work is part of a CRADA with GE to demonstrate a 100 MVA generator. LANL's technology areas are long term vacuum maintenance, alternative rotor cooling methods, thermal modeling of the cooling system, and engineering support with ac loss characterization and assessment of 2nd generation wire impact.

The achievement of a low heat load of the generator system relies on successful long term vacuum maintenance. Basically, the reduction of the residual gas pressure lowers the refrigeration load, and therefore the cost of refrigeration. Vacuum maintenance is a combination of two factors 1) the outgassing properties of materials used in the generator (gas species and quantity of each species as a function of time) and 2) getter material sizing (maintains the low pressure by absorbing gas species, but has limited capacity. Fig. 112 illustrates both of these components.

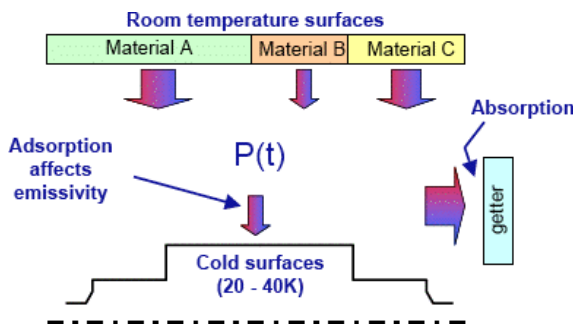


Fig. 112. Surfaces at room temperature outgas and unless absorbed by a getter, result in a heat load on cold surfaces.

The data generated from this study allows GE to make more reliable estimates of getter lifetimes and of the heat loads. Alternatives to Rulon and Ultem, GE products similar to G10 in application, were measured. In addition, humidified samples of G10, more representative of the assembly environment, a simulation of the actual assembly process of the generator, and the effect of exposure to the atmosphere were all included in the testing process. Fig. 113 indicates some of the experimental results. Table 3 lists numerical values for the outgassing rates for some materials.

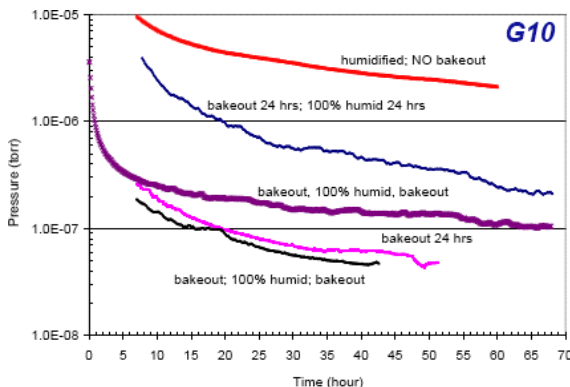


Fig. 113. Outgassing rate as a function of time for various materials and treatments.

Table 3. Outgassing rates for selected materials

| Material | True outgassing rate (Torr-liter/cm ² -sec) |
|---|---|
| Aluminum sheet | 3.40E-09 |
| stainless steel sheet | 6.00E-10 |
| G-10 sheet | 7.00E-7 |
| silver plated stainless | 2.00E-8 |
| Aluminized Mylar | 5.00E-8 |
| Brush plated SS sheet | 7.00E-9 |
| Soft iron | 2.00E-9 |
| Rulon | 4.00E-7 |
| Ultem | 8.00E-7 |
| Carbon fiber reinforced | 1.00E-7 |
| G-10 baked at 150°F 24 h | 6.00E-8 |
| G-10 twice humidified and baked at 150°F 24 h | 3.80E-8 |

The use of a heat pipe (Fig. 114) for rotor cooling in the generator has a high payoff. The heat pipe makes use of a two-phase fluid as the heat transfer media making the device nearly isothermal. As a result, the temperature difference dT between the rotor and the coupling is smaller. The temperature gradient of the rotor is also reduced. This all results in increased efficiency and reduced refrigeration cost. Other advantages are that the sealed device is simple and operates passively, and that redundant cooling is possible.

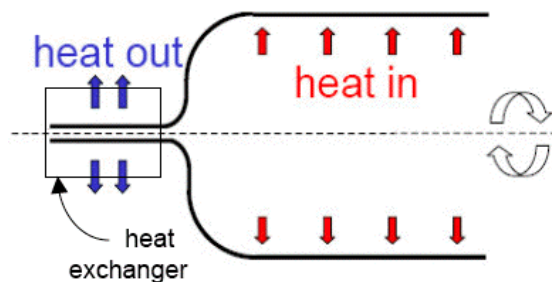


Fig. 114. Schematic of rotor (right) and coupling (left) with heat pipe transferring the heat.

To date, the first two phases of heat pipe development have been completed. We have developed the thermal fluid heat pipe model including optimal fluid fill calculations. This model uses the full Navier-Stokes equation, and has been presented at the 2004 ASME Heat Transfer Conference. We have also fabricated a heat pipe and have benchmarked the model with stationary experimental results. The comparison between experimental and model results is favorable, and the model continues to predict promising results, a 1.5 K or 40% reduction in dT as shown in Fig. 115, for the HTS rotor.

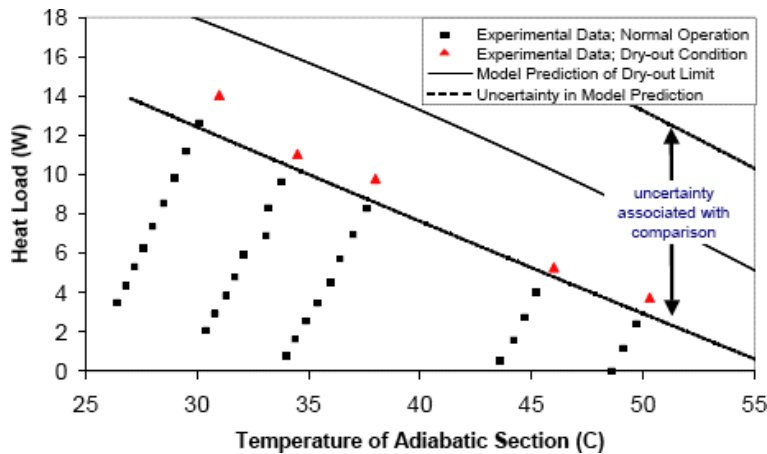


Fig. 115. Experimental vs. model predictions for a heat pipe with a 4° adverse tilt.

All of the preparations for the rotating experiment are complete. The heat pipe design requires a wick structure that can operate in two different modes: stationary during cool down with the annulus full and at high RPM during operation with the annulus partially full. The dual-mode wick fabrication and bending were technically challenging. Several design iterations were fabricated and tested. Finally, a reliable and repeatable fabrication method was determined, Fig. 116. Thereafter, the project underwent an extensive safety review and authorization for a test plan at 3600 RPM. The project is now ready for the final stage of development, that is, the rotating tests.

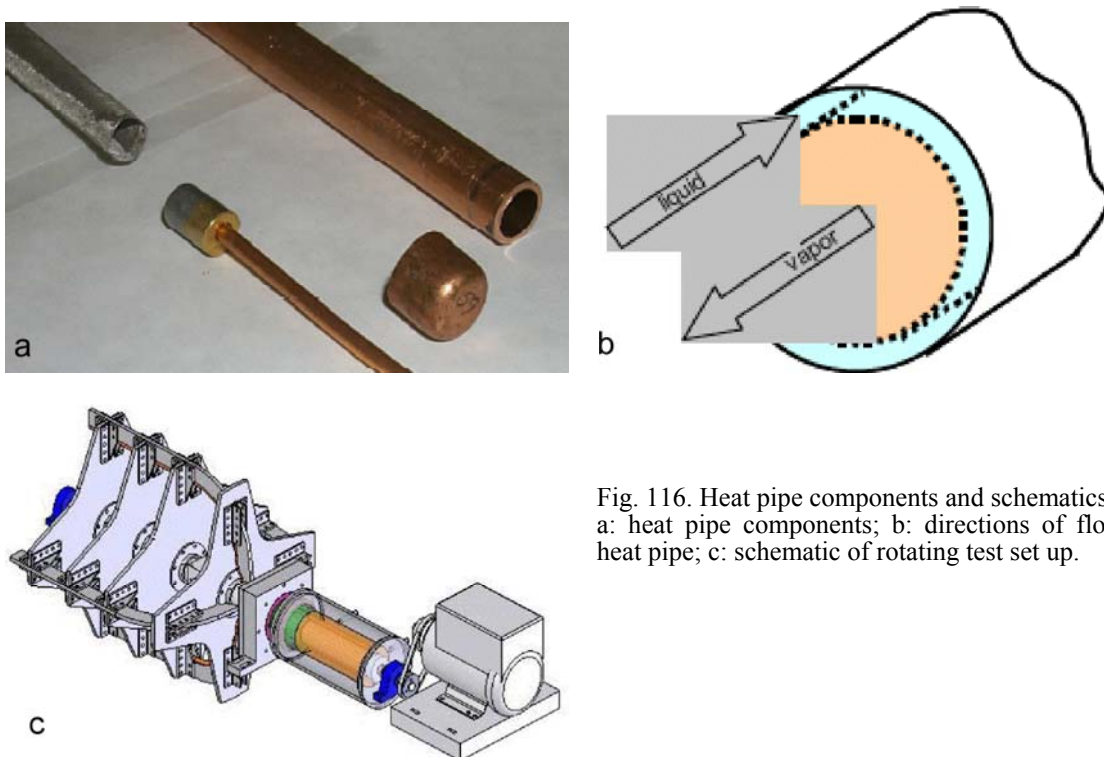


Fig. 116. Heat pipe components and schematics. a: heat pipe components; b: directions of flow in heat pipe; c: schematic of rotating test set up.

An understanding of the magnitude of the heat load is critical to successful engineering of the cooling system for the generator. One component that is technically difficult to estimate is that of the ac losses in the superconductive rotor. The presence of AC magnetic fields results in joule heating in these windings during normal operation. During a fault current (FC) condition (Fig. 117a), the superconductive magnet could quench, leading to possible damage and loss of capability. To this end, test equipment was fabricated (Fig. 117b) to determine the fault current response of an HTS coil and validate the modeling (Fig. 117c). The coil to be tested had an ID of 127 mm, and OD of 160 mm and had 279 turns in 4 layers and a critical current I_c of 150 A at 30 K. The magnet and a FC profile were provided by GE. The coil was analyzed by finite element analysis (FEA) and preliminary tests were performed. Following some needed modifications to the equipment, measurements are scheduled in late FY05.

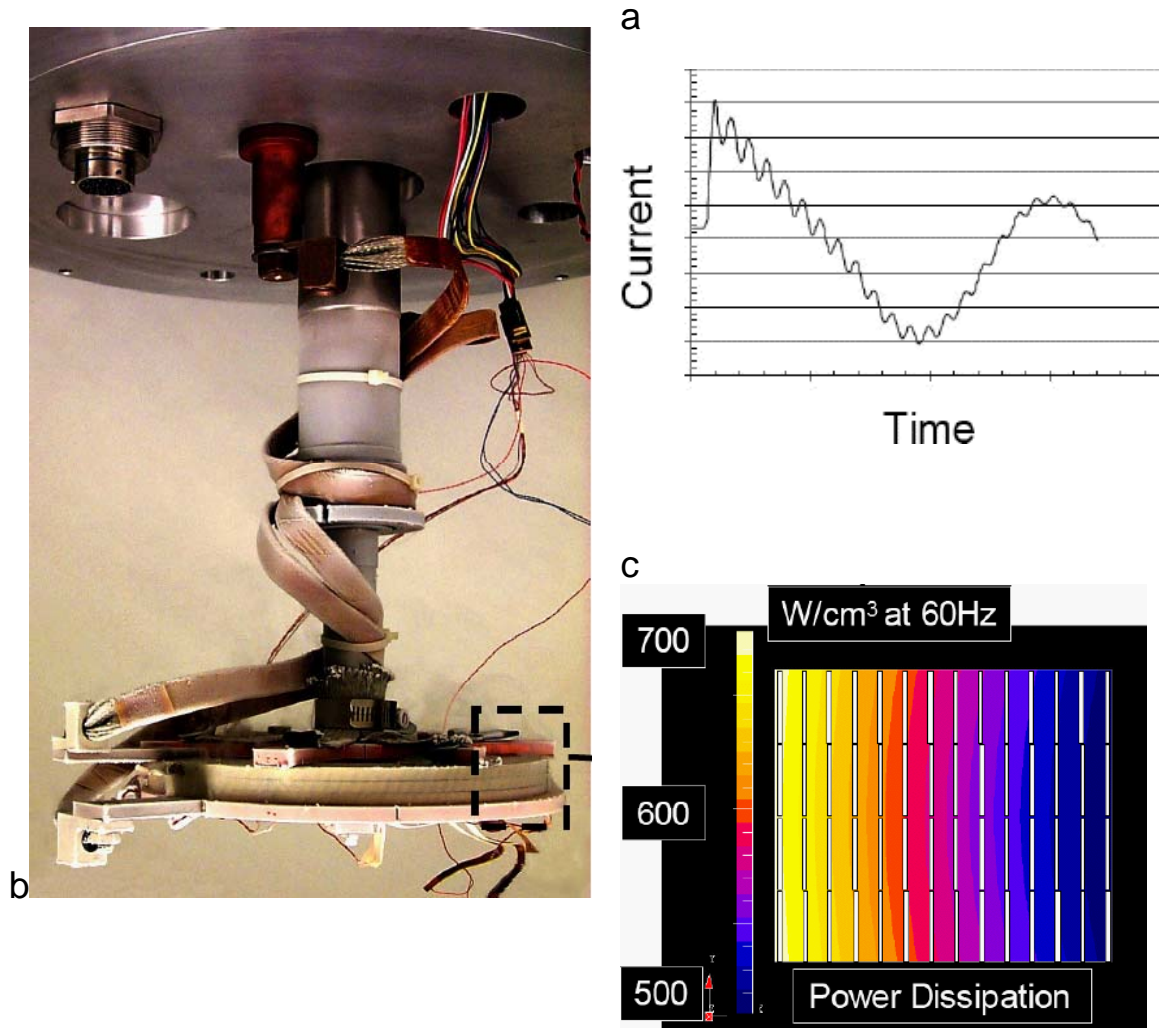


Fig. 117. Ac loss measurements in an HTS coil.

a: current as a function of time after a fault; b: experimental apparatus supporting a pancake coil, one edge of which is in the black dashed box at right; c: calculation of ac losses as a function of location in the winding pack.

In the final CRADA task, LANL is working with GE and making steady state analyses of the rotor cooling and baseline refrigeration system. LANL and GE have been exchanging models and reviewing the results. LANL is currently working with GE on parameters for a transient model being developed at LANL. Thus LANL is providing a capability that a refrigeration system vendor typically does not have. LANL is also providing information about thermal stresses and times and costs associated with startup and shutdown operations.

To summarize this work, the LANL tasks serve to augment the HTS generator program leading to cost reduction using 2nd generation wire and in production units. Testing of new samples that evaluate alternative materials and operational effects serve to enhance long-term vacuum maintenance and reduce refrigeration cost. The development of a more efficient cooling system using heat pipe technology also reduces refrigeration cost. Bench testing and fabrication of a heat pipe design have been completed, and the rotating tests are planned in the near future. The ac losses are being characterized to improve the thermal design margin. Modeling of the test coil has been completed, and the experimental confirmation is set to begin. LANL provided expertise in thermal modeling of the system. Modeling of the steady state is complete, and a transient model is in progress.

3. Fiscal Year 2005 Publications

3.1. Journal Articles Published

- Rare earth ion size effects and enhanced critical current densities in $\text{Y}_{2/3}\text{Sm}_{1/3}\text{Ba}_2\text{Cu}_3\text{O}_{7-x}$ coated conductors
J.L. MacManus-Driscoll, S.R. Foltyn, B. Maiorov, Q.X. Jia, A. Serquis, L. Civale, Y. Lin, M.E. Hawley, M.P. Maley
Applied Physics Letters 86, 3, 032505 (Jan 17 2005)
- Effects of Eu interfacial mobility on the growth of epitaxial $\text{EuBa}_2\text{Cu}_3\text{O}_{7-d}$ films
H. Wang, X.Z. Liao, H.F. Xu, X. Zhang, Y. Lin, S.R. Foltyn, P.N. Arendt, J.L. MacManus-Driscoll, Y.T. Zhu, Q.X. Jia
Applied Physics Letters 86, 10, 101912-1-3 (7 March 2005)
- Effect of the misalignment between the applied and internal magnetic fields on the critical currents of “tilted coated conductors”
B. Maiorov, B.J. Gibbons, S. Kreiskott, V. Matias, T.G. Holesinger, L. Civale
Applied Physics Letters 86, 13, 1-3 (Mar 28 2005)
- The effect of growth rates on the microstructures of $\text{EuBa}_2\text{Cu}_3\text{O}_{7-x}$ films on SrTiO_3 substrates
Y. Lin, H. Wang, M.E. Hawley, S.R. Foltyn, Q.X. Jia
Applied Physics Letters 86, 19, 192508-1-3 (9 May 2005)
- Magneto-optical evidence for a gapped Fermi surface in under doped $\text{YBa}_2\text{Cu}_3\text{O}_{6x}$
B.A. Maiorov, E.J. Osquiguill, S.C. Lee, M. Sullivan, G.R. Ruchti, S.M. Palmer, B.S. Anlage
Physical Review Letters: 93, 13, 137002/1-4 (2005)
- Spectroscopy of magnetic excitations in magnetic superconductors using vortex motion
L.N. Bulaevskii, M. Hruska, M.P. Maley
Physical Review Letters: 95, 20, 207002/1-4 (11 Nov 2005)
- Doping-dependent nonlinear Meissner effect and spontaneous currents in high- T_c superconductors
B.A. Maiorov, E.J. Osquiguill, S.C. Lee, M. Sullivan, G.R. Ruchti, S.M. Palmer, B.S. Anlage
Physical Review B: 71, 1, 014504 (2005)
- Improving flux pinning in $\text{YBa}_2\text{Cu}_3\text{O}_7$ coated conductors by changing the buffer layer deposition conditions
B. Maiorov, H. Wang, P.N. Arendt, S.R. Foltyn, and L. Civale
Ceramic Transactions 160, 3-13 (2005)
- Finite-Element Method Modeling of Superconductors from 2-D to 3-D
F. Grilli, S. Stravrev, Y. LeFloch, M. Costa, E. Vinot, I. Klustch, G. Meunier, P. Taxador, B. Dutoit
IEEE Transactions on Applied Superconductivity 15, 1, 17-25 (2005)
- Phase shifts of parallel currents in a single-layer model of superconducting cables
F. Gomory, L. Frolek, J. Souc, F. Grilli
IEEE Trans. Applied Superconductivity: 15, 2, Part II, 1779-82 (June 2005)

- 3-D finite element simulations of strip lines in a YBCO/Au fault current limiter
J. Duron, L. Antognazza, M. Decroux, F. Grilli, S. Stravrev, B. Dutoit, O. Fischer
 IEEE Trans. Applied Superconductivity: 15, 2, Part II, 1998-2002 (June 2005)
- Analysis of magnetic field and geometry effects for the design of HTS devices for AC power applications
F. Grilli, L. Martini, S. Stravrev, B. Dutoit, R. Brambilla
 IEEE Trans. Applied Superconductivity: 15, 2, Part II, 2074-7 (June 2005)
- AC losses in a high temperature-superconducting generator
K. Sivasubramaniam, X.R. Huang, D. Ryan, K. Weeber, J.W. Bray, E.T. Laskaris, L. Tomaino, J.M. Fogarty, S. Ashworth
 IEEE Trans. Applied Superconductivity: 15, 2, Part II, 2162-5 (June 2005)
- A shell model for the filament structure of Bi-2223 conductors
T.G. Holesinger, J.A. Kennison, S. Liao, Y. Yuan, J. Jiang, X.Y. Cai, E.E. Hellstrom, D.C. Larbalestier, R.A. Bauceanu, V.A. Maroni
 IEEE Trans. Applied Superconductivity: 15, 2, Part III, 2514-17 (June 2005)
- Long term anneal study and composition variation for reducing residual $\text{Bi}_2\text{Sr}_2\text{CaCu}_2\text{O}_x$ (2212) and $(\text{Bi, Pb})_2\text{SrCa}_2\text{Cu}_3\text{O}_x$ (2223) wires
J. Jiang, X.Y. Cai, Y. Yuan, A.A. Polyanskii, E.E. Hellstrom, D.C. Larbalestier, V.A. Maroni, T.G. Holesinger, Y. Huang
 IEEE Trans. Applied Superconductivity: 15, 2, Part III, 2526-9 (June 2005)
- Temperature and magnetic field dependence of critical currents in YBCO coated conductors with processing-induced variations in pinning properties
A.A. Gapud, R. Feenstra, D.K. Christen, J.R. Thompson, T.G. Holesinger
 IEEE Trans. Applied Superconductivity: 15, 2, Part III, 2578-81 (June 2005)
- Influence of tilted geometries on critical current superconducting thin films
B. Maiorov, B.J. Gibbons, S. Kreiskott, V. Matias, Q.X. Jia, T.G. Holesinger, L. Civale
 IEEE Trans. Applied Superconductivity: 15, 2, Part III, 2582-5 (June 2005)
- Second generation HTS wire based on RABiTS substrates and MOD YBCO
U. Schoop, M.W. Rupich, C. Thieme, D.T Verbelyi, W. Zhang, X. Li, T. Kodenkandath, N Nguyen, E Siegal, L. Civale
 IEEE Trans. Applied Superconductivity: 15, 2, Part III, 2611-16 (June 2005)
- Synthesis and characterization of Cu-doped SrTiO_3 powders and sol-gel processed buffer layers on IBAD MgO templates
A. Ayala, T.G. Holesinger, P.G. Clem, V. Matias, Q.X. Jia, H. Wang, S.R. Foltyn, B. Gibbons
 IEEE Trans. Applied Superconductivity: 15, 2, Part III, 2703-6 (June 2005)
- Comparative study of $\text{REBa}_2\text{Cu}_3\text{O}_7$ films for coated conductors
Q.X. Jia, B. Maiorov, H. Wang, Y. Lin, S.R. Foltyn, L. Civale, J.L. MacManus-Driscoll
 IEEE Trans. Applied Superconductivity: 15, 2, Part III, 2723-6 (June 2005)
- Continuous fabrication of IBAD-MgO based coated conductors
V. Matias, B.J. Gibbons, A.T. Findikoglu, P.C. Dowden, J. Sullard, J.Y. Coulter
 IEEE Trans. Applied Superconductivity: 15, 2, Part III, 2735-8 (June 2005)

- J_c-H crossover in YBCO thick films and Bi2223/Ag tapes with columnar defects
Q. Li, M. Suenaga, S.R. Foltyn, H. Wang
 IEEE Trans. Applied Superconductivity: 15, 2, Part III, 2787-2789 (June 2005)
- Critical currents I_c (77 K) > 350 A/cm-width achieved in ex situ YBCO coated conductors using a faster conversion process
R. Feenstra, A.A. Gupad, F.A. List, E.D. Specht, D.K. Christen, T.G. Holesinger, D. M. Feldmann
 IEEE Trans. Applied Superconductivity: 15, 2, Part III, 2803-7 (June 2005)
- Identification of intrinsic ab-plane pinning in YBa₂Cu₃O₇ thin films and coated conductors
L. Civale, B. Maiorov, J.L. MacManus-Driscoll, H. Wang, T.G. Holesinger, S.R. Foltyn, A. Serquis, P.N. Arendt
 IEEE Trans. Applied Superconductivity: 15, 2, Part III, 2808-11 (June 2005)
- Optimization of critical currents in MgB₂ wires and coils
A. Serquis, L. Civale, D.L. Hammon, G. Sarrano, V.F. Nesterenko
 IEEE Trans. Applied Superconductivity: 15, 2, Part III, 3188-91 (June 2005)
- Microwave properties of MgB₂ thin films grown by reactive evaporation
H.H. Moeckly, K.E. Kihlstrom, A.T. Findikoglu, D.E. Oates
 IEEE Trans. Applied Superconductivity: 15, 2, Part III, 3308-12 (June 2005)
- Dynamic field mapping for obtaining the current distribution in high-temperature superconducting tapes
B. Dutoit, J. Duron, S. Stravrev, F. Grilli
 IEEE Trans. Applied Superconductivity: 15, 2, Part III 3644-7 (June 2005)
- Optimizing SrTiO₃ films on textured Ni substrates using chemical solution deposition
M.P. Siegal, P.G. Clem, J.T. Dawley, J. Richardson, D.L. Overmyer, T.G. Holesinger
 J. Materials Research: 20, 4, 910-21 (April 2005)
- Liquid mediated growth and the bimodal microstructure of YBa₂Cu₃O_{7-d} films made by the ex situ conversion of physical vapor deposited BaF₂ precursors
T.G. Holesinger, P.N. Arendt, R. Feenstra, A.A. Gapud, E.D. Specht, D.M. Feldmann, D.C. Larbalestier
 J. Materials Research: 20, 5, 1216-33 (May 2005)
- Comparative study of microstructural properties for YBa₂Cu₃O₇ films on single-crystal and Ni-based metal substrates
Y. Lin, H. Wang, B. Maiorov, M.E. Hawley, C.J. Wetteland, P.N. Arendt, S.R. Foltyn, L. Civale, Q.X Jia
 J. Materials Research: 20, 8, 2055-2060 (Aug 2005)
- Crystallographic orientation dependence of radiation damage in Ar⁺ YSZ and MgO single crystals
I.O. Usov, P.N. Arendt, J.R. Groves, L. Stan, R.F. DePaula
 Nuclear Instruments and Methods in Physics Research B, 240, 3, 661-665 (2005)

Progress in scale-up of second-generation high-temperature superconductors at SuperPower Inc

Y.Y. Xie, A. Knoll, Y. Chen, Y. Li, X. Xiong, Y. Qiao, P. Hour, J. Reeves, T. Salaam, K. Lenses, L. Civale
Physica C 426-431, 849-857 (2005)

Thickness effects of SrTiO₃ buffer layers on superconducting properties of YBa₂Cu₃O_{7-d} coated conductors

H. Wang, S.R. Foltyn, P.N. Arendt, Q.X. Jia, Y. Li, X. Zhang
Physica C 435, 43-49 (2005)

3.2. Journal Articles Submitted for Publication

Grain boundary critical currents in coated conductors with non-correlating YBa₂Cu₃O₇ and substrate grain boundary networks

A. Palau, T. Puig, X. Obradors, Spain; R. Feenstra, A.A. Gapud, E.D. Specht, ORNL; D.M. Feldmann, U. WI; T.G. Holesinger, LANL
Submitted to Applied Physics Letters

High critical current densities in YBa₂Cu₃O_{7-x} films grown at high rates by hybrid liquid phase epitaxy

J.L. Driscoll, S.R. Foltyn, L. Civale, B.A. Maierov, H. Wang, Q.X. Jia, LANL;
J.E. Evetts, A. Kursumovic, Cambridge U
Submitted to Applied Physics Letters

Overcoming the barrier to 1000 A/cm-width superconducting coating

S.R. Foltyn, H. Wang, L. Civale, Q.X. Jia, P.N. Arendt, B Maierov, J.L. MacManus-Driscoll, Y. Li, M.P. Maley
Submitted to Applied Physics Letters

Epitaxial solution deposition of YBa₂Cu₃O_{7-d} coated conductors

P.G. Clem, J.T. Dawley, M.P. Siegal, D.L. Overmyer, J.J. Richardson, J.A. Voigt, Sandia Nat. Lab.; T.G. Holesinger
Submitted to Applied Physics Letters

Photobleaching in GdBa₂Cu₃O_{7-d} in a simulation Raman and electrical-transport experiment

S. Bahrs, A.R. Goni, C. Thomsen, TU Berlin; B.A. Maierov, LANL; G. Nieva, A. Fainstein, CAB-CNEA
Submitted to Physical Review B

Long-range order of vortex lattices pinned by point defects in layered superconductors

Jose P. Rodriguez
Submitted to Physical Review B

Collective pinning of imperfect vortex lattices by material line defects in extreme type-II superconductors

J.P. Rodriguez and M.P. Maley
Submitted to Physical Review B

- Evidence for extensive grain boundary meander and overgrowth of substrate grain boundaries in high critical current ex-situ $\text{YBa}_2\text{Cu}_3\text{O}_7$ coated conductors
D.M. Feldmann, D.C. Larbalestier, Univ. WI; T.G. Holesinger, LANL, R. Feenstra, A.A. Gapud, E.D. Specht, ORNL
 Submitted to Journal of Materials Research
- Comparison of different routes for improving vortex pinning in $\text{YBa}_2\text{Cu}_3\text{O}_7$ thin films and coated conductors
 B.A. Maiorov, L. Civale, H. Wang, S.R. Foltyn, Q.X. Jia, J.L. Driscoll,
 Submitted to Advances in Cryogenic Engineering
- Dual ion assist beam deposition of magnesium oxide for coated conductors
 J.R. Groves, P.N. Arendt, T.G. Holesinger, S.R. Foltyn, R.F. DePaula, L. Stan, I.O. Usov, LANL and *R.H. Hammond, Stanford U*
 Submitted to Advances in Cryogenic Engineering
- Comparison of different routes for improving vortex pinning in $\text{YBa}_2\text{Cu}_3\text{O}_7$ thin films and coated conductors
 B.A. Maiorov, H. Wang, S.R. Foltyn, P.N. Arendt, L. Civale, Q.X. Jia, J.L. Driscoll
 Submitted to Advances in Cryogenic Engineering
- Annealing of radiation damage in (110) MgO single crystals implanted with Ar^+ ions
 I.O. Usov, P.N. Arendt, J.R. Groves, L. Stan, R.F. DePaula
 Submitted to Nuclear Instruments and Methods in Physics Research B
- Comparison of AC losses of BSCCO and YBCO conductors by means of numerical analysis.
S. Stavrev, B. Dutoit, Switzerland; F. Grilli and S. Ashworth
 Submitted to Superconductor Science and Technology
- Technique for studying overcurrent behavior in YBCO coated conductors using a localized magnetic field
 J.Y. Coulter, S.P. Ashworth, P.C. Dowden and J.O. Willis
 Submitted to 2005 Spring MRS Mtg. San Francisco, CA; 3/28-31/05
- Influence of the substrate temperature on the texture of MgO films grown by ion beam assisted deposition
 L. Stan, P.N. Arendt, R.F. DePaula, I.O. Usov, J.R. Groves
 Submitted to 2005 MRS Mtg. Symposium C Proceedings, San Francisco CA
- Effects of structural microdomains on the vortex correlation length in a-axis oriented $\text{EuBa}_2\text{Cu}_3\text{O}_7$ thin films
E.M. Gonzalez, Z. Sefriouib, Madrid, B.A. Maiorov, LANL, E. J. Osquiguil, CAB-CNEA, J. Santamaria, J.L. Vicent, Madrid
 Submitted to Journal of Physics and Chemistry of Solids
- Recent advances in superconductivity-materials synthesis, multi-scale characterization and functionally layered composite conductors
 T.G. Holesinger, LANL; *T. Izumi, SRI-ISTEC; J.L. MacManus-Driscoll, Cambridge; D. Miller, ANL, W. Wong-Ng, NIST*
 Summary submitted to Materials Research Bulletin

3.3. Other Publications and Conference Abstracts

Critical current anisotropy in nano-structured superconductors

J.H. Durrell, N.A. Rutter, J.E. Evetts, M.G. Blamire, J.L. McManus- Driscoll,
Cambridge; B.A. Maiorov, H. Wang, S.R. Foltyn, and L. Civale

Abstract submitted to MRS 2005 Spring Mtg., San Francisco, CA 3/28/-4/1/05

Evolution of biaxial texture during ion-beam assisted deposition of MgO

V. Matias, A.T. Findikoglu, and T.G. Holesinger

Abstract submitted to MRS 2005 Spring Mtg., San Francisco, CA 3/28/-4/1/05

Continuous preparation of pulsed laser deposited YBCO on IBAD-MgO for coated conductor applications

B.J. Gibbons, P.C. Dowden, and V. Matias

Abstract submitted to MRS Spring Mtg. 2005, San Francisco, CA, 3/28-4/1/05

YBCO Coated conductor current stabilizer V-I characteristics and thermal properties

J.Y. Coulter, P. Dowden, S. Ashworth, J.O. Willis, L. Civale, B.J. Gibbons, R. Edwards, K. Rau

Abstract submitted to MRS 2005 Spring Mtg., San Francisco, CA 3/28/-4/1/05

Limiting factors for high performance second-generation coated conductors

Q.X. Jia

Abstract for talk at State Univ. of New York, Buffalo NY 4/8/05

Epitaxial growth of both simple and complex metal-oxide films by polymer-assisted deposition

Q.X. Jia, Y. Lin, H. Wang, S.R. Foltyn

Abstract submitted to American Ceramic Society 107th Annual Mtg. and 1st Int. CICMT; Baltimore, MD; April 10-13, 2005

IBAD texturing or templates for epitaxial film growth

V. Matias and A.T. Findikoglu

Abstract submitted to 16th American Conf. on Crystal Growth and Epitaxy, Big Sky, Montana, July 10-15, 2005

Recent advances in understanding the development of J_c in Ag-sheathed Bi-22223 wire

E. Hellstrom, J. Jiang, X. Cai, A. Polyanskii, D. Abraimov, Y. Yuan, S. Liao, D. Larbalestier, U. WI; A. Malozemoff, Y. Huang, AMSC; T.G. Holesinger, LANL; V. Maroni, ANL

Abstract for MEM 05 Conf., Tokyo, Japan, July 2005

High temperature superconductors: materials science successes and challenges

J.O. Willis

Abstract submitted to 7th Giambiagi Winter School, Buenos Aires, Argentina, July 25-29, 2005

Magnetic determination of the field-dependence of critical current in coated conductors

J.R. Mantei, L. Civale, J.O. Willis, B.A. Maiorov

Abstract submitted to LANL Student Symposium 2005, Aug. 3, 2005

- Dual ion assist beam deposition of magnesium oxide for coated conductors
J.R. Groves, P.N. Arendt, R.F. DePaula, L. Stan, and I.O. Usov
Abstract submitted to CEC-ICMC 2005; Keystone, CO Aug. 29- Sept.2, 2005
- High rate deposition of YBCO films by Co-Evaporation for HTS coated conductors
J. Storer, C.J. Sheehan, and D.W. Reagor
Abstract submitted to CEC-ICMC 2005; Keystone, CO Aug. 29- Sept.2, 2005
- Copper Stabilized YBCO Coated Conductor Behavior in Over Current Conditions
J.Y. Coulter, J.O. Willis, B.J. Gibbons, V. Matias, P.C. Dowden
Abstract submitted to CEC-ICMC 2005; Keystone, CO Aug. 29- Sept.2, 2005
- X-Ray diffraction and compositional measurements on secondary phases found in melt-processed Bi-2212 tapes
J.A. Kennison and T.G. Holesinger
Abstract submitted to CEC-ICMC 2005; Keystone, CO Aug. 29- Sept.2, 2005
- Optimization of critical currents on MgB₂ wires and tapes
G. Serrano, A.C. Serquis, B.A. Maiorov, L. Civale, LANL; *M.T. Malachevsky, C. Ayala, G. Bridoux, CEB, Argentina*
Abstract submitted to CEC-ICMC 2005; Keystone, CO Aug. 29- Sept.2, 2005
- Microstructural development in high J_c (I_c) YBa₂Cu₃O_{7-x} coated conductors based on ex-situ YBCO conversion process
T.G. Holesinger, L. Civale, J.Y. Coulter; *W. Zhang and X. Li, AMSC*
Abstract submitted to CEC-ICMC 2005; Keystone, CO Aug. 29- Sept.2, 2005
- The effect of alumina additions on the processing of Bi-2212 conductors
T.G. Holesinger, J.A. Kennison, LANL; *K.R. Marken, H. Miao, M. Meinesz, S. Hong, Oxford Scientific Instruments*
Abstract submitted to CEC-ICMC 2005; Keystone, CO Aug. 29- Sept.2, 2005
- High rate deposition of YBCO films by Co-evaporation for HTS coated conductors
J. Storer, C. Sheehan, I. Usov, D. Reagor, LANL; *J. Huh, G. Koster, R.H. Hammond, M.R. Beasley, Stanford U*
Abstract submitted to CEC-ICMC 2005; Keystone, CO Aug. 29- Sept.2, 2005
- Radiation damage anisotropy in MgO and YSZ single crystals
I.O. Usov, P.N. Arendt, T.G. Holesinger, R.J. Groves, L. Stan, and R.F. DePaula
Abstract submitted to 13th Int. Conf. on Radiation Effects in Insulators (REI 2005), Santa Fe, NM, Aug. 31 - Sept 2, 2005.
- Continuous Fabricated IBAD-Textured Coated conductors
V. Matias, B.J. Gibbons, P. Dowden, J. Rowley, A. Findikoglu, J. Coulter and S. Ashworth
Abstract submitted to 7th European Conf. on Appl. Supercond. (EUCAS) Vienna, Austria, Sept. 11-15, 2005
- Losses in Bi-2223/Ag Tape at simultaneous action of AC transport and AC magnetic field shifted in phase
J. Souc, M. Vojenciak, B. Klinecok, F. Gomory, Inst. of Electrical Engineering; J. Ceballos, Indst. Engineering Faculty; E. Pardo, Spain; F. Grilli, LANL
Abstract submitted to 7th European Conf. on Appl. Supercond. (EUCAS) Vienna, Austria, Sept. 11-15, 2005

- Finite-Element modeling of superconductors in over-critical regime with temperature dependent resistivity
J. Duron, S. Stravrev, B. Dutoit, Switzerland; F. Grilli, LANL; L. Antognazza, M. Decroux, O. Fischer, Switzerland
 Abstract submitted to 7th European Conf. on Appl. Supercond. (EUCAS) Vienna, Austria, Sept. 11-15, 2005
- Finite-Element analysis of the AC loss performance of BSCCO and YBCO conductors
S. Stravrev, Bertrand Dutoit- Swiss Fed. Institute of Tech.; F. Grilli and S. Ashworth, LANL
 Abstract submitted to 7th European Conf. on Appl. Supercond. (EUCAS) Vienna, Austria, Sept. 11-15, 2005
- Flux pinning improvement in coated conductors: how much further can we go?
L. Civale, B.A. Maierov, H. Wang, S.R. Foltyn, J.L. MacManus-Driscoll, T.G. Holesinger, Q.X. Jia, P.N. Arendt
 Abstract submitted to PACRIM6 Maui, Hawaii, Sept. 11-17, 2005
- TEM studies of interfacial microstructures in $\text{YBa}_2\text{Cu}_3\text{O}_7$ coated conductors
T.G. Holesinger, P.N. Arendt, J.R. Groves, LANL; R. Feenstra, A.A. Gapud, E.D. Specht, ORNL; D.T. Verebelyi, W. Zhang, X. Li, and M. Rupich, AMSC
 Abstract submitted to PACRIM6 Maui, Hawaii, Sept. 11-17, 2005
- Continuous preparation of pulsed laser deposited YBCO on IBAD-MgO for coated conductor applications
B.J. Gibbons, J.G. Storer, A.T. Findikoglu, P.C. Dowden, C.J. Sheehan, E.J. Rowley, J.Y. Coulter, V. Matias
 Abstract submitted to PACRIM6 Maui, Hawaii, Sept. 11-17, 2005
- Microstructural study of thick superconducting films with high critical current density
Q.X. Jia, H. Wang, Y. Li, S.R. Foltyn, Y. Lin, L. Civale, and P.N. Arendt
 Abstract submitted to PACRIM6 Maui, Hawaii, Sept. 11-17, 2005
- Pulsed laser deposition equipment for coated-conductor applications
J.A. Greer, M. Paradise, B. Howard, PVD Products; B.J. Gibbons and V. Matias
 Abstract submitted to 8th International Conf. On Laser Ablation, Banff, Canada, Sept. 11-16, 2005.
- Continuously fabricated IBAD-textured coated conductors
V. Matias, B.J. Gibbons, P.C. Dowden, J. Rowley, A.T. Findikoglu, J.Y. Coulter, F. Grilli, and S.P. Ashworth
 Abstract submitted to ISS 2005, Tsukuba, Japan, Oct. 24-27, 2005
- Recent progress in vortex pinning enhancement by microstructural engineering of coated conductors
L. Civale, B.A. Maierov, H. Wang, S.R. Foltyn, and T.G. Holesinger
 Abstract submitted to ISS 2005 Conf. Tsukuba, Japan, Oct. 24-27, 2005
- Damage recovery of Mg implanted GaN during rapid thermal annealing
I.O. Usov, T.G. Holesinger, P.N. Arendt
 Abstract submitted to MRS 2005 Fall Mtg. Boston, MA, Nov. 28 - Dec 2, 2005

4. Patent and License Activity (April 1988 to September 2005)

4a. Invention Disclosures and Patent Applications

| Designation | Date | Subject | Submitted by |
|----------------------------------|------------------------------------|---|--|
| DOE 94,720 | 7/13/00 | Apparatus for Heating a Moving Tape | S. R. Foltyn, P.C. Dowden |
| DOE S-97,795 S.N. 10/209,391 | Filed 7/31/02 | Multilayer Composites and Manufacture of Same | T.G. Holesinger, Q.X. Jia |
| DOE S-99.947 S.N. 10/456,639 | Disclosed 9/10/02 Filed 6/5/03 | Processing of High Density MgB ₂ Wires by Hot Isostatic Pressing | Y.T. Zhu, A. Serquis, D. Hammon, L. Civale, X.Z. Liao, F.M. Mueller, D.E. Peterson, V. Nesterenko, Y. Gu |
| DOE S-99.952 S.N. 10/624,350 | Disclosed 9/16/02 Filed 7/21/03 | Use of High Current Density Electropolishing for the Preparation of Very Smooth Substrate Tapes for Coated Conductor Applications | S. Kreiskott, V. Matias, P.N. Arendt. S.R. Foltyn |
| DOE S-100,556 S.N. 60/483,146 | Filed 6/26/03 | Underground Radio | David Reagor, Jose Vasquez-Dominquez |
| DOE S-100,564 S.N. 10/624,855 | Filed 7/21/03 | Buffer Layer for Thin Film Structures | Stephen Foltyn, Quanxi Jia, Paul Arendt, Haiyan Wang |
| DOE S-100,600 | Disclosed 4/8/03 | Magnetic Infrasound Sensor | Frederick Mueller, Lawrence Bronisz, Holger Grube, David Nelson, Jonathon Mace |
| DOE S-100,631 S.N. 10/888,868 | Disclosed 8/03 Filed 7/8/04 | Polymer-assisted deposition of films | T.M. McCleskey, A.K. Burrell, Q.X. Jia, Y. Lin |
| DOE S-100,663 S.N. 10/925,479 | Disclosed 9/5/03 Filed 8/25/04 | Enhanced Pinning in Mixed RE-123 Films | Judith Driscoll Stephen Foltyn |
| DOE S-100,664 | Disclosed 9/5/03 | Balanced Inductance Current Limiter | Stephen Ashworth |
| DOE S-100,667 S.N. 10/900,639 | Disclosed 9/5/03 Filed 7/24/04 | Enhanced Pinning in YBCO Films with BaZrO ₃ Nanoparticles | Judith Driscoll Stephen Foltyn |
| DOE S-102,337 | Disclosed 2004 | Method for Improving the Critical Current Density of Thick YBCO Coatings | Stephen Foltyn, Quanxi Jia, Haiyan Wang |
| DOE S-102,368 | Disclosed 2004 | Superconducting Current Controller | Stephen P. Ashworth |
| DOE S-102,393 | Disclosed 2004 | Method For Improving Performance Of High-Temperature Superconductors in a Magnetic Field | Haiyan Wang, Boris Maiorov, Stephen R Foltyn, Leonardo Civale |
| DOE S-104,805 | Disclosed | Architecture for Coated | Stephen R. Foltyn, Paul N. |

| Designation | Date | Subject | Submitted by |
|--|--|---|--|
| S.N. 11/021,171 | 2004 Filed 12/23/04 | Conductors | Arendt, Haiyan Wang, Liliana Stan |
| DOE S-104,806 S.N. 11/02,1800 | Disclosed 2004 Filed 12/23/04 | High-Rate Buffer Layer for IBAD MgO Coated Conductors | Stephen R. Foltyn, Quanxi Jia, Paul N. Arendt |
| DOE S-104,919 | Disclosed 5/2/05 | Method for determining current densities using external magnetic field measurements | Frederick Mueller et. Al. |
| DOE S-104,949 S.N. 60/699,241 | Disclosed Filed 7/13/05 | Cubic metal oxide film buffers for IBAD MgO templates amenable for high rate reactive sputter deposition | Paul Arendt, et al. |

4b. Patents Granted

| Designation | Date | Subject | Issued to | Status |
|--|---|---|---|----------------------------------|
| DOE S-63,245 S.N. 07/041,950 US Pat.4,784,686 | Filed 04/24/87 Issued 11/15/88 | Synthesis of Ultrafine Powders by Microwave Heating | T.T. Meek H. Sheinberg R.D. Blake | Expired 05/15/00 |
| DOE S-68,033 S.N. 07/454,607 US Pat. 5,008,622 | Filed 12/21/89 Issued 04/16/91 | Superconductive Imaging Surface Magnetometer | W.C. Overton, Jr D. van Hulsteyn E.R. Flynn | Expired 10/16/98 |
| DOE S-68,041 S.N. 07/330,329 US Pat 5,006,672 | Filed 03/29/89 Issued 04/09/91 | Apparatus for Storing High Magnetic Fields Having Reduced Mechanical Forces and Reduced Magnetic Pollution | M.L. Prueitt F.M. Mueller J.L. Smith | Maint. Fee 3 paid 10/09/02 |
| DOE S-68,042 S.N. 07/276,188 US Pat 4,873,444 | Filed 11/23/88 Issued 10/10/89 | Detection of Surface Impurity Phases in HTS Using Thermally Stimulated Luminescence | D.W. Cooke M.S. Jahan | Expired 10/10/97 |
| DOE S-68,086 S.N. 07/311,998 US Pat 4,992,696 | Filed 02/17/89 Issued 02/12/91 | Apparatus Having Reduced Mechanical Forces for Supporting High Magnetic Fields | M.L. Prueitt F.M. Mueller J.L. Smith | Maint. Fee 3 paid 08/12/02 |
| DOE S-68,098 S.N. 07/324,264 US Pat 5,015,952 | Filed 03/14/89 Issued 05/14/91 | Apparatus for Charac- terizing Conductivity of Materials by Measuring the Effect of Induced Shielding Currents Therein | J.D. Doss | Expired 05/14/99 |
| DOE S-71,082 S.N. 07/671,231 | Filed 03/19/91 | Process for Producing Clad Superconducting | R.B. Cass K.C. Ott | Expired 10/07/99 |

| Designation | Date | Subject | Issued to | Status |
|--|---|--|--|---------------------------------|
| US Pat 5,102,863 | Issued 04/07/92 | Materials | D.E. Peterson | |
| DOE S-71,084 S.N. 07/670,111 US Pat 5,134,360 | Filed 03/15/91 Issued 07/28/92 | Apparatus and Method for Critical Current Measurements | J.A. Martin R.C. Dye | Expired 01/28/00 |
| DOE S-72,816 S.N. 07/690,725 US Pat 5,268,646 | Filed 04/24/91 Issued 12/07/93 | Apparatus & Method for Characterizing Con- ductivity of Materials | J.D. Doss | Maint. Fee 2 due 06/07/05 |
| DOE S-72,851 S.N. 07/860,337 US Pat. 5,238,913 | Filed 03/30/92 Issued 08/24/93 | Superconducting Micro- circuitry by the Micro- lithographic Patterning of Superconducting Compounds and Related Materials | N.V. Coppa | Expired 08/24/01 |
| DOE S-72,861 S.N. 813,726 US Pat 5,262,394 | Filed 12/27/91 Issued 11/16/93 | Superconductive Compositions Including Cerium Oxide Layer | X.D. Wu R. Muenchausen | Maint. Fee due 05/16/05 |
| DOE S-72,880 S.N. 07/774,748 US Pat 5,278,138 | Filed 10/11/91 Issued 01/11/94 | Aerosol Chemical Vapor Deposition of Metal Oxide Films | K.C. Ott T.T. Kodas | Maint. Fee due 07/11/05 |
| DOE S-72,898 S.N. 814,355 US Pat 5,252,551 | Filed 12/27/91 Issued 10/12/93 | Superconductive Articles | X.D. Wu, R.E. Muenchausen | Maint. Fee due 04/12/05 |
| DOE S-72,899 S.N. 813,727 US Pat 5,270,294 | Filed 12/27/91 Issued 12/14/93 | Free-Standing Superconductive Articles | X.D. Wu, R.E. Muenchausen | Maint. Fee due 06/14/05 |
| DOE S-75,023 S.N. 08/419,485 US. Pat 5,554,224 | Filed 03/31/94 Issued 09/10/96 | Substrate Heater for Thin Film Deposition | S.R. Foltyn | Maint. Fee due 03/10/04 |
| DOE S-75,081 S.N. 08/067,911 US Pat 5,300,486 | Filed 05/27/93 Issued 04/06/94 | Synthesis of BiPbSrCaCuO Superconductor | W.L. Hults, K.A Kubat-Martin, K.V. Salazar, D.S. Phillips, D.E. Peterson | Maint. Fee due 10/05/05 |
| DOE S-78,394 S.N. 08/419,485 US Pat. 5,569,641 | Filed 04/10/95 Issued 10/29/96 | Preparation of Superconducting Bi- 2223 Wire | M.G. Smith J.O. Willis D.E. Peterson | Maint. Fee due 04/29/04 |
| DOE S-80,400 S.N. 08/168,331 US Pat 5,434,128 | Filed 12/17/93 Issued 07/18/95 | Superconducting Wire | D.A. Korzekwa J.F. Bingert D.E. Peterson H. Sheinberg | Maint. Fee due 01/18/07 |
| DOE S-82,620, S.N. 08/425,752 | Filed 04/19/95 | High Temperature | P.N. Arendt X.D. Wu | Maint. Fee 1 |

| Designation | Date | Subject | Issued to | Status |
|---|---|--|---|---------------------------------|
| US Pat. 5,872,080 | Issued 02/16/99 | Superconducting Thick Films | S.R. Foltyn | due 08/16/06 |
| DOE S-82,623 S.N. 08/608,069 US Pat. 5,958,842 | Filed 02/28/96 Issued 09/28/99 | Melt Processing of Superconductors Using Alumina | T.G. Holesinger | Maint. Fee 1 due 03/28/07 |
| DOE S-82,633 US Pat. 5,726,848 | Filed 05/8/96 Issued 3/10/98 | Fault Current Limiter and Alternating Current Circuit Breaker | H.J. Boenig | Maint. Fee due 09/10/05 |
| DOE S-84,942 S.N. 08/597,061 US Pat. 5,908,812 | Filed 02/05/96 Issued 06/01/99 | Structure for HTS Composite Conductors & Manufacture of Same | J.D. Cotton G.N. Riley | Maint. Fee due 12/01/06 |
| DOE S-84,965 S.N. 08/865,827 US Pat. 5,820,678 | Filed 09/23/96 Issued 10/13/98 | Solid Source MOCVD Delivery System | B.N. Hubert X.D. Wu | Maint. Fee due 04/13/06 |
| DOE S-89,600 S.N. 60/074,717 S.N. 09/249,476 US Pat. 6,195,870 | Filed 2/13/98 Filed 02/12/99 Issued 3/6/01 | Compressive Annealing of BSCCO-2223 Superconductive Tapes | Y.T. Zhu, P.S. Baldonado, J.F. Bingert, T.G. Holesinger, D.E. Peterson | Maint. Fee due 3/06/04 |
| DOE S-91,761 S.N. 60/213,111 S.N. 09/867,842 US Pat. 6,383,989 | Filed 6/21/00 Filed 5/29/01 Issued 5/7/02 | Architecture for High Critical Current Superconducting Thick Films | Q.X. Jia S.R. Foltyn T.G. Holesinger | |
| DOE S-89,624 S.N. 08/942,038 US Pat. 6,428,635 | Filed 10/1/97 Issued 8/6/02 | Substrates for Superconductors | L.G. Fritzemeier, E. Thompson, E. Siegel, C. Thieme, R.D. Cameron, J.L. Smith, W.L. Hulst | Maint. Fee due 8/6/05 |
| DOE S-89,678 S.N. 09/152,813 US Pat. 6,541,136 | Filed 9/14/98 Issued 4/1/03 | Superconducting Structure | C. Kwon, Q.X. Jia, and S.R. Foltyn | Maint. Fee due 10/1/06 |
| DOE S-89,679 S.N. 60/100,215 S.N. 09/787,224 US Pat. 6,602,588 | Filed 9/14/98 Filed 3/14/01 Issued 8/5/03 | Superconducting Structure Including Mixed Rare-Earth Barium Copper Oxide Compositions | C. Kwon, Q.X. Jia, S.R. Foltyn, J.L. Smith, W.L. Hulst, E.J. Peterson | Maint. Fee due 2/5/07 |
| DOE S-91,736 S.N. 60/138,326 S.N. 09/615,640 US Pat. 6,451,742 | Filed 06/09/99 Filed 7/13/00 Issued 9/17/02 | High Temperature Superconducting Com- posite Conductor & Method for Manufac- turing the Same | T.G. Holesinger and J.F. Bingert | Maint. Fee due 9/17/05 |
| DOE S-91,748 | | Apparatus for | J. Y. Coulter | Maint. Fee |

| Designation | Date | Subject | Issued to | Status |
|---|--|--|--|------------------------|
| S.N. 60/143,781 S.N. 09/615,640 US Pat. 6,452,375 | Filed 7/13/99 Filed 7/13/00 Issued 9/17/02 | Measurement of Critical Current in Superconductive Tapes | R.F. DePaula | due 9/17/05 |
| DOE S-91,761 S.N. 60/213,111 S.N. 09/867,842 US Pat. 6,383,989 | Filed 6/21/00 Filed 5/29/01 Issued 5/7/01 | Architecture for High Critical Current Superconducting Thick Films | Q.X. Jia S.R. Foltyn T.G. Holesinger | Maint. Fee due 11/7/05 |
| DOE 94,732 S.N. 09/721,834 US Pat. 6,624,993 | Filed 11/22/00 Issued 9/23/03 | Adjustable Direct Current and Pulsed Fault Current Limiter | H.J. Boenig J.B. Schillig | Maint. Fee due 3/23/07 |
| DOE S-97,723 S.N. 10/113,476 US Pat. 6,624,122 | Filed 5/30/01 Issued 9/23/03 | High Critical Current Superconducting Tapes | T.G. Holesinger, Q.X. Jia S.R. Foltyn | Maint. Fee due 3/27/07 |
| DOE S-97,804 S.N. 10/096,774 US Pat. 6,511,943 | Filed 3/13/02 Issued 1/28/03 | Synthesis of Magnesium Diboride by Magnesium Vapor Infiltration | A. Serquis, Y.T. Zhu, F.M. Mueller, D.E. Peterson, X.Z. Liao | Maint. Fee due |
| DOE 94,734 S.N. 60/333,917 S.N. 10/113,475 US Pat. 6,716,545 | Filed 11/21/01 Filed 3/28/02 Issued 4/6/04 | High Temperature Superconducting Composite Conductors | T.G. Holesinger, S.R. Foltyn, P.N. Arendt, J.R. Groves, Q.X. Jia, A. Ayala | |
| DOE S-94,668 S.N. 60/170,968 S.N. 09/616,570 US Pat. 6,730,410 | Filed 7/14/00 Issued 5/4/04 | Surface control alloy substrates and methods of manufacture thereof | L.G. Fritzemeier, Q. Li, M.W. Rupich, E.D. Thompson, E.J. Siegel, C.L.H. Thieme, S. Annavarapu, P.N. Arendt, S.R. Foltyn | |
| DOE S-97,725 S.N. 10/113,476 US Pat. 6,756,139 | Filed 3/28/02 Issued 6/29/04 | Buffer Layer on Metal Alloy Substrates for Superconducting Tapes | Q.X. Jia, S.R. Foltyn, P.N. Arendt, J.R. Groves | |
| DOE S-97,787 S.N. 10/208,086 US Pat. 6,899,928 | Filed 7/29/02 Issued 5/31/05 | Dual Ion Beam Assisted Deposition of Biaxially Textured Template Layers | James Groves Paul N. Arendt, Robert H. Hammond | |
| DOE S-97,803 S.N. 10/161,132 US Pat. 6,800,321 | Filed 5/29/02 Issued 10/5/04 | Reduced AC Losses in HTS Coated Conductors | S.P. Ashworth | |
| DOE S-100,536 S.N. 10/624,348 US Pat. 6,884,527 | Filed 7/21/03 Issued 4/26/05 | Biaxially Textured Composite Substrates | James Groves, Paul Arendt, Stephen Foltyn | |

| Designation | Date | Subject | Issued to | Status |
|--|--|--|--|---------------|
| DOE S-100,550 S.N. 10/321,156 US Pat. 6,943,136 | Filed 12/17/02 Issued 9/13/05 | Superconducting Structure | Chuhee Kwon, Quanxi Jia, Stephen R. Foltyn | |
| DOE S-100,569 S.N. 10/359,808 US Pat. 6,931,741 | Filed 2/7/03 Issued 7/26/05 | Substrate Structure for Growth of Highly Oriented and/or Epitaxial Layers Thereon | Paul Arendt, Stephen Foltyn, James Groves, Quanxi Jia | |
| DOE S-100,586 S.N. 10/387,952 US Pat. 6,933,065 | Filed 3/13/03 Issued 8/23/05 | High Temperature Superconducting Thick Films | Paul N. Arendt, Stephen R. Foltyn, James R. Groves, Terry G. Holesinger, Quanxi Jia | |
| DOE S-99,943 S.N. 10/242,895 US Pat. 6,800,591 | Filed 9/11/02 Issued 10/5/04 | Buffer Layers on Metal Alloy Substrates for Superconducting Tapes | Q.X. Jia, S.R. Foltyn, P.N. Arendt, J.R. Groves | |

4c. Licenses Granted

| License Number | Dates | Subject | Issued to |
|---------------------------|---------------------------|---|--------------------------------|
| 89-41-0000-1 | 12/28/88 - 11/94 | Apparatus for Characterizing Conductivity of Materials by Measuring the Effect of Induced Shielding Currents Therein | Lakeshore Cryotronics |
| 99-C00510.1 | 11/11/98 | Superconductive Article including Cerium Oxide Layer | DuPont Superconductivity |
| 01-C01080.0 | 05/29/01 - - 12/17/03 | High Temperature Superconductor Material | IGC-SuperPower, LLC |
| 01-C01081.0 | 05/29/01 - - 12/17/03 | High Temperature Superconductor Material | IGC-SuperPower, LLC |
| 01-C01082.0 | 05/29/01 - - 12/17/03 | Fault Current Limiter and Alternating Current Circuit Breaker Device | IGC-SuperPower, LLC |
| 05-C01724 | In negotiation | Superconductivity Technology | IGC-SuperPower, LLC |

5. Agreements in Progress (8 Active, all types)

5a. CRADA Agreements - Active

| Organization | Topic | PI | Funding,\$K DOE | Funding,\$K Partner | Dates |
|-----------------------------------|--|-----------------------------------|-----------------------|------------------------|---|
| Oxford Superconducting Technology | Bi-2212 HTS Tapes | Smith Holesinger Holesinger | 290 55 700 | 290 100 730 | 11/93 -11/96 10/97–10/98 5/99-10/05 |
| American Superconductor Corp. | Bi-2223 Wire Development HTS Wire Technologies | Holesinger | 450 | 450 | 5/02-5/04 |
| | | Holesinger | 375 1800 | 300 1200 | 5/04-5-05 5/05-5/08 |
| General Electric | HTS Generator | Waynert Schmierer | 860 860 | 860 860 | 8/02-8/04 8/04-8/06 |
| IGC-SuperPower | Coated Conductors | Foltyn Balachandran | 700, LANL 500, ANL | 1300 | 1/00-1/03 |
| | | Foltyn Foltyn | 1700 2000 | 1700 2000 | 4/03-3/05 4/05-10/07 |

5b. Funds In / Funds Out Agreements – Active

| Organization | Topic | PI | Type | Value \$K | Dates |
|--|--|------------|----------|-----------|-------------|
| Long Electro-magnetics, Inc. | AC Losses in HTS Wires | Willis | Funds In | 30 | 5/04-2/05 |
| SCI Engineered Materials, Inc. | Bi2212 Round Wires for High Field Magnets | Holesinger | Funds-In | 100 | 10/04-10/06 |
| DARPA through Office of Naval Research | AC Losses in High Performance 2G HTS Wire | Ashworth | Funds-In | 150 | 10/04-9/07 |
| Office of Naval Research | Electromagnetic Propulsion and Magnetic Levitation | Peterson | Funds In | 600 | 08/05-9/06 |

5c. Other Collaborations - Active

| Organization | Topic | PI | Dates |
|--|---|---------------------------------------|-------------------------------------|
| ASC/ ANL/ ORNL/ U. Wisconsin/ (previously, NIST-Gaithersburg) | Bi-2223 Wire Development (Wire Development Group) (Primarily Coated Conductors) | J. Willis Holesinger Holesinger | 11/91-11/00 11/00-9/04 10/04- |
| ASC/ORNL/U. Wisconsin/ (previously, TCSUH, LBNL, MIT, WPAFB, EPRI) | Coated Conductor Development Group (now combined with WDG) | J. Willis Holesinger | 2/96-11/00 11/00-9/04 |
| Oak Ridge National Laboratory | HTS Information Exchange | D. Peterson | In Progress |

| | | | |
|------------------------------|--------------------------|-------------|-------------|
| Argonne National Laboratory | HTS Information Exchange | D. Peterson | In Progress |
| Sandia National Laboratories | HTS Information Exchange | D. Peterson | In Progress |
| Brookhaven National Lab. | HTS Information Exchange | D. Peterson | In Progress |

6. Completed Agreements

6a. CRADA Agreements - Completed

| Organization | Topic | PI | Funding,\$K DOE | Funding,\$K Partner | Dates |
|---------------------------------------|--|-----------|------------------------------|------------------------------|-------------------------------------|
| Lockheed Martin | Coil Development | Peterson | 330 | 210 | 7/93 - 7/96 |
| Plastronic, Inc. | Liquid Cryogen Free HTS Magnet System | Daugherty | 100 +33k funds in | 67 | 6/95 - 5/96 |
| The BOC Group, Inc. | Superconducting Coated Materials | Peterson | 70 | 70 | 2/23/96-11/22/96 |
| EURUS Technologies, Inc. | Development of HTS Current Leads & Solders | Peterson | 80 | 140 | 2/6/96-2/5/97 |
| Eriez Magnetics | HTS Magnetic Separation | Daugherty | 70 | 52 | 4/2/96-4/1/97 |
| Lockheed Martin | HTS Current Limiter | Peterson | 400 | 400 | 11/95-10/97 |
| Lockheed Martin | Bridge-Type Fault Current Limiter | Boenig | 700 | 1400 | 11/95-9/98 |
| General Atomics (assumed LM activity) | Bridge-Type Fault Current Limiter | Peterson | Remainder of 700 from above | Remainder of 1400 from above | 9/98-5/99, 5/99-11/99 |
| Astronautics Corp. of America | Active HTS Magnetic Refrigerator | Peterson | 200 | 200 | 4/98-7/00 |
| ABB Power T&D Co., Inc. | HTS Transformer | Maley | 95 | 70 | 7/99-7/00 |
| 3M Corporation | Coated Conductors | Peterson | 960 720 400 | 1375 720 150 | 3/97-3/99 3/99-5/00 5/00-1/02 |
| DuPont | HGMS Magnetic Separation | Waynert | 120 LANL 300 FI Dupont | 200 | 6/02-6/04 |
| Hyper Tech Research, Inc. | MgB ₂ Wire Development | Mueller | 400 | 400 | 9/02-9/04 |

6b. Funds In / Funds Out Agreements - Completed

| Organization | Topic | PI | Type | Value \$K | Dates |
|-----------------------------------|---|--------------------|-------------------------------|-----------|-----------------------------|
| Superconductor Techn., Inc. | Rutherford Backscattering | Maggiore | Funds In | 1.0 | 5/88 - 5/89 |
| Public Service Co. of New Mexico | HTS Theory | Parkin | Funds In | 357.1 | 6/88 - 6/90 |
| EPRI | Assessments for Utilities | Newkirk | Funds In | 99.8 | 6/88 - 6/89 |
| AMP, Inc. | RF Characterization of TI-Based HTS Films | Wallace | Funds In | 102.9 | 1/89 - 5/89 |
| EPRI | Heat Pipe Switch | Merrigan | Funds In | 150 | 1/89 - 1/90 |
| Univ. Missouri, Rolla | HTSC Fibers | Maestas | Funds Out | 111 | 1/89 - 1/90 |
| Bechtel | SMES Systems/ Hot-to-Cold Transitions | Maestas | Funds Out | 10 | 2/89 - 2/90 |
| Rocketdyne Corp., Rockwell, Intl. | Synthesis of TI HTS | Peterson | Funds Out | 95.3 | 5/89 - 5/90 |
| EPRI | New Families of HTS | Smith | Funds In | 120 | 2/90 - 2/92 |
| Underground Systems | Transmission Systems | Stewart | Funds In | 48 | 5/91 - 5/92 |
| W.J. Schafer Assoc. | SMES Assessment | Peterson | Funds Out | 89.9 | 5/92 - 5/93 |
| Univ. Calif.-San Diego | Hydrocode Models | Peterson | Funds Out | 63 57 | 12/92 -12/93 6/94 - 5/95 |
| Intermagetics General Corp. | TI-Based HTS Coils | Peterson | Funds Out | 400 | 10/92 - 10/96 |
| MIT | Bitter Magnets | Peterson | Funds In | 50 | 5/93 - 4/96 |
| Midwest Superconductivity, Inc. | IBAD-Coated Flexible Substrates | Peterson | SBI Tech Consulting Agreement | 5 | 3/95 - 3/96 |
| EPRI | Ac Loss Measurements in HTS Cables | Maley | Funds In | 150 | 9/5/95-9/4/96 |
| EPRI | Thick Films on Flexible Substrates | Wu | Funds In | 25 200 | 7/95-9/95 10/95-10/96 |
| Pirelli Cable & Systems | Ac Losses on HTS Cables | Peterson Willis | Funds In | 55 63 | 11/97 – 6/98 1/99 – 9/99 |
| Columbia Univ. | HTS Susceptometer | Peterson | Funds In | 237 | 7/02 - 4/03 |

6c. Superconductivity Pilot Center Agreements - Completed

| Organization | Topic | PI | Funding,\$K DOE | Funding,\$K Partner | Dates |
|--|---|--|--|-----------------------------------|--|
| CPS Superconductor | Metal-Ceramic Interfaces | Mitchell | 102.6 | 80.8 | 9/89 - 9/90 |
| DuPont / Hewlett- Packard | HTS Electronic Components | Peterson | 3777 | 7200 | 10/89 - 10/92 |
| Space Industries, Inc. | Microgravity Processing | Peterson | 205 | 247 | 4/90 - 4/91 |
| Cryopower Associates | Improvement of Bulk HTS Materials | Maley Maley | 45.2 199.4 | 60 485.9 | Ph 1: 2/90 Ph 2: 1/92 1/94 |
| HiTc Superconco | Optimizing Performance of HTS Cavities and Targets | Wu Wu | 136.6 101.9 | 125 100 | Ph 1: 9/89 Phase 2: 12/91 |
| Ceracon, Inc | Bulk HTS Consolidation | Foltyn | 237.5 | 300 | Phase 1: 6/91 |
| Nuclear Metals/ SNL/AT&T | HTS Co- extrusion | Wallace Bingert | 239.2 239.2 | 760.5 285 NM 190 ATT | Ph 1: 8/90- 8/93 Ph. 2: 10/93-10/96 |
| The Boeing Company | Superconducting Electromagnetic Devices | Peterson | 240 | 240 | 4/97 - 4/98 |
| Power Superconduct- ing Devices, Inc | Development of HTS Fault Current Limiter | Peterson | 250 | 250 | 7/96-7/98 |
| American Superconductor Corporation | Bi-2223 Conductors HTS Composite Conductors | Peterson Peterson Willis Willis Willis Holesinger | 170.5 587.1 1500 2300 1800 | 179 350 950 1100 1800 | Ph 1: 6/89- Ph 2: 11/91- Ph 3: 2/94- Ph 4: 3/96- Ph.5: 7/98- 3/01 |